Charles University in Prague
Faculty of Mathematics and Physics

Institute of Physics, Academy of Sciences of the Czech Republic

DOCTORAL THESIS

Martin Ondráček

Morphology of crystal surfaces – theoretical interpretation of the STM

Supervisor:	RNDr. František Máca, CSc.
Advisor:	Ing. Vladimír Cháb, CSc.
Branch:	f5-Physics of surfaces and interfaces

Prague 2008

Acknowledgments

I am much indebted to my supervisor, RNDr. František Máca, CSc., for his helpful and friendly attitude and the infinite patience he was showing towards me during all the time I was working on this thesis. I highly appreciate the extensive assistance that he has been always willing to offer me in all aspects of my work. I am also much grateful to RNDr. Josef Kudrnovský, CSc. for introducing me into the TB-LMTO method and for his help and advice he has given me concerning this method. I thank Ing. Alexander B. Shick, CSc. for his advice on the subject of magnetocrystalline anisotropy. Further, I would like to acknowledge all the support I have received from Ing. Vladimír Cháb, CSc. I would also like to express my gratitude to Prof. Peter M. Oppeneer for his hospitality during my stay in Uppsala in fall 2006. Finally, my special thanks go to my family and in particular to my parents for all the invaluable support and constant encouragement, without which this thesis would have hardly come to completion.

Contents

1 Introduction

There has been an ever increasing interest in the physics of solid surfaces for several last decades. The interest has been stimulated—apart from the many prospective applications of this field of physics—by enlarging the possibilities on hand due to the ongoing development and refinement of suitable experimental tools. The progress in the experimental part of surface physics has been accompanied by the perfection of theoretical description, which has been facilitated by the steadily increasing capacity of computers. A prominent example of surface-sensitive experimental methods are scanning probe techniques, which are capable of resolving details on solid surfaces down to individual atoms; these are namely the scanning tunneling microscope (STM) and the atomic force microscope (AFM). On the one hand, the scanning probe techniques allow the physicists to study the structure of many types of surfaces on the atomic scale. On the other hand, the interpretation of, say, an STM image of a given surface is not always straightforward. A theoretical analysis supplementing the experiment is especially valuable in such cases in which the interpretation of the experimental data turns out to be ambiguous.

While the first applications of the STM at the dawn of this method were mostly to ordered crystal surfaces like, e.g. the Au(110) [1, 2] surface or the 7×7 reconstructed Si(111) [3] surface, the range of the applications extended soon thereafter towards other types of surfaces, including disordered surfaces of binary alloys, adsorbate-covered surfaces etc. The introduction of the spin-polarized STM [4] (and recently the magnetic exchange force microscope [5]) has further enriched the capabilities of the scanning-probe methods, allowing it to probe magnetic properties of surfaces.

The goal of this thesis is to show on the examples of several surface systems how the theoretical analysis and numerical simulations make it possible to understand experimental data obtained by means of the STM and scanning tunneling spectroscopy (STS). More specifically, the aims are to

1. interpret the images and spectra obtained with the STM on the (001) surface of an alloy that consists of 64 atomic % Fe and 36 atomic % Ni (i.e. the alloy known as the Invar), focusing on the lighter and darker spots and the background intensity modulation seen in the images as well as on the main features of the tunneling spectra.

2. analyze the magnetic properties of the tungsten (001) surface covered by an adsorbate of magnetic $3d$ transition metals in order to understand what findings can be expected from the ongoing experimental investigation of such surfaces by means of the spin-polarized STM. The problems to be studied include:

   (a) monoatomic layers of the $3d$ transition metals on the W(001) surface in which two different $3d$ metals are mixed together, thus forming a two-dimensional surface alloy,

   (b) disordered structures formed by sub-monolayer films of the $3d$ transition metals on the W(001) surface, and

(c) the effect of the surface magnetocrystalline anisotropy on the overlayers of the $3d$ transition metals on the W(001) substrate.

The systems that have been chosen to be studied theoretically in this thesis have already been subject to an STM study and, moreover, they are likely to be further investigated by means of this experimental tool in the future, since there are still open questions which can be answered this way. What all these systems have in common is that they are solid state surfaces which contain more than just one chemical element, they exhibit some degree of disorder, and they are in general magnetic.

After summarizing the theoretical concepts and computational tools which are going to be used throughout the thesis in Chapter 2, I will proceed to deal with the $\mathrm{Fe}_{0.64}\mathrm{Ni}_{0.36}(001)$ surface in Chapter 3 and with disordered magnetic films of $3d$ transition metals on the W(001) surface in Chapter 4. The experiment that has motivated the theoretical research of the $\mathrm{Fe}_{0.64}\mathrm{Ni}_{0.36}(001)$ (Invar) alloy surface will be briefly described in Section 3.1. In Section 3.2, I will focus on my results concerning the geometrical structure of $\mathrm{Fe}_{0.64}\mathrm{Ni}_{0.36}(001)$ and its connection with the topography of STM images of this surface. Section 3.3 is then focused on the results concerning the electronic structure of the Invar (001) surface and the relation of the electronic structure to the results of the scanning tunneling spectroscopy (STS). In the next chapter, Section 4.1 will concern the two-dimensional binary alloys of the $3d$ transition metals deposited as a monoatomic layer on the W(001) surface; Section 4.2 will deal with the disordered sub-monolayer films of the $3d$ transition metals on the W(001) substrate; Section 4.3 will contain a discussion of how the relaxation of surface atomic positions influences the magnetic properties of the overlayers on the tungsten substrate; and, in Section 4.4, the results concerning the magnetocrystalline anisotropy of the overlayers will be eventually presented. The main results at which I have arrived will be summarized at the ends of both chapters that deal with the specific systems, in Section 3.4 and Section 4.5, respectively, and then, finally, in the concluding chapter (Chapter 5) at the end of the thesis.

2 Theory

2.1 Scanning tunneling microscope

Scanning tunneling microscope (STM), which was devised by Gerd Binnig, Heinrich Rohrer, and collaborators [6] in early 1980s, provides a possibility to observe atomic-sized features on a wide range of solid surfaces in a direct way—a possibility that was indeed revolutionary at the time when this microscopic technique was invented. The atomic structures that can be imaged by the STM include the patterns of surface reconstructions, monoatomic steps, individual atoms or molecules adsorbed on surfaces, and other surface structures of comparable size (for the early development and first applications of the STM, see[7]). Scanning tunneling microscopy, as a method based on a scanning probe, renders a real-space image of the investigated surface, hence the 'direct observation' mentioned above. The real-space picture given by the STM distinguishes it from other experimental techniques, namely various diffraction methods, which were, of course, used to study atomic structures long before the STM was invented. Although another scanning-probe technique, the atomic force microscope (AFM), has been demonstrated to be capable of atomic resolution too, the STM remains an invaluable tool of surface science with innumerable applications (see, e.g., [8] for some more examples, apart from those cited in [7]).

The probe of the STM is a metallic stylus ended by an atomically sharp tip. A voltage bias is applied between the stylus and the sample during the scanning. The stylus is mounted on a positioning system equipped with piezoelectric elements. The motion of the stylus can be thus controlled by voltage applied to these piezoelectric elements. Before the scanning starts, the stylus has to be placed above the investigated surface in such a way that the gap between the tip of the stylus and the surface is only several ångströms wide . The narrow gap between the two electrodes—the tip and the sample—forms a potential barrier through which electrons can penetrate due to the tunneling effect. As a result of the applied voltage bias, the electron flow through the gap in one direction prevails over the flow in the opposite direction and a nett electric current from one electrode to the other results. The magnitude of this tunneling current is very sensitive to the width of the barrier, i.e. to the distance separating the tip of the probe from the surface of the sample. The decrease of the tunneling current with increasing barrier width is approximately exponential. Therefore, the current is a good measure of the height of the tip's position above the scanned surface. This fact is utilized in the most common mode of operation, called *'constant current mode'*, in which a feedback loop attempts to maintain the tunneling current at a constant preset value by adjusting the vertical position of the tip, i.e. by bringing it closer to the surface or retracting it away from the surface. Because of the exponential dependence of the current on the barrier width, keeping a constant current means that approximately constant distance of the tip from the surface is maintained as the tip moves above the surface during the scanning. The trajectory of the tip above the surface thus follows the profile of the surface itself. The topography of the surface may be apparently reconstructed from the record of the voltage that controls (by means of the piezoelectric elements) the position of the tip. There are, however, some pitfalls in interpreting the obtained image as a surface topography. First, there is this qualifier *'approximately'* in the statement that keeping constant current results in constant distance between the tip and the surface. The tunneling current depends, of course, not only on the width of the barrier but also on its height and shape and on the electronic structure of the surface (and also on that of the tip). The electron density or the height of the potential barrier, which is related to local work function, may vary between different sites on the surface and may thus contribute to the final image. Second, when dealing with a surface on an atomic scale, it is even not obvious what the term 'topography' really means. A more exact description of the tunneling process is therefore needed for proper interpretation of the image produced by the microscope.

2.2 Bardeen integral

The tunneling current flowing between two electrodes separated by a potential barrier can be calculated using a formula derived by Bardeen [9]. Bardeen developed his theory of the tunneling effect about twenty years before the STM was invented. Later, the theory was adapted for the theoretical description of the STM. Here, I will loosely follow the modification of Bardeen's theory that has been suggested by Chen [10, 11]. Although Bardeen originally formulated his theory as a many-particle one (and he even stressed its many-body nature in the title of his paper), I will restate it, like Chen did, in single-particle terms.

Bardeen's expression for the tunneling current may be derived with the help of the first-order time-dependent perturbation theory. However, the treatment of the tunneling effect that is going to be expounded here deviates from the way in which the perturbation theory is usually applied. The ordinary time-dependent perturbation theory starts with one unperturbed system (described by a certain unperturbed Hamiltonian) and one set of unperturbed stationary states, which are the *eigenstates* of the unperturbed Hamiltonian. The perturbation then causes transitions between the states within this one set of states. For the description of the tunneling effect, on the other hand, it is convenient to introduce two different sets of unperturbed states: one set for the initial states and the other for the final states of the transition. An obvious interpretation is that these two sets comprise eigenstates of two respective subsystems, each representing one of the electrodes involved in the process of tunneling.

Let us suppose that the whole system of two interacting electrodes can be described by a (single-particle) Hamiltonian

$$\hat{H} = -\frac{\hbar^2}{2m_e}\Delta + V(\vec{r}), \tag{1}$$

where $\hbar$ is the reduced Planck constant, m_e the mass of the electron, Δ denotes the Laplace operator, and V is an effective electron potential. Similarly, the two unperturbed Hamiltonians, each corresponding to one separate electrode, will have the form

$$\hat{H}_S = -\frac{\hbar^2}{2m_e}\Delta + V_S(\vec{r}), \tag{2a}$$

$$\hat{H}_T = -\frac{\hbar^2}{2m_e}\Delta + V_T(\vec{r}). \tag{2b}$$

The choice of the indices that discriminate between the two subsystems is motivated by the the prospective application of the theory. In the case of the STM, one electrode is a sample (S) and the other one is the tip (T) of the stylus. I will assume in the following that the tunneling happens in the direction from the tip into the sample. Since the roles of the electrodes in the theory are completely interchangeable, tunneling in the opposite direction could be treated in an analogous way. We will now introduce two complete orthogonal sets of states, $\{\psi_m^{(S)}\}$ and $\{\psi_n^{(T)}\}$, defined as the eigenstates of the respective unperturbed Hamiltonian,

$$\hat{H}_S\psi_m^{(S)} = E_m^{(S)}\psi_m^{(S)}, \tag{3a}$$

$$\hat{H}_T\psi_n^{(T)} = E_n^{(T)}\psi_n^{(T)}. \tag{3b}$$

Now, let us divide the whole space into two semi-infinite regions (denoted by S and T) so that they would contain one of the electrodes each. The cutting surface (Σ) separating these two regions should be placed somewhere inside the potential barrier between the electrodes. The unperturbed effective potentials $V_S(\vec{r})$ and $V_T(\vec{r})$ have to follow two conditions with respect to the just introduced semi-infinite regions: First, the unperturbed potential of each electrode should be equal to the potential V (the potential of the whole interacting system) inside the region associated with that particular electrode. That is, $V_S(\vec{r}) = V(\vec{r})$ for all $\vec{r} \in S$ and, analogously, $V_T(\vec{r}) = V(\vec{r})$ for all $\vec{r} \in T$. Second, the unperturbed potential of each electrode should be high enough in the region that contains the other electrode (i.e. $V_S(\vec{r})$ for $\vec{r} \in T$ and $V_T(\vec{r})$ for $\vec{r} \in S$), so that all relevant unperturbed wave functions fall off to zero with increasing distance from the electrode to which they belong. By 'relevant', I mean any wave function corresponding to a state that is—or at least may possibly become—occupied by an electron during the process of tunneling. The latter requirement imposed on the potentials ensures that the unperturbed stationary states are localized inside their respective electrodes.

Consider the temporal evolution of an electron state, described by a wave function $\Psi_n(\vec{r},t)$, that is initially (at $t=0$) equal to $\psi_n^{(T)}$. Using the *ansatz*

$$\Psi_n(\vec{r},t) = \psi_n^{(T)}(\vec{r})e^{-iE_n^{(T)}t/\hbar} + \sum_m c_{mn}(t)\psi_m^{(S)}(\vec{r})e^{-iE_m^{(S)}t/\hbar} \tag{4}$$

for the wave function, we may express the evolution of the state by the time dependence of the coefficients $c_{mn}(t)$. The square of the absolute value of a coefficient $c_{mn}(t)$ is proportional to the probability of transition from the initial state $\psi_n^{(T)}$ to a final state $\psi_m^{(S)}$. From the time-dependent Schrödinger equation,

$$i\hbar\frac{\partial}{\partial t}\Psi_n = \hat{H}\Psi, \tag{5}$$

after substituting the right-hand side of Eq. (4) for Ψ and using Eqs. (1–3), we obtain

$$\begin{aligned} i\hbar\sum_m \frac{\partial c_{mn}}{\partial t}\,\psi_m^{(S)}\,e^{-iE_m^{(S)}t/\hbar} &= (V - V_T)\,\psi_n^{(T)}\,e^{-iE_n^{(T)}t/\hbar} + \\ &+ \sum_m c_{mn}(t)\,(V - V_S)\,\psi_m^{(S)}\,e^{-iE_m^{(S)}t/\hbar}. \end{aligned} \tag{6}$$

For the sake of brevity, the spatial dependence of the potentials and wave functions has not been indicated explicitly in the above equation. In the first order perturbation theory, the coefficients $c_{mn}(t)$ on the right-hand side of Eq. (6) may be replaced by their initial values $c_{mn}(0)$. It follows from the initial condition that $c_{mn}(0) = 0$. Consequently, only the first term on the right-hand side of Eq. (6) remains nonzero. An individual coefficient c_{mn} may be separated on the left-hand side of Eq. (6) by means of multiplying the equation by the complex conjugate to $\psi_m^{(S)} e^{-iE_m^{(S)} t/\hbar}$, integrating over the whole space, and using the orthogonality relation

$$\int d^3r \, (\psi_m^{(S)})^* \, \psi_{m'}^{(S)} = \delta_{mm'} \tag{7}$$

for the unperturbed stationary states. After performing the above described steps, we obtain

$$\frac{\partial c_{mn}}{\partial t} = \frac{1}{i\hbar} \int d^3r \, (\psi_m^{(S)})^* \, (V - V_T) \, \psi_n^{(T)} \, e^{i(E_m^{(S)} - E_n^{(T)})t/\hbar}. \tag{8}$$

Integrating Eq. (8) with respect to the time variable and taking the square of the absolute value of the coefficient c_{mn} yields the transition probability,

$$|c_{mn}(t)|^2 = \left(|M_{mn}| \frac{\sin\left((E_m^{(S)} - E_n^{(T)})t \,/\, 2\hbar \right)}{(E_m^{(S)} - E_n^{(T)}) \,/\, 2} \right)^2 . \tag{9}$$

In the last equation, M_{mn} denotes the matrix element

$$M_{mn} = \int d^3r \, (\psi_m^{(S)})^* \, (V - V_T) \, \psi_n^{(T)}. \tag{10}$$

The current that arises due to an electron tunneling from the state $\psi_m^{(S)}$ to the state $\psi_n^{(T)}$ equals the transition probability per unit time multiplied by the charge of the electron,

$$I_{mn} = \lim_{t\to\infty} \frac{e|c_{mn}(t)|^2}{t} = -\frac{2\pi e}{\hbar} |M_{mn}|^2 \delta(E_m^{(S)} - E_n^{(T)}). \tag{11}$$

Summation over all possible transitions and accounting for the fact that the tunneling only occurs from an occupied state into an empty states finally leads to an expression for the total tunneling current,

$$I = \frac{2\pi e}{\hbar} \sum_{mn} \left[f_S(E_m^{(S)}) - f_T(E_n^{(T)}) \right] |M_{mn}|^2 \delta(E_m^{(S)} - E_n^{(T)} - eU). \tag{12}$$

The distribution functions f_S and f_T give the average number of electrons in a stationary state with given energy in the sample and the tip, respectively. They are typically equal to the Fermi distribution function corresponding to the temperature of the system. For low temperatures, the distribution functions become equal to zero above the Fermi level and to 1 (or 2, so as to account for spin degeneracy in non-magnetic systems while treating two states that differ only by spin as one state) below the Fermi level. The effect of the applied voltage bias U may be described by introducing two separate quasi-Fermi levels, one for each electrode (sample and tip), shifted by eU with respect to each other. Instead of redefining the distribution functions and the energy spectra so that they would include this energy shift, I found it more convenient to put the shift into the argument of the Dirac δ-function that ensures energy conservation during the tunneling process described by Eq. (12).

What remains to be done is transforming the formula for the matrix element M_{mn} into a form that would be more symmetric (with respect to interchanging the electrodes) and more appropriate for a practical calculation than Eq. (10). We start with the observation that the term $(V - V_T)$ can only be non-zero in the region S (which contains the sample) because, for the region T (which contains the tip), the equality $V = V_T$ has been postulated. The integration in Eq. (10) may thus be limited to the region S, where $V = V_S$. Taking this into account, we may rewrite Eq. (10) as

$$M_{mn} = \int_S d^3r \, (\psi_m^{(S)})^* \, (V_S - V_T) \, \psi_n^{(T)}. \tag{13}$$

The next step will consist in expanding the integrand in the following way:

$$\begin{aligned} M_{mn} \;=\; \int_S d^3r \;\; \Big[\;\; & \psi_n^{(T)} \, (-\frac{\hbar^2}{2m_e}\Delta + V_S) \, (\psi_m^{(S)})^* - \\ - \;\; & (\psi_m^{(S)})^* \, (-\frac{\hbar^2}{2m_e}\Delta + V_T) \, \psi_n^{(T)} + \\ + \;\; & (-\frac{\hbar^2}{2m_e}) \left((\psi_m^{(S)})^* \Delta \psi_n^{(T)} - \psi_n^{(T)} \Delta (\psi_m^{(S)})^* \right) \Big]. \end{aligned} \tag{14}$$

Applying Eqs. (3a,b) on the first two terms in the integrand on the right hand side of Eq. (14) yields

$$\begin{aligned} M_{mn} \;=\; \int_S d^3r \;\; \Big[\;\; & (E_m^{(S)} - E_n^{(T)}) \, (\psi_m^{(S)})^* \, \psi_n^{(T)} + \\ + \;\; & (-\frac{\hbar^2}{2m_e}) \left((\psi_m^{(S)})^* \Delta \psi_n^{(T)} - \psi_n^{(T)} \Delta (\psi_m^{(S)})^* \right) \Big]. \end{aligned} \tag{15}$$

Because of the Dirac δ-function on the right-hand side of Eq. (11), only terms with $E_m^{(S)} = E_n^{(T)}$ contribute to the tunneling current. We may therefore omit the first term on the right-hand side of Eq. (15), so eventually only the last of the three terms on the right-hand side of Eq. (14) will remain:

$$M_{mn} = -\frac{\hbar^2}{2m_e} \int_S d^3r \left((\psi_m^{(S)})^* \Delta \psi_n^{(T)} - \psi_n^{(T)} \Delta (\psi_m^{(S)})^* \right). \tag{16}$$

This remaining term may be rewritten, using the divergence and gradient operators, as

$$M_{mn} = -\frac{\hbar^2}{2m_e} \int_S d^3r \; \mathrm{div} \left((\psi_m^{(S)})^* \nabla \psi_n^{(T)} - \psi_n^{(T)} \nabla (\psi_m^{(S)})^* \right). \tag{17}$$

The last form of M_{mn} suggests using the Gauss theorem to transform the integral over the three-dimensional region S into an integral over a closed surface that forms a boundary of the region S. The only part of the boundary surface that contributes to the integration is, however, the boundary Σ between the regions S and T. The rest of the closed surface is situated in infinity, where $\psi^{(T)}(\vec{r})$ is infinitely small. Consequently, the whole expression after the divergence operator in Eq. (17) is infinitely small everywhere on the closed surface around S except for the surface Σ. The final expression for the matrix element then becomes

$$M_{mn} = -\frac{\hbar^2}{2m_e} \int_\Sigma d\vec{S} \cdot \left((\psi_m^{(S)})^* \nabla \psi_n^{(T)} - \psi_n^{(T)} \nabla (\psi_m^{(S)})^* \right) . \tag{18}$$

The differential vector quantity $d\vec{S}$ in the above equation has a magnitude of an element of Σ and the direction of a normal to Σ. More specifically, $d\vec{S}$ is supposed to point from S to T (rather than *vice versa*), but this is not critical to keep in mind because only the absolute value of M_{mn} is needed to calculate the tunneling current. In conclusion, equations (12) and (18) are the principal results of the perturbative approach to the problem of tunneling.

An especially appealing feature of Bardeen's method is that it allows us to divide a complex problem into two more feasible ones. We can separately calculate the electronic structure of the sample and that of the tip. The results are then easily combined by substituting the eigenfunctions of both subsystems into Eq. (18). Such an approach, however, implicitly includes another approximation besides the already discussed use of the perturbation theory. Although the unperturbed wave functions that occur in Eq. (18) belong to *separate* electrodes, the effective potentials V_T and V_S, which determine these wave functions, are still related to the effective potential V of the whole *coupled* system of the sample and the tip. The relationship is established through the requirement that V_S be identical to V in the region S and V_T be identical to V in the region T. If the respective electronic structures of the two subsystems (electrodes) are to be calculated truly separately, such relation to the coupled system has to be broken. The calculated effective potentials of the isolated electrodes will thus differ from the 'correct' potentials V_S and V_T (since the latter should be related to V). The largest difference can be expected inside the potential barrier between the electrodes—near the separation surface Σ—where both electrodes influence the shape of the potential simultaneously. Important factors that modify the shape of the barrier are especially the external voltage bias and the contact potential (i.e. the difference of work functions) between the electrodes. Unfortunately, these factors cannot be taken into account as long as the electrodes are treated separately.

The condition for applicability of the perturbation theory is that the tunneling current should cause just a negligible change of the stationary electronic structure of the electrodes. Such a condition will often be fulfilled for the STM, unless a contact mode is approached. On the other hand, the next approximation, which consists in replacing the potentials V_S and V_T with potentials calculated for truly isolated electrodes, is not automatically justified. The latter approximation implies that the shape of the potential barrier must not be significantly affected by the coupling of the two electrodes. This requirement can be roughly satisfied if the two electrodes (i) are separated by a broad barrier with a region of a nearly flat potential in its center and (ii) their contact potential is approximately compensated by the applied voltage bias.

So far, I have not explicitly considered the spin of the electron. In a non-magnetic system, it has only to be taken into account that any single-particle state characterized by a particular wave function may be occupied by two electrons instead of one. The existence of the electron spin thus only contributes a factor of 2 to the expression for the tunneling current in a non-magnetic case. If the sample or the tip or both are magnetic, there may still exist a quantization axis such that the projection of the spin onto that axis is a good quantum number. If this is the case, the electron states can be divided according to the projection of the spin into two groups (which we may call, e.g., spin-*up* electrons and spin-*down* electrons) and the sum in Eq (12) then simply runs over both possible values of the spin. In the most general case, in which no spin projection is a good quantum number, either because the sample has a magnetic quantization axis different from the tip or because there are some more complex magnetic structures in the sample (like, e.g., spin spirals), the simple wave functions have to be replaced by two-component wave functions to account for the spin. However, even in the last most general case, the generalization of Eqs. (12) and (18) is quite straightforward.

2.3 Tersoff–Hamann model

The above described scheme allows for practical calculation of the tunneling current based on known electronic structures of an isolated sample and an isolated tip of the STM probe. However, the structure of the tip is often unknown or may even vary from experiment to experiment due to the impossibility of manufacturing the STM probes in a completely reproducible way. It is therefore desirable to introduce a further approximation that would allow us to estimate the tunneling current without any reference to the detailed structure of the tip. Such an requirement is met by the approximation suggested by Tersoff and Hamann [12], which replaces the real tip by a simple spherical-symmetric model. It should be noted here that the knowledge of the electronic structure of the tip is, as a general rule, indispensable for a realistic simulation of STM images and spectra (see, e.g., the introductory discussion in [13] or [14]) and the method of Tersoff and Hamann must therefore be regarded merely as a very rough approximation that may only allow for qualitative estimates. On the other hand, some features of the images and spectra acquired by the STM turn out to be more or less independent from what particular tip is used as a probe in the experiment. Such features may be—and often were indeed—successfully interpreted in terms of the Tersoff-Hamann approximation.

The principal assumption that enters into the derivation of the Tersoff-Hamann approximation is the already mentioned spherical model of the tip. This assumption translates into the spherical symmetry of $V_T(\vec{r}-\vec{r}_0)$, where $\vec{r}_0$ in the position of the imaginary center of the tip. A further assumption is that the potential $V_S(\vec{r})$ has a constant value V_0 throughout the region T (that contains the tip) and, conversely, $V_T(\vec{r})$ equals the same constant value V_0 throughout the region S (that includes the sample). It is not difficult to satisfy the condition $V_S(\vec{r}) = V_0$ for $\vec{r} \in T$ because V_S may be arbitrary outside the region S in Bardeen's theory—it only has to be sufficiently high in the region T for the perturbation theory to work. In a practical calculation, V_S will typically approach a constant vacuum level far from the solid sample. The requirement $V_T(\vec{r}) = V_0$ for $\vec{r} \in S$, on the other hand, has to be consistent with the assumed spherical symmetry of V_T. The two requirements for

V_T, i.e. the isotropy of $V_T(\vec{r}-\vec{r}_0)$ and the constancy of $V_T(\vec{r})$ for $\vec{r} \in S$, may only be reconciled if we assume that $V_T(\vec{r}) = V_0$ not only in the region S, but everywhere apart from the interior of the spherical tip itself; i.e., V_T should be constant everywhere outside a certain sphere of radius R that is centered in $\vec{r}_0$. No special assumption has to be made about the radius R, it only must not be too large, so that the whole sphere that represents the tip of the STM probe is contained in the region T and does not intersect the boundary surface Σ.

The solution of the Schrödinger equation (3a) for the wave function of the tip in the region where $V_T(\vec{r}) = V_0$ is

$$\psi_n^{(T)}(\vec{r}) \propto \frac{1}{|\vec{r}-\vec{r}_0|} e^{-k_n|\vec{r}-\vec{r}_0|}, \tag{19}$$

where

$$k_n = \frac{\sqrt{2m_e(V_0-E_n)}}{\hbar}. \tag{20}$$

In the following, I will denote the right hand side of Eq. (19) by $4\pi\chi_m(\vec{r})$, i.e.,

$$\chi_n(\vec{r}) = \frac{1}{4\pi|\vec{r}-\vec{r}_0|} e^{-k_m|\vec{r}-\vec{r}_0|}. \tag{21}$$

While Eq. (19) holds only outside the sphere of radius R around the point $\vec{r}_0$, where V_T equals V_0, the definition of the function $\chi_n(\vec{r})$ as given by Eq. (21) is meant to hold for any $\vec{r}$. As a consequence, $\chi_n(\vec{r})$ will in general deviate from $\psi_T(\vec{r})$ inside the sphere that represents the tip of the STM probe. Nonetheless, the two functions will equal each other (except for normalization) everywhere outside the sphere, especially also at the separation surface Σ. From now on, I will drop the superscript (S) from $\psi_m^{(S)}$, denoting the wave functions of the sample plainly by ψ_m. With the above introduced notation at hand, we may rewrite Eq. (18) in the form

$$M_{mn} \propto \frac{\hbar^2}{2m_e} \int_T d^3r \left(\psi_m{}^* \Delta\chi_n - \chi_n \Delta\psi_m{}^*\right). \tag{22}$$

Eq. (22) has a form rather similar to Eq. (16) and it has been obtained from Eq. (18) by a step essentially inverse to the one that led from Eq. (16) to (18). The different domain of integration—the integration is performed over the region T instead of the region S—is of minor importance since the electrodes are mutually interchangeable in the theory and so are the corresponding regions S and T. A more important difference between Eq. (22) and Eq. (16) is that the integrands are not equal in the whole range of integration because of the possible difference between the functions $\chi_n(\vec{r})$ and $\psi_m^{(T)}$ inside the sphere that represents the tip. The action of the Laplace operator on ψ_m in the region T,

$$\Delta\psi_m(\vec{r}) = \frac{2m_e(V_0-E_m)}{\hbar^2}\psi_m(\vec{r}), \tag{23}$$

follows immediately from the Schrödinger equation. The action of the same operator on χ_n can be found from the explicit expression for χ_n, Eq (21), to be

$$\Delta\chi_n(\vec{r}) = \frac{2m_e(V_0-E_n)}{4\pi\hbar^2}\chi_m(\vec{r}) - \delta(\vec{r}-\vec{r}_0). \tag{24}$$

By substituting Eqs. (23) and (24) into Eq. (22) and taking $E_m = E_n$, we obtain the proportionality

$$M_{mn} \propto \psi_m(\vec{r}_0). \tag{25}$$

The contribution of a particular wave function ψ_m to a tunneling current is, according to Eq. (12), proportional to the square of the absolute value of the matrix element M_{mn}. Furthermore, according to the last equation, the matrix element is proportional to the value of the wave function at $\vec{r}_0$, i.e. at the center of the curvature of the tip. The square of the absolute value of a wave function at a particular point equals the density of the probability that the electron would be found in an infinitesimal neighborhood of that point. The total tunneling current can be obtained by summation over all single-electron states that contribute to the tunneling. For a macroscopically large sample, the discrete set of states passes into a continuum. The sum of probability densities has to be replaced by an integration of the local density of states at $\vec{r}_0$ over the relevant interval of electron energies. For low temperatures, all states below the Fermi level may be considered as being fully occupied and all states above the Fermi level totally empty. Under such conditions, only those electron states in the sample contribute to the tunneling whose energy falls into the interval from E_F to $E_F + eU$ (or *vice versa* for an opposite bias), where E_F is the Fermi level in the sample and U denotes the voltage bias applied on the sample. This considerations finally leads to the following relation between the tunneling current and the local density of states:

$$I \propto \int_{E_F}^{E_F+eU} \rho(\vec{r}_0, E)dE, \tag{26}$$

where $\rho(\vec{r}_0, E)$ is the local density states of electrons in the sample at energy E and at the spatial point $\vec{r}_0$. From that, we obtain for the differential tunneling conductivity the relation

$$\sigma = \frac{dI}{dU} \propto \rho(\vec{r}_0, E_F + eU). \tag{27}$$

The quantity called *'local density of states'*, which has been used in the last two relations, may be defined in terms of a sum of probability densities at given energy as the number of single-particle states approaches infinity. Specifically, we may write[1]

$$\rho(\vec{r}_0, E) = \lim_{N\to\infty} \sum_{m=0}^{N} |\psi_m(\vec{r}_0)|^2 \delta(E_m - E). \tag{28}$$

During the discussion leading to Eqs. (26) and (27), I have tacitly assumed that the proportionality constant of Eq. (25) is independent from the energy of the tunneling electrons, so that I would not have to consider different weighting coefficients for contributions from electrons at different energies. Such an assumption is, however, not always justified. The constant of proportionality is given by an unknown normalizing prefactor of the wave function of the tip, which may in turn

---

[1] The limit that appears in Eq. (28) has to be interpreted in terms of distributions (generalized functions), not in the sense of point convergence of ordinary functions.

depend on the energy $E_n^{(T)}$. Note that Eq. (19) defines the wave function $\psi_n^{(T)}$ only up to this unknown prefactor. The uncertainty about the precise value of the proportionality constant hinders any quantitative evaluation of the tunneling current using the Tersoff-Hamann approximation in the form introduced here. Nonetheless, there may still occur such conditions that the normalizing prefactor in front of $\psi_n^{(T)}$ varies only mildly with $E_n^{(T)}$ and the stationary states of the tip are distributed with an approximately uniform density over the relevant interval of energies. Then the relations given by Eq. (26) for the tunneling current and Eq. (27) for the tunneling conductivity may remain valid. For example, if we want to describe an experiment that was carried out under low voltage bias, only a narrow range of energies has to be considered and the variation of M_{mn} with energy may be neglected. An STM image taken in the constant current mode at low bias can be interpreted as a map of the local density of states of electrons above the sample surface. In a spectroscopic measurement, a rather wide range of voltages would be explored, thus casting the applicability of the discussed relations into doubt. We are, nevertheless, usually interested only in some prominent features like peaks in the differential tunneling conductivity when performing spectroscopic measurements. Provided that both the density of states and the form of wave functions of the electrons in the tip depend smoothly enough on energy, so that the tip does not introduce any such pronounced features into the spectra, a peak in tunneling conductance can be ascribed to a peak in the local density of states of the sample, just as indicated by Eq. (27). To sum up, the Tersoff-Hamann approximation does not permit a quantitative evaluation of the tunneling current, but it may still be successful in interpreting the relative changes of the current in terms of a varying local density of states.

2.4 Density functional theory

The Hamiltonian of any system consisting of atoms can be written in the form

$$\hat{H} = \hat{T}_e + \hat{T}_N + \hat{V}_{ee} + \hat{V}_{eN} + \hat{V}_{NN}, \tag{29}$$

where the operators on the right-hand side represent, respectively, the kinetic energy of electrons,

$$\hat{T}_e = -\frac{\hbar^2}{2m_e} \times \sum_{i=1}^{N_e} \Delta_{\vec{r}_i}, \tag{30}$$

the kinetic energy of atomic nuclei,

$$\hat{T}_N = -\frac{\hbar^2}{2} \times \sum_{i=1}^{N_A} \frac{1}{M_i} \Delta_{\vec{R}_i}, \tag{31}$$

the potential energy of the electron–electron interaction,

$$\hat{V}_{ee} = \frac{e^2}{4\pi\epsilon_0} \times \frac{1}{2} \sum_{i=1}^{N_e} \sum_{j=1}^{N_e} \frac{1}{|\vec{r}_i - \vec{r}_j|}, \tag{32}$$

the potential energy of electrons in the field of nuclei

$$\hat{V}_{eN} = -\frac{e^2}{4\pi\epsilon_0} \times \sum_{i=1}^{N_e} \sum_{j=1}^{N_A} \frac{Z_j}{|\vec{r}_i - \vec{R}_j|}, \tag{33}$$

and the potential energy of the nucleus–nucleus interaction

$$\hat{V}_{NN} = \frac{e^2}{4\pi\epsilon_0} \times \frac{1}{2} \sum_{i=1}^{N_A} \sum_{j=1}^{N_A} \frac{Z_i Z_j}{|\vec{R}_i - \vec{R}_j|}. \tag{34}$$

The symbols $\Delta_{\vec{r}_i}$ and $\Delta_{\vec{R}_i}$ denote, respectively, Laplace operators that perform differentiation with respect to the position $\vec{r}_i$ of the i-th electron in the first case and with respect to the position $\vec{R}_i$ of the nucleus of the i-th atom in the other case; N_e and N_A are the respective numbers of electrons and atoms in the system; m_e stands for the mass of electron, M_i for the mass of the nucleus of the i-th atom; e denotes the elementary charge (which, except for the sign, equals the charge of the electron); ϵ_0 is the vacuum permittivity; and Z_i denotes the atomic number of the respective atom (i.e., it gives the charge of the nucleus as a number of elementary charges). The summations in Eq. (32) and Eq. (34) skip the instances in which $i = j$. All the above expressions hold for a non-relativistic case.

The masses of atomic nuclei are several orders of magnitude greater than the mass of electron. This strong inequality implies that we can expect the nuclei to be much more localized than the electrons, at least in the ground state and in low-lying excited states. Such conditions justify the use of the Born-Oppenheimer approximation. This approximation consists in treating the nuclei as being localized in fixed geometrical points while only the electrons are handled as quantum-mechanical objects, i.e., only the system of electrons is represented by a (many-particle) wave function. As a second step in the approximation, an effective potential $V_N(\vec{R}_1, \ldots, \vec{R}_{N_A})$ felt by the nuclei may be introduced so that it would incorporate—apart from $\hat{V}_{NN}$ representing the direct coulombic interaction among the nuclei—also another contribution that describes the effect of electrons on the nuclei. The latter contribution to the effective potential V_N would be equal to the ground-state energy of the system of electrons for the given positions $\{\vec{R}_i\}$ of the nuclei. I am not going to deal with the dynamics of atomic nuclei anywhere in this thesis; therefore I will always restrict myself to calculations within the first step of the Born-Oppenheimer approximation. In other words, I will always assume the atomic nuclei to be just fixed charged points. Their positions will be either taken from experimental data or calculated by applying the condition that the ground-state positions should yield minimal total energy for the combined system of all electrons and nuclei.

After excluding the dynamics of nuclei from the description, the Hamiltonian for which the Schrödinger equation has to be solved reduces to

$$\hat{H}_{el} = \hat{T}_e + \hat{V}_{ee} + \sum_{i=1}^{N_e} v(\vec{r}_i). \tag{35}$$

The last term on the right-hand side of Eq. (35) comes from the electron–nucleus interaction term $\hat{V}_{NN}$ in Eq. (29). The single-particle potential v that constitutes this term will be referred to as an *'external'* potential. The name is meant to indicate that the potential is external to the system of electrons. If we were to consider the whole system including both the electrons and the nuclei, the forces exerted by the nuclei on the electrons and the corresponding potential v would have to be, of course, described as internal. Given the origin of the potential v, it can be obviously evaluated using the formula

$$v(\vec{r}) = -\frac{e^2}{4\pi\epsilon_0}\sum_{i=1}^{N_A}\frac{Z_i}{|\vec{r}-\vec{R}_i|}. \tag{36}$$

The nuclear positions $\vec{R}_i$ now assume a role of external parameters rather than dynamical variables. We may additionally consider a truly external field acting on the electrons, like e.g. an electrostatic field induced by external electrodes. A corresponding additional term would have to be introduced onto the right-hand side of Eq. (36) then. In any case, the origin and the explicit form of the external potential v is not going to matter in the following considerations.

The above Hamiltonian of the electron system, Eq. (35), although simplified, does not yet allow for a direct solution of the corresponding Schrödinger equation. An approximate solution has to be sought therefore. A very successful approximation can be based on the *density functional theory* (DFT). The computational schemes based on the DFT are nowadays routinely applied to many-electron systems ranging from atoms and molecules to crystals. The DFT itself provides an exact description of the many-electron ground state in principle, but its exact form cannot be directly utilized for any practical calculation scheme. The theory has, however, proven useful in motivating reasonable approximations, namely the local density approximation (LDA) and its various generalizations. The basic idea behind the density functional theory is to avoid the (generally very complicated) many-particle wave function $\Psi(\vec{r}_1, \vec{r}_2, \ldots, \vec{r}_N)$ and to express instead all ground-state properties of the many-electron system in terms of one-particle electron density $n(\vec{r})$. The one-particle density is defined as

$$n(\vec{r}) = N\int d^3r_2 \ldots \int d^3r_N |\Psi(\vec{r}, \vec{r}_2, \ldots, \vec{r}_N)|^2, \tag{37}$$

where N denotes the number of electrons (formerly denoted by N_e).

DFT is founded on two theorems, originally formulated and proven by Hohenberg and Kohn [15] in 1964. The first Hohenberg-Kohn theorem states, in essence, that the the external potential $v(\vec{r})$ is a *unique* functional of the ground-state electron density $n(\vec{r})$. The precise meaning of this statement, however, needs to be clarified in some more detail. The first two terms on the right-hand side of Eq. (35)—i.e. the kinetic term and the term that represents the electron–electron interaction—remain always the same. These terms are fully determined by the fact that the interacting particles are electrons and by the number N of the electrons. Different systems of the same number N of interacting electrons can differ only in the external potential $v(\vec{r})$. Once the external potential is also known, all properties of the system described by the Hamiltonian, Eq. (35), are determined in principle, including all properties of the ground state of the system. In this sense, the ground-state wave function may be considered a functional of the external potential, although the functional is not unique because the ground state may be possibly degenerate. Since the electron density is, according to Eq. (37), a (unique) functional of the corresponding wave function, the ground-state density $n(\vec{r})$ is eventually a functional of the external potential too. Likewise, all other characteristics of the ground state are uniquely determined by the ground-state wave function as well, so they may be also regarded as functionals of the external potential. Let us introduce the notation $n[v]$ for the ground-state electron density n that is associated with an external potential v in the above explained way. We may now ask whether the functional $n[v]$ can be inverted. It is not guaranteed for an arbitrary density $n(\vec{r})$ that there exist an external potential which would lead just to that ground-state density $n(\vec{r})$. The densities which may be associated with some external potential are called v-representable. The v-representable densities thus form the domain of the functional inverse to the $n[v]$ functional. One particular v-representable density $n(\vec{r})$ can be clearly obtained by various potentials which differ from each other only by a position-independent additive constant. We will therefore consider two external potentials v and v' to be equivalent for the purpose of the DFT, if

$$v - v' = const. \tag{38}$$

What the first Hohenberg-Kohn theorem says is that if two external potentials $v(\vec{r})$ and $v'(\vec{r})$ lead to one and the same ground-state electron density $n(\vec{r})$, then the potentials are necessarily equivalent in the sense of Eq. (38). The proof of the theorem may be found not only in the original paper of Hohenberg and Kohn [15] but also in almost any textbook dealing with the DFT (e.g. [16]).

We have seen that just like the ground-state density n may be regarded a functional of the external potential v, so may be v, conversely, regarded as a functional of n (provided n is v-representable) and that the latter functional is even unique. It has been already mentioned that the ground-state wave function is a (generally non-unique) functional of the external potential. From the chain of relations

$$n \to v \to \Psi \tag{39}$$

follows that we can also handle the ground-state wave function as a functional of n, though not unique. Through the ground-state wave function Ψ, all physical properties of the ground state are functionals of the ground-state density as well, which is exactly the central idea of the DFT.

Let us consider the following functional $F[n]$ of the density n:

$$F[n] = \langle \Psi[n] | \hat{T}_e + \hat{V}_{ee} | \Psi[n] \rangle, \tag{40}$$

where $\Psi[n]$ denotes the ground-state wave function corresponding to the density n. The functional $F[n]$ is obviously defined for v-representable densities only. In contrast to other functionals depending on n through the possibly degenerate ground-state wave function Ψ, the above introduced functional $F[n]$ is even unique. To show that the ambiguity of $\Psi[n]$ does not affect the uniqueness of $F[n]$, let us consider another functional $E[n]$,

$$E[n] = F[n] + \int d^3r \; (v[n](\vec{r})) \; n(\vec{r}). \tag{41}$$

The functional $E[n]$ has clearly the meaning of the ground-state energy pertaining to the system of electrons with the ground-state density n. Even if the ground state were degenerate and $\Psi[n]$ were thus ambiguous, there would always be *one* ground-state energy for a given system since the ground-state energy must be only one *by definition.* Of course, the functional $E[n]$ supposed to represent the ground-state energy *would* be ambiguous unless we fix the arbitrary additive constant in the potential $v[n]$. Suppose that we have determined the potential uniquely by means of some additional condition (like that the mean value of the potential over the whole space should be zero, or that the potential should be zero at some particular point, etc.) so as to remove this ambiguity. As soon as we choose $v[n]$ uniquely, the functional $E[n]$ becomes unique as well, the ambiguity of $\Psi[n]$ notwithstanding. We may now express $F[n]$ in terms of $E[n]$, using Eq. (41), as

$$F[n] = E[n] - \int d^3r \; (v[n](\vec{r})) \; n(\vec{r}). \tag{42}$$

We can see from the above discussion that Eq. (42) determines $F[n]$ without any ambiguity.

We now introduce the following functional of both n and v with the help of the functional $F[n]$:

$$E[v, n] = F[n] + \int d^3r \, v(\vec{r}) \, n(\vec{r}). \tag{43}$$

The functional $E[v, n]$ will be dubbed *'energy functional'*. The second theorem of Hohenberg and Kohn says that—the external potential $v(\vec{r})$ and the number of electrons N being given—the energy functional $E[v, n]$ assumes its minimal value for the density $n_0(\vec{r})$ that corresponds to the ground-state of the system of N electrons in the external potential v. This minimal value equals the ground-state energy of the system. The fixed number of electrons imposes a constraint

$$N = \int d^3r \, n(\vec{r}) \tag{44}$$

on possible variations of the one-particle density n.

Note that while it may be tempting to think about the functionals $E[v, n]$ as defined by Eq. (43) and $E[n]$ as defined by Eq. (41)—both of which are related to the energy of the system in some way—as if they were identical, they are definitely not. Only if $v_0 = v[n]$, the equality $E[v_0, n] = E[n]$ holds. In any case, however, we may rewrite the definition of $E[v, n]$ as

$$E[v_0, n] = \langle \Psi[n] | \hat{H}_{el}[v_0] | \Psi[n] \rangle, \tag{45}$$

where $\hat{H}_{el}[v_0]$ is the Hamiltonian we obtain from Eq. (35) by substituting the external potential v_0 for v.

The two Hohenberg-Kohn theorems allows us to restate the quest for a ground-state electron density of a many-electron system as a variational problem. The ground-state density is the one that minimizes the above defined energy functional and the minimal value of the functional is the energy of the ground state. However, the original formulation by Hohenberg and Kohn imposes an inconvenient restriction on the electron density $n(\vec{r})$ that enters into $E[v,n]$ as a variational parameter, namely that n must be v-representable. The requirement of v-representability may be lifted if one uses an alternative approach to the DFT, suggested by Levy [17]. Levy proposed another functional of the electron density (which is now usually called the Levy-Lieb functional),

$$Q[n] = \min_{\Psi \to n} \langle \Psi | \hat{T}_e + \hat{V}_{ee} | \Psi \rangle. \tag{46}$$

The minimum on the right-hand side of Eq. (46) is searched under the constraint that the wave function Ψ is compatible with the electron density n in the sense of Eq (37) and that the wave function must be completely antisymmetric. Levy has shown that $Q[n]$ is closely related to the functional $F[n]$ of Hohenberg and Kohn. Specifically, $F[n] = Q[n]$ for any v-representable density n. it is easy to show that if one replaces $F[n]$ by $Q[n]$ in the definition of the functional $E[v,n]$, Eq. (43), the second theorem of Hohenberg and Kohn will still hold for such an altered functional $E[v,n]$. The replacement will, however, extend the domain of the functional to all densities n that may originate from some N-particle wave function.

In conclusion, there exist a certain functional of the one-particle electron density $n(\vec{r})$ that assumes its minimal value equal to the ground state energy for the correct ground-state density $n_0(\vec{r})$. The difficulty with the DFT is that the explicit form of this energy functional is not known. Note that in the above presented constructions of the energy functional $E[v,n]$, either that of Levy or that of Hohenberg and Kohn, the ground-state many-particle wave function was used in a hidden way: recall Eq. (39). Unfortunately, the many-particle wave function is just the quantity we seek to avoid in the calculations. The definition of the functional $E[v,n]$ that was useful to demonstrate its existence and basic properties therefore does not offer much help when a real calculation of the ground-state properties has to be performed. A different practical approach to evaluate the energy functional and find its minimum is needed. The predominantly used method to solve this problem is based on Kohn-Sham equations and the local density approximation.

2.5 Kohn-Sham equations

The fact that the energy functional $E[v,n]$ assumes its minimal value at the ground-state electron density $n(\vec{r}) = n_0(\vec{r})$ leads to the requirement that its variation with respect to the electron density be zero,

$$\left(\frac{\delta E[v,n]}{\delta n} \right) \delta n(\vec{r}) = 0, \tag{47}$$

provided that $n = n_0$ and that the variation δn is constrained by the condition

$$\int d^3 r \, n(\vec{r}) = N, \tag{48}$$

which fixes the total number of electrons. Alternatively, the constraint can be incorporated in the variational condition Eq. (47) by means of a Lagrange multiplier μ (which is independent from $\vec{r}$ and has the physical meaning of the chemical potential). This reformulation renders

$$\left.\frac{\delta E[v, n(\vec{r})]}{\delta n(\vec{r})}\right|_{n=n_0} = \mu. \tag{49}$$

Kohn and Sham [18] suggested splitting the energy functional up into the following terms:

$$E[v, n] = T_0[n] + V_H[n] + V_{XC}[n] + \int d^3r\, v(\vec{r})\, n(\vec{r}), \tag{50}$$

where the functional $T_0[n]$ stands for the kinetic energy of *non-interacting* electrons whose density equals $n(\vec{r})$, $V_H[n]$ is the Hartree functional that represents electrostatic energy of the electron gas without correlation or exchange effects,

$$V_H[n] = \frac{e^2}{8\pi\epsilon_0} \int d^3r \int d^3r' \frac{n(\vec{r})\, n(\vec{r}')}{|\vec{r} - \vec{r}'|}, \tag{51}$$

and $V_{XC}[n]$ is a functional that accounts for exchange and correlation effects, i.e. for the effects that are not included in the other parts of the split energy functional.

After substituting the expansion Eq. (50) into Eq. (49), the variational condition passes into

$$\frac{\delta T_0[n]}{\delta n} + v_{\text{eff}}(\vec{r}) = \mu, \tag{52}$$

where the effective potential $v_{\text{eff}}(\vec{r})$ is defined as

$$v_{\text{eff}} = v + v_H[n] + v_{XC}[n], \tag{53}$$

the n-dependent contributions to the effective potential being given by

$$v_H[n] = \frac{\delta V_H[n]}{\delta n} \tag{54a}$$

or

$$v_H[n](\vec{r}) = \frac{e^2}{4\pi\epsilon_0} \int d^3r' \frac{n(\vec{r}')}{|\vec{r} - \vec{r}'|}, \tag{54b}$$

and

$$v_{XC}[n] = \frac{\delta V_{XC}[n]}{\delta n}. \tag{55}$$

We would have obtained exactly the same equation as Eq. (52) if we were interested in the ground state density of a gas of non-interacting electrons in an external potential equal to v_{eff}. By non-interacting electrons, we shall understand hypothetical particles which possess the same mass as electrons and obey the Pauli exclusion principle like electrons, but do not exert any electromagnetic or other force on each other, in contrast to the electrons. Of course, in the case of the non-interacting electrons, the functional $T_0[n]$ simply represents the total inner kinetic energy of the electron gas with density $n(\vec{r})$.

The problem of the non-interacting particles in an external potential can be solved easily. The corresponding many-particle wave function will assume the form of a Slater determinant consisting of N single-particle wave functions (often referred to as 'orbitals'). The effective potential, as defined by Eq. (53), is independent from the electron spin. We may therefore separate the single-particle wave function into a spin and a spatial part and we only need to deal with the spatial part for the moment. The spatial parts of the orbitals, $\varphi_i(\vec{r})$, can be found as solutions of the Schrödinger equation into with the effective potential v_{eff} enters, i.e.,

$$\left(-\frac{\hbar^2}{2m_e}\Delta + v_{\text{eff}}(\vec{r})\right)\varphi_i(\vec{r}) = E_i\varphi_i(\vec{r}). \tag{56}$$

The Schrödinger equation has infinitely many solutions. Since we are interested in the ground-state solution of the many-particle problem, we will take those solutions of the single-particle Schrödinger equation which are associated with the lowest possible energies. Let us suppose that the solutions φ_i are ordered according to their corresponding energy E_i, starting from the lowest energy for $i = 1$. Of course, we cannot take N-times one and the same solution $\varphi_1(\vec{r})$ that corresponds to the lowest single-particle energy E_1 and compose the Slater determinant of this single-particle orbital alone. The Pauli exclusion principle has to be observed, otherwise the Slater determinant would become zero. Consequently, we may take any particular form of the spatial part of a single-particle orbital only twice at most (due to two possible spin states). So we have to take the first $N/2$ different solutions $\varphi_i(\vec{r})$, $i = 1, \ldots, N/2$, associated with the $N/2$ lowest energies[2]. Let us assume that the single-particle wave functions are normalized to unity:

$$\int d^3r\, |\varphi_i(\vec{r})| = 1 \quad \forall i = 1, \ldots, \infty. \tag{57}$$

The sum of the squares of their absolute values (times the spin degeneracy) then yields the ground-state electron density n_0,

$$n_0(\vec{r}) = 2\sum_{i=1}^{N/2} |\varphi_i(\vec{r})|^2 . \tag{58}$$

Recall, however, that the variational condition for the ground states of both systems, that of interacting and that of non-interacting electrons, can be written in the same form, namely Eq. (52). The ground state density $n_0(\vec{r})$ which is the solution to the auxiliary problem of non-interacting electrons therefore must be the right solution to the original problem of interacting electrons too. The ground-state electron density of the system of interacting electrons can be thus found through Eq. (58). The single-particle wave functions $\varphi_i(\vec{r})$ used to construct the density are referred to as the *Kohn-Sham orbitals* and the Schrödinger-like equation, Eq. (56), which determines the Kohn-Sham orbitals, as the *Kohn-Sham equation*. The only—but substantial—difference between the Kohn-Sham equation for the interacting system

---

[2] Even number of electrons is supposed here. Since we will be interested in systems where $N \to \infty$, the distinction between odd an even N is not going to be an important matter.

and the single-particle Schrödinger equation for the corresponding non-interacting system is an indispensable dependence of the effective potential on electron density in the interacting case. To emphasize the importance of this fact, let me restate the Kohn-Sham equation once again, now with the effective potential being decomposed according to Eq. (53) and with any dependence on the electron density n explicitly noted:

$$\left(-\frac{\hbar^2}{2m_e}\Delta + \frac{e^2}{4\pi\epsilon_0}\int d^3r' \frac{n(\vec{r}')}{|\vec{r}-\vec{r}'|} + v_{XC}[n](\vec{r}) + v(\vec{r})\right)\varphi_i(\vec{r}) = E_i\varphi_i(\vec{r}). \tag{59}$$

We can easily obtain the ground state electron density $n_0(\vec{r})$ if we know the Kohn-Sham orbitals $\varphi_i(\vec{r})$. In order to find the Kohn-Sham orbitals, we have to solve the Kohn-Sham equation, Eq. (59). We should, however, substitute the correct ground-state density n_0 for n in the Kohn-Sham equation. We thus end up with a problem of finding a self-consistent electron density $n(\vec{r}) = n_0(\vec{r})$ that would conform to Eqs. (58) and (59) simultaneously. Such a problem of self-consistency has to be solved iteratively. One has to begin with some trial electron density, solve the Kohn-Sham equation, calculate a new electron density from the Kohn-Sham orbitals, and repeat the last two steps until the electron density does not change substantially any more. In a practical calculation, it is usually necessary to take some combination of the new and the old electron density to the next iteration instead of keeping purely the new density itself, otherwise the resulting density will not converge. However, a detailed description of this procedure, called 'mixing', is beyond the scope of this introductory chapters.

The Kohn-Sham orbitals $\{\varphi_i\}$ and the associated single-particle energies $\{E_i\}$ describe the auxiliary system of non-interacting electrons. Unfortunately, these quantities cannot be easily linked to any of those properties of the interacting system that would allow for a straightforward physical interpretation, like, for example, one-electron Green's functions or one-electron excitation energies. Nevertheless, for the lack of any better one-particle characteristics, I shall still use φ_i and E_i taken from a DFT calculation to interpret observations made by the STM. I shall therefore assume that the above named quantities can be substituted for those single-electron wave functions and single-electron energies that appear, e.g., in Eqs. (12) and (18). As there is no rigorous justification for such a step, it must be considered just another one in the series of approximations.

2.6 Local density approximation

Until now, we have carefully avoided writing down the explicit form of the exchange-correlation energy functional $V_{XC}[n]$ or the corresponding exchange-correlation potential $v_{XC}[n](\vec{r})$. The reason for this is simply that the exact form of the exchange-correlation part of the energy functional is unknown. The difficulty in finding the exchange-correlation functional is by no means surprising indeed. Solving the many-body problem has been avoided by introducing the energy functional $E[v_0, n]$, which depends on the electron density $n(\vec{r})$ only, rather than on the whole many-particle wave function. As a consequence, the energy functional has to incorporate all the difficulties of the original many-body problem. Subsequently, several parts which were comparatively easy to handle have been isolated from the functional $E[v_0, n]$, namely the kinetic energy of non-interacting particles T_0, the Hartree term V_H, and the potential energy in external fields. The rest is the exchange-correlation term. All the complicated phenomena of the many-electron system have been thus finally pushed into the exchange-correlation functional V_{XC}.

If there is no hope of finding an explicit formula for V_{XC}, one might ask what good it was to elaborate the above theory at all. However, while the exchange-correlation potential is not known exactly, reasonable approximations can be made for it. Since V_{XC} constitutes, as a rule, just a lesser contribution to the total energy functional as compared to the other terms that appear on the right-hand side of Eq. (50), it may be considered a justifiable step to replace it with an approximate formula. Most of the routinely used DFT-based algorithms rely on the (in general not fulfilled) assumption that the value of the exchange-correlation potential v_{XC} at a certain point $\vec{r}$ depends exclusively on the properties of the electron density at this very point $\vec{r}$. Specifically, the *local density approximation* (LDA) is based on the assumption that $v_{XC}(\vec{r})$ depends on the value $n(\vec{r})$ at $\vec{r}$ only.

Within the LDA, the functional $V_{XC}[n]$ representing the exchange-correlation energy may be expressed using some function $\epsilon_{LDA}(n)$ of the density in the following way:

$$V_{XC}^{(LDA)}[n] = \int d^3r \, \epsilon_{LDA}\left(n(\vec{r})\right) \, n(\vec{r}). \tag{60}$$

Note that ϵ_{LDA} is a function of a numeric value $n(\vec{r})$—the density at a certain point $\vec{r}$—rather than being a functional of the whole spatial distribution of the electron density. The exchange-correlation potential then becomes

$$v_{XC}(\vec{r}) = \epsilon_{\text{LDA}}\left(n(\vec{r})\right) + n(\vec{r}) \left. \frac{d\epsilon_{LDA}(n)}{dn} \right|_{n=n(\vec{r})} . \tag{61}$$

A physically substantiated choice for the function $\epsilon_{LDA}(n_0)$ is the value of the exchange-correlation energy of homogeneous electron gas with electron density $n(\vec{r}) = n_0$. With this choice, the LDA becomes exact in the limit of a slowly varying density $n(\vec{r})$, but it often yields reasonably good results (total energy, equilibrium interatomic distances etc.) even for realistic atomic systems, where the electron density changes in space appreciably. The exchange-correlation energy of the homogeneous electron gas can be found using Monte-Carlo calculations [19] and several parameterizations have been suggested for it (either based on theoretical considerations or on the Monte-Carlo results or both). The next natural step beyond the LDA consists in introducing also the gradient of the electron density into the description of $V_{XC}[n]$, so that not only the local value of $n(\vec{r})$, but also its changes in the vicinity of $\vec{r}$ may be taken into account. This leads to the *generalized gradient approximation* (GGA), in which

$$V_{XC}^{(GGA)}[n] = \int d^3r \, \epsilon_{GGA}\left(n(\vec{r}), \nabla n(\vec{r})\right) \, n(\vec{r}). \tag{62}$$

2.7 Spin-polarized systems

Several spin-polarized systems (ferromagnets, antiferromagnets, etc.) will be treated in this thesis. All the above considerations regarding the DFT and the derivation of the Kohn-Sham equations hold, strictly speaking, for the spin polarized systems as well. However, the LDA in the above form, in which it does not explicitly include the spin-polarization, would be a very poor approximation for such systems. Also the resulting Kohn-Sham orbitals and their eigenenergies, even if they were obtained from an exact (but not spin-polarized) DFT rather than from LDA, would be useless for an interpretation of STM experiments performed on magnetic systems. The description of the spin-polarized systems improves when the spin is explicitly introduced into the Kohn-Sham scheme from the beginning. We shall decompose the total electron density into two parts,

$$n(\vec{r}) = n^{\uparrow}(\vec{r}) + n^{\downarrow}(\vec{r}), \tag{63}$$

corresponding to opposite spin directions. These components are conventionally referred to as the majority spin and the minority spin density, respectively (or the spin-up and spin-down densities). The majority density would be, naturally, the one that gives a greater number of electrons when integrated over the whole space. The functional $T_0[n]$ in Eq. (50), representing the inner kinetic energy of the non-interacting electron gas with density n, will be replaced by the kinetic energy of a spin-polarized non-interacting electron gas, $T_0[n^{\uparrow}, n^{\downarrow}]$. Also the exchange-correlation energy V_{XC} will be treated as a functional of both $n^{\uparrow}$ and $n^{\downarrow}$. The appropriate generalization of the LDA to spin-polarized system is called the 'local spin density approximation' (LSDA). The expression for the exchange-correlation functional within the LSDA obviously reads

$$V_{XC}^{(LSDA)}[n^{\uparrow}, n^{\downarrow}] = \int d^3r \, \epsilon_{LSDA}\left(n^{\uparrow}(\vec{r}), n^{\downarrow}(\vec{r})\right) \left(n^{\uparrow}(\vec{r}) + n^{\downarrow}(\vec{r})\right), \tag{64}$$

and similar spin-polarized extensions exist for the GGA. The corresponding exchange-correlation potentials may now be expressed as

$$v_{XC}[n^{\uparrow}] = \frac{\delta V_{XC}[n^{\uparrow}, n^{\downarrow}]}{\delta n^{\uparrow}}, \tag{65a}$$

$$v_{XC}[n^{\downarrow}] = \frac{\delta V_{XC}[n^{\uparrow}, n^{\downarrow}]}{\delta n^{\downarrow}}. \tag{65b}$$

We then write down two sets of Kohn-Sham equations, one set for each spin component:

$$\left(-\frac{\hbar^2}{2m_e}\Delta + v_{\text{eff}}^{\uparrow}(\vec{r})\right) \varphi_i^{\uparrow}(\vec{r}) = E_i^{\uparrow} \varphi_i^{\uparrow}(\vec{r}), \tag{66a}$$

$$\left(-\frac{\hbar^2}{2m_e}\Delta + v_{\text{eff}}^{\downarrow}(\vec{r})\right) \varphi_i^{\downarrow}(\vec{r}) = E_i^{\downarrow} \varphi_i^{\downarrow}(\vec{r}). \tag{66b}$$

The spin-resolved densities are obtained as sums over the squares of absolute values of the spin-resolved Kohn-Sham orbitals $\varphi_i^{\uparrow}$ and $\varphi_i^{\downarrow}$,

$$n^{\uparrow}(\vec{r}) = \sum_{i=1}^{N^{\uparrow}} \left|\varphi_i^{\uparrow}(\vec{r})\right|^2, \tag{67a}$$

$$n^{\downarrow}(\vec{r}) = \sum_{i=1}^{N^{\downarrow}} \left|\varphi_i^{\downarrow}(\vec{r})\right|^2 . \tag{67b}$$

The partial numbers of electrons, $N^{\uparrow}$ and $N^{\downarrow}$, that determine the upper bounds of the sums in Eqs. (67) are chosen in such a way that $N = N^{\uparrow} + N^{\downarrow}$ and there exists *one* threshold energy E_F, common to both the spin-up and the spin-down subsystem, such that the summation is performed over all indices i for which the respective eigenenergy $E_i^{\uparrow}$ or $E_i^{\downarrow}$ is lesser than or equal to E_F and over no indices for which the eigenenergy would be greater than E_F. Obviously, the energy E_F can be regarded as the zero-temperature Fermi level (as long as the single-electron picture may be considered a reasonable representation of the system, otherwise it does not make much sense to use the term 'Fermi level' at all).

2.8 Linearized augmented plane wave method

If we were to handle the wave functions $\varphi_i(\vec{r})$, obtained by solving the Kohn-Sham equations, with unlimited precision, we would have to be able to store and process an infinite amount of information: The value of each wave function would have to be specified at every spatial point. In reality, the wave functions will be typically expressed as linear combinations of some basis functions $\{\chi_i\}$,

$$\varphi_i(\vec{r}) = \sum_j c_{ij}\chi_j(\vec{r}), \tag{68}$$

where c_i are complex coefficients, instead of specifying the value of $\varphi(\vec{r})$ for various positions $\vec{r}$ directly. Nonetheless, the situation remains the same: An infinite set of basis function would be needed to represent an arbitrary wave function. Obviously, any practical calculation has to be limited to a finite subset of the complete basis set. This is equivalent to cutting the infinite expansion Eq. (68) of the wave function after a certain term. This truncation of the expansion necessarily introduces some error into the description of the wave function. In other words, a finite basis set will always be incomplete. If we could use complete basis sets to expand the wave functions, every possible complete basis would do the job equally well. However, as we are limited to finite and thus incomplete sets, the choice of a reasonable one turns out to be critical for obtaining as good a representation of the wave functions as possible. There are various numerical methods based on the Kohn-Sham scheme which differ in the basis set they use to expand the wave functions, seeking a compromise between economy and precision. A similar situation as with the wave functions occurs also with the effective potential $v_{\text{eff}}(\vec{r})$. Again, the potential will be typically expressed as a linear combination of some functions from a suitably chosen finite basis set.

The idea behind augmented plane wave methods (APW) is to separate the space into two distinct regions: atomic spheres and the interstitial space. The atomic spheres are spheres centered at the positions of atomic nuclei $\vec{R}_\nu$, their radii ρ_ν being chosen so that the spheres would not overlap. The interstitial region is the remaining space between atoms outside all atomic spheres. The effective potential inside the atomic spheres is almost spherically symmetric but varies abruptly in the radial direction while the potential in the interstitial region lacks the spherical symmetry but varies only mildly. The APW basis functions are adjusted to the typical forms of the effective potential in the respective regions. Each basis function consists of a plane wave in the interstitial region and of an augmentation part inside each atomic sphere, the augmentation part being composed from spherical harmonics multiplied by some radial factor. Let us denote the interstitial region by I, i.e.,

$$\vec{r} \in I \Leftrightarrow (\forall \nu)\ |\vec{r} - \vec{R}_\nu| > \rho_\nu, \tag{69}$$

and the interior of the νth atomic sphere by S_ν, i.e.,

$$\vec{r} \in S_\nu \Leftrightarrow |\vec{r} - \vec{R}_\nu| < \rho_\nu. \tag{70}$$

Additionally, let us introduce spherical coordinates $(r_\nu, \theta_\nu, \phi_\nu)$ for each atomic sphere S_ν in such a way that

$$\vec{r} - \vec{R}_\nu = (r_\nu \sin\theta_\nu \cos\phi_\nu\ ,\ r_\nu \sin\theta_\nu \sin\phi_\nu\ ,\ r_\nu \cos\theta_\nu)\,. \tag{71}$$

The formula for the APW basis functions can be written in the following way then:

$$\chi_{\vec{k}}(\vec{r}) = \begin{cases} e^{i\vec{k}\cdot\vec{r}} & \text{if } \vec{r} \in I, \\ \sum_{lm} A_{lm}^{\vec{k},\nu} u_{\nu,l}(E, r_\nu) Y_{lm}(\theta_\nu, \psi_\nu) & \text{if } \vec{r} \in S_\nu. \end{cases} \tag{72}$$

The coefficients $A_{lm}^{\vec{k},\nu}$, which appear in the above expression, are subject to the constraint that the augmentation parts of the basis functions matches continuously the plane wave parts at the boundaries of the atomic spheres. The function $u_{\nu,l}(E, r_\nu)$ that determines the radial component of the basis function in the ν-th atomic sphere is a solution of the radial Schrödinger equation for energy E,

$$\left[-\frac{\hbar^2}{2m_e}\left(\frac{1}{r}\frac{d^2}{dr^2}r + \frac{l(l+1)}{r^2}\right) + v_\nu(r)\right] u_{\nu,l}(E, r) = E u_{\nu,l}(E, r), \tag{73}$$

the potential $v_\nu(r)$ being the spherical component of the effective potential inside that atomic sphere.

The drawback of the basis defined by Eq. (72) is that the radial functions $u_{\nu l}$, which are needed to build the basis, depend on the energy E that should equal the eigenenergy of the state whose wave function is to be expressed using that basis. That means that we should have a special basis for each one-particle state and that we would have to know the energy E so as to be able to create the basis before actually solving the Kohn-Sham equation. Imagine, however, that we decompose the energy-dependent radial functions into a Taylor series around a certain fixed energy E_0 and that we keep only the first two terms of the series, i.e., those which are constant and linear in energy, respectively. We get

$$u_{\nu,l}(E, r) \approx u_{\nu,l}(E_0, r) + \dot{u}_{\nu,l}(E_0, r)(E - E_0), \tag{74}$$

where the dot above the radial function denotes the first derivative with respect to energy,

$$\dot{u}_{\nu,l}(E, r) = \frac{du_{\nu,l}(E, r)}{dE}. \tag{75}$$

Now, the linearized augmented plane wave (LAPW) basis can be introduced [20] by means of the following prescription:

$$\chi_{\vec{k}}(\vec{r}) = \begin{cases} e^{i\vec{k}\cdot\vec{r}} & \text{if } \vec{r} \in I, \\ \sum_{lm} \left(A_{lm}^{\vec{k},\nu} u_{\nu,l}(E_0, r_\nu) + B_{lm}^{\vec{k},\nu} \dot{u}_{\nu,l}(E_0, r_\nu) \right) Y_{lm}(\theta_\nu, \psi_\nu) & \text{if } \vec{r} \in S_\nu. \end{cases} \tag{76}$$

The coefficients $A_{lm}^{\vec{k},\nu}$ and $B_{lm}^{\vec{k},\nu}$ in Eq. (76) has to be chosen in accord with the requirement that all the LAPW basis functions $\chi_{\vec{k}}(\vec{r})$ as well as their first derivatives should be continuous at the boundaries of all atomic spheres. The incorporation of the energy derivatives $\dot{u}_{\nu,l}$ into the expression for the basis functions $\chi_{\vec{k}}$ allows the wave functions φ_i to adjust their radial dependence inside the atomic spheres to a form that corresponds—in the linear approximation given by Eq. (74)—to the correct eigenenergy $E = E_i$ (rather than to E_0).

Another way to improve the APW basis set by utilizing the linearization of the type Eq. (74) consists in supplementing the set of basis functions with so-called local orbitals [21]. The resulting method (and the basis set) is usually referred to as APW+lo. Apart from the usual APW basis functions, which are given by Eq. (72) except that the radial parts are determined for a fixed energy E_0 rather than by the variable energy E, the APW+lo basis set contains one local orbital (at least, more local orbitals are possible as we will see) for each atomic sphere. The local orbital is given by

$$\chi_\nu^{(\mathrm{lo})}(\vec{r}) = \sum_{lm} \left(A_{lm}^{\nu} u_{\nu,l}(E_0, r_\nu) + B_{lm}^{\nu} \dot{u}_{\nu,l}(E_0, r_\nu) \right) Y_{lm}(\theta_\nu, \psi_\nu) \tag{77}$$

for $\vec{r} \in S_\nu$ and equals 0 outside the atomic sphere. The coefficients A_{lm}^{ν} and B_{lm}^{ν} are such that the functions $\chi_\nu^{(\mathrm{lo})}(\vec{r})$ are continuous at the atomic sphere boundary, their first derivative being possibly discontinuous there.

The augmented plane wave method and all its above discussed modifications have been designed to deal with valence electrons of extended systems, most often systems with some translational symmetry like crystals. The deeper lying electron states which form atomic cores are better treated by methods that have been developed for isolated atoms. Therefore the fixed energy E_0 that enters into the definition of the LAPW and the APW+lo basis should be set to a value appropriate for the description of the valence states. In practice, different values of E_0 may be chosen for different atoms in one and the same system and even for different angular quantum numbers l for the same atom, according to the expected position of the valence energy bands. In some instances, however, we may encounter electron states at energy levels that may be classified as semi-core. These energy levels are situated below the ordinary valence levels and the electrons in the semi-core states are accordingly more localized as compared to the valence electrons, yet they are not localized enough to justify their inclusion among the core electrons. The semi-core states must be handled by the (L)APW method along with the valence states. In such a case, it is not possible any more to find one fixed energy E_0 whose value would be close enough to the energy of all single-electron states of interest, both the semi-core and the valence. A possible resolution to the situation consists in taking an LAPW or APW+lo basis set adapted for the valence electrons and adding another local orbitals to it. The new local orbitals should be defined with the help of another fixed energy E_0', which is supposed to represent the semi-core levels well enough and which, of course, differs from the energy E_0 used for the valence states. The additional local orbitals for an APW+lo basis are defined in the same way as those given by Eq. (77) except that E_0 is replaced by E_0'. In the case of the LAPW method, the additional local orbitals assume the form

$$\chi_\nu^{(\mathrm{LO})}(\vec{r}) = \sum_{lm} \left(A_{lm}'^{\nu} u_{\nu,l}(E_0, r_\nu) + B_{lm}'^{\nu} u_{\nu,l}(E_0', r_\nu) + C_{lm}'^{\nu} \dot{u}_{\nu,l}(E_0', r_\nu) \right) Y_{lm}(\theta_\nu, \psi_\nu) \tag{78}$$

for $\vec{r} \in S_\nu$ and equal 0 otherwise, the coefficients $A_{lm}'^{\nu}$, $B_{lm}'^{\nu}$, and $C_{lm}'^{\nu}$ being chosen so as to ensure continuity up to the first derivative at the atomic sphere boundary.

The APW+lo and LAPW methods may be combined into one by defining the augmentation part of the basis functions according to the APW+lo prescription for some atoms and angular quantum numbers and according to the LAPW prescription for others. The APW+lo method typically requires less plane waves in the basis set as compared to the LAPW method to achieve the same level of precision. On the other hand, the APW+lo method enlarges the basis set by adding the local orbitals. The combination of the two methods allows one to get the advantages of both. The most important or most problematic atomic orbitals, which would impose the severest requirement on the number of plane waves, can be treated using the APW+lo method, thus sparing the number of plane waves, while the rest of the orbitals can be treated by the LAPW method, thus sparing the local orbitals.

The APW-like methods may be used either in the 'muffin-tin potential' approximation or as 'full-potential' methods. In the former case, the effective potential $v_{\mathrm{eff}}(\vec{r})$ is approximated by a constant in the interstitial region and by a spherically symmetric function inside the atomic spheres. In the latter case, no arbitrary assumption about the form of the effective potential is made. For those calculations described in this thesis that have been carried out by means of the LAPW and APW+lo method, the full-potential approach has always been used. In the full potential (L)APW method, the potential is represented by a Fourier series (plane-wave expansion) in the interstitial region and by an expansion into functions whose angular dependence is described by spherical harmonics inside the atomic spheres. Symmetry properties of the system under investigation may be exploited to simplify the representation of the potential. The same holds for the representation of the charge density. For more details on the LAPW and akin methods, see, e.g., the textbooks [22] and [23].

2.9 Linear muffin-tin orbital method in atomic sphere approximation

The linear muffin-tin orbital method simplifies the form of the effective potential by retaining only its spherically symmetric component inside each atomic (or 'muffin-tin') sphere. The atomic sphere approximation (ASA) simplifies the situation further by a complete neglect of the interstitial region. The usual requirement that the atomic spheres must not overlap is relaxed in the ASA. Instead, the radii of the spheres are chosen so that the total volume obtained by summation over atomic spheres would equal the volume of the whole system. The effective volume of the interstitial space is thus reduced to zero. The muffin-tin orbital basis functions are derived from functions $\chi_{\nu,lm}$ that solve the Schrödinger equation for the spherically symmetric potential inside the atomic spheres:

$$\chi_{\nu,lm}(E,\vec{r}) = u_{\nu,l}(E,r_\nu) Y_{lm}(\theta_\nu,\phi_\nu) \quad \text{for } \vec{r} \in S_\nu, \tag{79}$$

where $u_{\nu,l}(E,r_\nu)$ are solutions of the radial Schrödinger equation, Eq. (73), like in the case of the LAPW method. Outside the atomic spheres, the wave functions are supposed to satisfy the Laplace equation. This corresponds to electrons having zero kinetic energy. The neglect of the kinetic energy may seem to be a very crude approximation; however, realistic values of the kinetic energy would be indeed rather close to zero in the interstitial space, and since the interstitial space has effectively zero volume anyway, the rough description of the wave function in this region does not matter so much. There are two special forms of functions solving the Laplace equation in the spherical coordinates (centered at $\vec{R}_\nu$), namely

$$J_{\nu,lm}(\vec{r}) \propto (r_\nu)^l Y_{lm}(\theta_\nu,\phi_\nu) \tag{80}$$

and

$$K_{\nu,lm}(\vec{r}) \propto (r_\nu)^{-(l+1)} Y_{lm}(\theta_\nu,\phi_\nu). \tag{81}$$

The first set of functions, $J_{\nu,lm}(\vec{r})$, consists of solutions regular at $\vec{R}_\nu$ (the origin of the coordinate system), while the second set of functions, $K_{\nu,lm}(\vec{r})$, consists of functions divergent at the origin but falling off towards infinity. The complete form of the basis functions reads

$$\tilde{\chi}_{\nu,lm}(E,\vec{r}) = \begin{cases} N_{\nu,l}(E)\,\chi_{\nu,lm}(E,\vec{r}) + P_{\nu,l}(E)\,J_{\nu,lm}(\vec{r}) & \text{if } \vec{r} \in S_\nu, \\ K_{\nu,lm}(\vec{r}) & \text{otherwise.} \end{cases} \tag{82}$$

The function $\chi_{\nu,lm}$ that appears on the right-hand side of the above equation is given by Eq. (79). The energy-dependent prefactors $N_{\nu,l}(E)$ and $P_{\nu,l}(E)$, called the *normalization function* and the *potential function*, respectively, have to ensure that both the basis function $\tilde{\chi}_{\nu,lm}$ and its first radial derivative are continuous at the boundary of the atomic sphere.

The irregular solutions $K_{\nu,lm}$ of the Laplace equation centered at $\vec{R}_\nu$ extend into other atomic spheres centered at $\vec{R}_{\nu'}$ ($\vec{R}_{\nu'} \neq \vec{R}_\nu$), where they may be expanded into a linear combination of the regular solutions $J_{\nu',l'm'}$. The expansion, written as

$$K_{\nu,lm}(\vec{r}) = -\sum_{l'm'} S_{\nu lm;\nu' l'm'}\, J_{\nu',l'm'}(\vec{r}) \quad \text{for } \vec{r} \in S_{\nu'},\ \vec{R}_{\nu'} \neq \vec{R}_\nu, \tag{83}$$

serves as an implicit definition of the matrix elements $S_{\nu lm;\nu' l'm'}$. These elements—the *canonical structure constants*, as they are called—depend on the type of the crystal lattice only, rather than on any specifics of the effective potential. Consider now a one-electron wave function $\varphi_i(\vec{r})$, expressed as a linear combination of the basis functions,

$$\varphi_i(\vec{r}) = \sum_{\nu,lm} c_{\nu,lm}(E_i)\tilde{\chi}_{\nu,lm}(E_i,\vec{r}). \tag{84}$$

Suppose further, that we decompose the basis functions $\tilde{\chi}_{\nu,lm}$ according to Eq. (82) into terms containing the functions $J_{\nu,lm}$, $K_{\nu,lm}$ or $\chi_{\nu,lm}$. If we want to make the wave function $\varphi_i(\vec{r})$ satisfy the Schrödinger equation in all atomic spheres simultaneously, we have to require that the terms proportional to $J_{\nu,lm}$ cancel with those proportional to $K_{\nu',lm}$ inside each atomic sphere, leaving there only a linear combination of the functions $\chi_{\nu,lm}$ alone. This requirement can be translated into a matrix equation,

$$\sum_{\nu'\,l'm'} c_{\nu',l'm'}(E)\left(\delta_{\nu'l'm';\nu lm}P_{\nu,l}(E) - S_{\nu'l'm';\nu lm}\right) = 0, \tag{85}$$

which takes the place of the Schrödinger equation in the LMTO-ASA method.

Let us linearize the energy dependence of the basis functions in the spirit of Eq. (74), as we have already done for the LAPW basis. The linearization results into a special form of the potential function, which may be parameterized as

$$P_{\nu,l}(E) = \frac{E - C_{\nu,l}}{\Delta_{\nu,l} + \gamma_{\nu,l}(E - C_{\nu,l})}. \tag{86}$$

The potential parameters $C_{\nu,l}$, $\Delta_{\nu,l}$ and $\gamma_{\nu,l}$ are often referred to as the center, width, and distortion, respectively, of a supposed energy band with a $\chi_{\nu,l}$-like character. However, it should be emphasized that $C_{\nu,l}$, $\Delta_{\nu,l}$, and $\gamma_{\nu,l}$ describe the properties of the spherical part of the effective potential rather than describing the distribution of the energies $E = E_i$ that solve Eq. (85). Therefore the terminology that seems to relate the potential parameters to the properties of the band structure may be somewhat confusing.

After substituting the right-hand side of Eq. (86) into Eq. (85), the LMTO-ASA condition expressed by Eq. (85) can be rewritten so that it would pass into the standard problem of finding *eigenvalues* and *eigenvectors* of a matrix which may be interpreted as the Hamiltonian. Furthermore, there is a possibility to go over to a tight-binding (TB) version of the LMTO method by performing a so-called screening transformation of Eq. (85) and of the quantities involved therein (i.e. $P_{\nu,l}(E)$ and $S_{\nu lm;\nu'l'm'}$). The resulting TB-LMTO formulae are better suited for a numerical evaluation in comparison with their counterparts in the original LMTO method. Namely, the screened structure constants decay faster than the unscreened (canonical) ones as the distance $|\vec{R}_\nu - \vec{R}_{\nu'}|$ increases. The reader who would be interested in these and other details related to the TB-LMTO ASA formalism and its practical implementation may be referred, e.g, to [24].

2.10 Green's function

The single-particle time-independent Green's function of a quantum mechanical system—further to be called simply the Green's function—is defined as a z-dependent operator that satisfies the equation

$$\left(z - \hat{H}\right) \hat{G}(z) = \hat{I}, \tag{87}$$

where $\hat{H}$ is the single-particle Hamiltonian that characterizes the system of interest, for example

$$\hat{H} = -\frac{\hbar^2}{2m_e}\Delta_{\vec{r}} + v_{\text{eff}}(\vec{r}), \tag{88}$$

$\hat{I}$ stands for the identity operator, and z is a complex variable with the physical dimension of energy. Alternatively, the Green's function may be represented by a function of two spatial positions, $\vec{r}$ and $\vec{r}\,'$, apart from being a function of the complex variable z. After substituting the specific form of the Hamiltonian, Eq. (88), the analogy of Eq. (87) in this representation reads

$$\left(z + \frac{\hbar^2}{2m_e}\Delta_{\vec{r}} - v_{\text{eff}}(\vec{r})\right) G(\vec{r}, \vec{r}\,'; z) = \delta(\vec{r} - \vec{r}\,'). \tag{89}$$

The symbol δ on the right-hand side of Eq. (89) denotes the Dirac function. The two representations may be considered equivalent, if we describe the action of an operator in terms of convolution with an appropriate kernel function:

$$\left[\hat{G}(z) f\right](\vec{r}) = \int G(\vec{r}, \vec{r}\,'; z)\, f(\vec{r}\,')\, d^3r'. \tag{90}$$

There is a close relationship between the Green's function and the spectrum of eigenstates belonging to the corresponding Hamiltonian. Owing to this relationship, the local density of states—see Eq. (28)—can be expressed in terms of the Green's function as

$$\rho(\vec{r}, E) = -\frac{1}{\pi} \lim_{\varepsilon \to 0+} \operatorname{Im} G(\vec{r}, \vec{r}; E + i\varepsilon). \tag{91}$$

Since the one-particle electron density, which is the central quantity in the DFT, follows from the local density of states by integration over the energy E up to the Fermi level E_F, it is possible to base DFT calculations on the Green's function instead of working with the Kohn-Sham orbitals directly.

Let us now turn attention to the systems that involve some kind of translational symmetry. The translational symmetry of the system is reflected in the properties of its Green's function, which has to satisfy the relation

$$G(\vec{r}, \vec{r}\,'; z) = G(\vec{r} + \vec{T}, \vec{r}\,' + \vec{T}; z), \tag{92}$$

where T_ν is any lattice vector, i.e., a vector such that every two atomic positions $\vec{R}_\nu$ and $\vec{R}_\nu + \vec{T}$ are equivalent. A natural means of description for these systems is provided by a Green's function that depends on the Bloch wave vector $\vec{k}$. The $\vec{k}$-dependent Green's function can be obtained from the so far considered Green's function $G(\vec{r}, \vec{r}\,'; z)$ through the discrete Fourier transform,

$$G_{\vec{k}}(\vec{r}, \vec{r}\,'; z) = \sum_{\vec{T}} G(\vec{r}, \vec{r}\,' + \vec{T}; z)\, e^{i\vec{k}\cdot\vec{T}}, \tag{93}$$

where the summation runs over all lattice vectors $\vec{T}$. In analogy to the local density of states, as expressed by Eq (91), we can define the *Bloch spectral density* (or $\vec{k}$-resolved local density of states), $\rho_{\vec{k}}(\vec{r}, E)$, with the help of the k-dependent Green's function:

$$\rho_{\vec{k}}(\vec{r}, E) = -\frac{1}{\pi} \lim_{\varepsilon \to 0+} \operatorname{Im} G_{\vec{k}}(\vec{r}, \vec{r}; E + i\varepsilon). \tag{94}$$

The concept of various spectral densities defined with the help of the Green's functions can be further generalized by introducing a spectral density projected on an arbitrary basis function or set of basis functions. As an example, we may consider an lm-projected spectral density, defined in terms of the lm-resolved local orbitals $\chi_{\nu,lm}(E, \vec{r})$ of the LMTO method, or, more generally, in terms of any suitable complete set of lm-resolved basis functions $\chi_{j,lm}(\vec{r})$. The lm-projected (lm-resolved) density of states is then given by the equation

$$\rho_{lm}(E) = -\frac{1}{\pi} \lim_{\varepsilon \to 0+} \operatorname{Im} \sum_j \int\!\!\int \chi^*_{j,lm}(\vec{r})\, G(\vec{r}, \vec{r}\,'; E + i\varepsilon)\, \chi_{j,lm}(\vec{r}\,')\, d^3r\, d^3r'. \tag{95}$$

Similarly, a spectral density projected on a particular atomic sphere can be introduced within the ASA approximation, or a spectral density that is simultaneously projected on a particular atomic sphere *and* on the spherical harmonic of particular l and m. The spectral density projected on one particular atomic sphere is equivalent to the local density of states integrated over that atomic sphere.

2.11 Coherent potential approximation

Substitutional alloys or systems that contain such alloys as their part (the Invar alloy, tungsten surface covered by a two-dimensional alloy composed from $3d$ transitional metals) will be of special interest in this theses. The substitutional disorder introduces an element of randomness into the properties of these systems and removes their transitional invariance. It would be obviously a vain effort to seek an exact description of every possible arrangement of atoms in the alloy. Instead, it appears more reasonable to look for some averaged characteristics of the random system. An important example of such an averaged quantity is the average Green's function $\bar{G}(z)$,

$$\bar{G}(z) = \sum_C p(C) \hat{G}_C(z), \tag{96}$$

The sum in the above definition includes all possible configurations of atoms in the alloy, $p(C)$ denotes the probability of realizing the configuration C, and $\hat{G}_C$ is the Green's function associated with that particular configuration. The knowledge of the configurationally averaged Green's function allows one to find the average value of an arbitrary one-electron observable quantity, which makes $\bar{G}(z)$ a particularly useful characteristics. In contrast to $\bar{G}(z)$, the configurational average of, say, a single-electron wave function turns out to be devoid of any physical significance. The Green's function formalism therefore provides an indispensable tool for handling random systems like the substitutional alloys.

Although a substitutional alloy itself lacks the translational symmetry, it is built on a translationally symmetric crystal lattice. Even two different lattice sites which are inequivalent in some particular configurations—because they are actually occupied by different atoms—may be still equivalent in the statistical sense—meaning that the probability of being occupied by a particular atom would be the same for both sites. If the alloy retains the translational symmetry at least in this statistical sense, the configurationally averaged Green's function will reflect this fact by conforming to Eq. (92). It is therefore meaningful to speak of, e.g, the $\vec{k}$-resolved density of states even in the case of the substitutional alloys, provided that the Fourier transform of the averaged Green's function $\bar{G}_{\vec{k}}(\vec{r},\vec{r}\,';z)$ is used in the definition, Eq. (94).

We may write a formal expression for the averaged Green's function in analogy to Eq. (89) if we replace the actual effective potential v_{eff} by a suitable operator $\hat{\Sigma}(z)$. Then we get

$$\int d^3r'' \left[\delta(\vec{r}-\vec{r}\,'')\left(z+\frac{\hbar^2}{2m_e}\Delta_{\vec{r}\,''}\right)-\Sigma(\vec{r},\vec{r}\,'';z)\right]G(\vec{r}\,'',\vec{r}\,';z)=\delta(\vec{r}-\vec{r}\,'). \qquad (97)$$

The above equation, Eq. (97), can be considered an implicit definition of the operator $\hat{\Sigma}(z)$, conventionally called 'the self-energy'. The self-energy represents an effective potential of a fictional non-random system that would have the same Green's function as is the configurationally averaged Green's function of the alloy. We can assume this fictional system, as characterized by $\hat{\Sigma}$ and $\bar{G}(z)$, to be an unperturbed system, while the difference $\hat{V}_C-\hat{\Sigma}(z)$ between the actual effective potential of a particular configuration and the self-energy represents a perturbation. This approach leads to the Dyson equation for the perturbed Green's function,

$$\hat{G}_C(z)=\bar{G}(z)+\hat{G}_C(z)\,\left(\hat{V}_C-\hat{\Sigma}(z)\right)\,\bar{G}(z). \qquad (98)$$

The perturbed Green's function is nothing else but the actual configuration-dependent Green's function of the alloy. If we introduce a configuration-dependent scattering operator $\hat{T}_C(z)$ as

$$\hat{T}_C(z)=\left[\hat{I}-\left(\hat{V}_C-\hat{\Sigma}(z)\right)\,\bar{G}(z)\right]^{-1}\left(\hat{V}_C-\hat{\Sigma}(z)\right), \qquad (99)$$

we are able to restate Eq. (98) in the form

$$\hat{G}_C(z)=\bar{G}(z)+\bar{G}(z)\,\hat{T}_C(z)\,\bar{G}(z), \qquad (100)$$

and by averaging both sides of Eq. (100) over all possible configurations, we eventually obtain (for all z)

$$\sum_C p(C)\,\hat{T}_C(z)=0. \qquad (101)$$

The last condition imposed on the scattering operators is exact. The *coherent potential approximation* (CPA) [25] relies on the assumption that the scattering matrix and the self-energy can be decomposed into a sum of localized single-site contributions,

$$\hat{T}_C(z)=\sum_\nu \hat{t}_\nu(C;z) \qquad (102)$$

and

$$\hat{\Sigma}(z) = \sum_{\nu} \hat{\mathcal{P}}_{\nu}(z), \tag{103}$$

respectively, and that the local scattering operators $\hat{t}_{\nu}(z)$ depend exclusively on which atom resides at the atomic position $\vec{R}_{\nu}$, no matter what the configuration of atoms at the other sites may be. The site-localized contribution to the self-energy, $\hat{\mathcal{P}}_{\nu}(z)$, is referred to as the *coherent potential function*, hence the name of the approximation. The local scattering operator at a particular site can be expressed in terms of a site-localized perturbation, which is identified with the difference between the coherent potential function and the effective potential induced by the actual atom that occupies the site. We thus finally obtain the CPA condition for each atomic site $\vec{R}_{\nu}$ in the form

$$\sum_{X} c_{\nu}(X) \left[\hat{I} - \left(v_X - \hat{\mathcal{P}}_{\nu}(z)\right) \bar{G}(z)\right]^{-1} \left(v_X - \hat{\mathcal{P}}_{\nu}(z)\right) = 0, \tag{104}$$

where X stands for the various types of atoms that may occupy the position $\vec{R}_{\nu}$, the coefficient $c_{\nu}(X)$ represents the probability that the position $\vec{R}_{\nu}$ will be occupied by atom X, and v_X is the (effective) potential induced by the presence of atom X in that position. The coefficients $c_{\nu}(X)$ are obviously proportional to the respective concentrations of constituting elements in the alloy. An electronic structure calculation carried out for a substitutional alloy in the CPA thus amounts to finding self-consistent solutions for the configurationally averaged Green's function $\bar{G}(z)$ and the coherent potential fuctions $\hat{\mathcal{P}}_{\nu}(z)$ so that they would conform to Eq. (98), Eq. (103), and Eq. (104) simultaneously. The formulas of the CPA can be translated into the language of the LMTO-ASA method without difficulty. The CPA is actually available within the LMTO software that has been applied for the purposes of this theses. The LMTO-ASA method has to be expressed in terms of the Green's functions so that the CPA approach would be applicable within that method. The re-formulation of the LMTO-ASA method into the Green's function language is outlined in the following section.

2.12 Surface Green's functions in the TB-LMTO method

The LMTO method in the atomic sphere approximation can be re-formulated in terms of the Green's function. The Green's function formulation turns the method into a particularly useful tool for studying disordered systems like alloys (with the help of the CPA) and also for studying surfaces and interfaces (with the help of the *surface Green's function method*, which is going to be described in this section). The Green's function connecting $\vec{r} \in S_{\nu}$ with $\vec{r}\,' \in S_{\nu'}$ can be expanded for the purpose of the LMTO-ASA method in the following way:

$$\begin{aligned} G(\vec{r}, \vec{r}\,'; z) = &-\delta\nu\nu' \sum_{lm} \chi_{\nu,lm}(z; \vec{r}^{<}) \chi'_{\nu,lm}(z; \vec{r}^{>}) + \\ &+ \sum_{lm,l'm'} \chi_{\nu,lm}(z; \vec{r}) G_{\nu lm;\nu' l'm'}(z) \chi_{\nu',l'm'}(z; \vec{r}\,'). \end{aligned} \tag{105}$$

In the above prescription for the LMTO-ASA Green's function, $\chi_{\nu,lm}(z;r)$ and $\chi'_{\nu,lm}(z;r)$ are, respectively, the regular and the irregular solution of the Schrödinger equation for the spherically symmetric potential inside the atomic sphere S_ν, the angular dependence of which is characterized by the quantum numbers l and m; $\vec{r}^<$ denotes that one of the vectors $\vec{r}$ and $\vec{r}'$ that points to a position closer to the center of S_ν, and $\vec{r}^>$ denotes the vector that points to a position farther from the center of S_ν. Each regular solution $\chi_{\nu,lm}(z;\vec{r})$ is normalized to unit norm, $\int |\chi_{\nu,lm}(z;\vec{r})|^2 d^3r = 1$, provided that the integral is performed over the respective atomic sphere. The irregular solutions are chosen in such a way that their values and their first spatial derivatives in the radial direction smoothly match the corresponding first energy derivative $\dot{\chi}_{\nu,lm}(z;\vec{r}) \equiv d\chi_{\nu,lm}(z;\vec{r})/dz$ of the regular solution on the boundary of the respective atomic sphere.

Furthermore, the physical Green's function matrix $G_{\nu lm;\nu' l' m'}(z)$ can be expressed in terms of the auxiliary Green's function matrix $g_{\nu lm,\nu' l' m'}$(z);

$$G_{\nu lm;\nu' l' m'}(z) = \lambda_{\nu l}(z)\delta_{\nu\nu'}\delta_{ll'}\delta_{mm'} + \mu_{\nu l}(z) g_{\nu lm;\nu' l' m'}(z)\mu_{\nu' l'}(z), \tag{106}$$

where the quantities $\lambda_{\nu l}$ and $\mu_{\nu l}$ are fully determined by the respective potential function $P_{\nu l}(z)$ (see section 2.9) and its derivatives with respect to z. The matrix $g(z)$ with elements $g_{\nu lm;\nu' l' m'(z)}$ (where the indices ν, l, m identify the row and the indices ν', l', m' identify the column) is called *auxiliary Green's function matrix.* This auxiliary Green's function matrix can be calculated by performing the matrix inversion,

$$g(z) = \left(P\left(z\right) - S\right)^{-1}. \tag{107}$$

In the above matrix equation, $P(z)$ denotes a diagonal matrix with elements $P_{\nu lm;\nu' l' m'}(z) = P_{\nu l}(z)\delta_{\nu\nu'}\delta_{ll'}\delta_{mm'}$ and S denotes the matrix of the canonical structure constants $S_{\nu lm;\nu' l' m'}$.

The so-called screening transformation allows one to transform the canonical quantities (like the structure constants, potential functions, auxiliary Green's function matrices, and the parameters λ and μ), which appear in Eq. (106) and Eq. (107), into their screened counterparts. The advantage of this transformation is that suitably screened structure constants are substantially different from zero only for a limited site-to-site distance, i.e. only for ν and ν' for which $|\vec{R}_\nu - \vec{R}_{\nu'}|$ is small enough. The screening transformation thus brings us to the tight-binding version of the LMTO method (TB-LMTO). The form of Eqs. (106) and (107) remains unchanged if all the canonical quantities in these equations are systematically replaced by the screened ones. The physical Green's function matrix is invariant with respect to the screening transformation.

The short-range character of the screened structure constants, which incorporate all the inter-site interactions in the TB-LMTO equations, plays a crucial role in establishing so-called *principal layers* and, consequently, in the successful application of the *surface Green's function* formalism. The surface Green's functions will allow us to cope with layered systems, surfaces, interfaces, and, in general, with any infinite or semi-infinite systems that lack the translational symmetry in one direction. Here, we are particularly interested in surfaces. Crystal surfaces possess a translational symmetry in the directions along the surface; even surfaces of substitutional alloys exhibit at least a translational symmetry of their configurationally averaged Green's function $\bar{G}(\vec{r},\vec{r}\,';z)$ and the corresponding averaged auxiliary Green's function matrix $\bar{g}_{\nu lm;\nu' l' m'}(z)$. However, their is no translational symmetry (spatial periodicity) in the direction perpendicular to the surface. We can thus perform the Fourier transformation of the Green's functions in the directions parallel to the surface plane. The Fourier transformation leaves us with $\vec{k}_{\|}$-dependent Green's function matrices $G_{\nu lm;\nu' l' m'}(\vec{k}_{\|},z)$, whose indices ν and ν' are limited to inequivalent sites in one surface unit cell. Since the surface unit cell is nevertheless infinite in the direction perpendicular to the surface, the $\vec{k}_{\|}$-dependent Green's function matrices still have to be infinite. The infinite range of the matrix indices prevents a direct numerical implementation of the matrix inversion indicated in Eq. (107).

The division of the system into principal layers and the use of the surface Green's function formalism offers a solution to the above discussed obstacle. Each principal layer consists of one or several atomic layers. The number of atomic layers in one principal layer is determined by the requirement that the screened structure constants $S_{\nu lm;\nu' l' m'}$ connecting different sites ν and ν' can be non-negligible only for sites within one principal layer or in two directly neighboring principal layers. Let us re-label the elements of the fundamental matrices that enter the TB-LMTO formulas as $g_{p\nu lm;p'\nu' lm}(z)$, $P_{p\nu lm;p'\nu' lm}(z)$, $S_{p\nu lm;p'\nu' lm}$, etc., where the indices p and p' refer to a specific principal layer while the site indices ν and ν' are now restricted to sites within the given principal layer. Further, let $g_{p,p'}(\vec{k}_{\|},z)$, $P_{p,p'}(\vec{k}_{\|},z)$, and $S_{p,p'}(\vec{k}_{\|})$ denote sub-matrices with elements $g_{p\nu lm;p'\nu' lm}(\vec{k}_{\|},z)$, $P_{p\nu lm;p'\nu' lm}(\vec{k}_{\|},z)$, and $S_{p\nu lm;p'\nu' lm}(\vec{k}_{\|})$, respectively, in which ν, l, and m are considered to be the row indices, ν', l', and m' are considered to be the column indices, ν and ν' are confined to non-equivalent sites within one principal layer, and the principal-layer indices p and p' refer to different sub-matrices. These sub-matrices are finite. The sub-matrix $g_{p,p}$ of the auxiliary Green's function matrix can be evaluated with the help of the so-called surface Green's functions (or surface Green's function matrices here) $G^{>}_{p+1}$ and $G^{<}_{p-1}$, associated with the neighboring principal layers. The dependence of the Green's functions on z and $\vec{k}_{\|}$ is omitted here for the sake of brevity. The equation that relates $g_{p,p}$ to the surface Green's functions in TB-LMTO reads

$$g_{p,p} = \left(P_{p,p} - S_{p,p} - S_{p,p+1}G^{>}_{p+1}S_{p+1,p} - S_{p,p-1}G^{<}_{p-1}S_{p-1,p}\right)^{-1}. \tag{108}$$

The surface Green's functions (matrices) can be in principle found by using the recursive relations

$$G^{>}_{p} = \left(P_{p,p} - S_{p,p} - S_{p,p+1}G^{>}_{p+1}S_{p+1,p}\right)^{-1}, \tag{109a}$$

and

$$G^{<}_{p} = \left(P_{p,p} - S_{p,p} - S_{p,p-1}G^{<}_{p-1}S_{p-1,p}\right)^{-1}. \tag{109b}$$

2.13 Surface magnetic anisotropy

When we handle a spin-polarized system within the LSDA (as briefly described in chapter 2.7), we do not consider any connection between the orientation of the spin magnetic moments and a specific direction in the Euclidean space. The labels ‘up’ and ‘down’, chosen for the majority and minority spin orientation, respectively, are utterly arbitrary. In reality, however, there is typically a preferred direction in which the magnetic moments tend to align themselves. The two main mechanisms that determine this preferred direction—called the *‘easy magnetization axis’*—are the spin-orbit coupling and the dipole-dipole magnetic interaction. Let us first turn our attention to the spin-orbit coupling. The formulas concerning this effect that will be presented here are mostly taken from [26], sometimes with an altered notation.

The spin-orbit coupling (spin-orbit interaction) is a relativistic effect. In order to account for it, we have to replace the Schrödinger equation, Eq. (56), with the Dirac equation,

$$\left(-i\hbar c\vec{\alpha}\cdot\nabla + m_e c^2\beta + v(\vec{r})\right)\psi = (m_e c^2 + E)\psi, \tag{110}$$

where $\vec{\alpha}$ is a three-component vector, whose components are constant 4×4 matrices, β is another constant 4×4 matrix, and ψ is, accordingly, a 4-component wave function. The prescription for the constant matrix factors reads

$$\vec{\alpha} = \begin{pmatrix} 0 & \vec{\sigma} \\ \vec{\sigma} & 0 \end{pmatrix}, \tag{111}$$

where the 2×2 blocks $\vec{\sigma}$ are the Pauli matrices

$$\sigma_x = \begin{pmatrix} 0 & 1 \\ 1 & 0 \end{pmatrix}, \quad \sigma_y = \begin{pmatrix} 0 & -i \\ i & 0 \end{pmatrix}, \quad \sigma_z = \begin{pmatrix} 1 & 0 \\ 0 & -1 \end{pmatrix},$$

and

$$\beta = \begin{pmatrix} I & 0 \\ 0 & -I \end{pmatrix},$$

where

$$I = \begin{pmatrix} 1 & 0 \\ 0 & 1 \end{pmatrix}.$$

The energy E in Eq. (110) is an excess energy over the rest energy $m_e c^2$ of the electron and stands for one of the single-particle energies E_i of the Kohn-Sham equation. The 4-component wave function ψ, which may be expanded as

$$\psi = \begin{pmatrix} \psi^{+\uparrow} \\ \psi^{+\downarrow} \\ \psi^{-\uparrow} \\ \psi^{-\downarrow} \end{pmatrix}, \tag{112}$$

replaces the Kohn-Sham orbitals of the spin-polarized DFT. The contribution of one particular one-electron wave function ψ to the spin-resolved electron density is simply

$$n^{\uparrow} = \left|\psi^{+\uparrow}\right|^2 + \left|\psi^{-\uparrow}\right|^2, \tag{113a}$$

$$n^{\downarrow} = \left|\psi^{+\downarrow}\right|^2 + \left|\psi^{-\downarrow}\right|^2. \tag{113b}$$

In the above employed representation, the ‘up’ and ‘down’ spins were defined with respect to a magnetization axis that was parallel to the z direction. So as to orient the referential magnetization axis in some other direction, the vector of matrices $\vec{\alpha}$ has to be rotated accordingly. The choice of the particular representation does not matter too much when solving the Dirac equation itself, because one can always easily transform from one representation into another. However, the orientation of the magnetization axis becomes important in a DFT calculation, in which the four-component wave function ψ serves to construct the spin-polarized electron densities, as prescribed by Eqs. (113). Unless the actual magnetization axis is *a priori* known, the calculation has to be performed for several different orientations of the axis so as to find out the one that renders the lowest total energy for the investigated system.

Separating the 'large' components $\psi^{+\uparrow}$ and $\psi^{+\downarrow}$ of the wave function in Eq. (110) yields

$$\vec{\sigma} \cdot \nabla \left(-\frac{\hbar^2}{2m_e} \right) \left(1 + \frac{E - v(\vec{r})}{2m_e c^2} \right)^{-1} \vec{\sigma} \cdot \nabla \psi^+ = \left(E - v(\vec{r}) \right) \psi^+, \tag{114}$$

where

$$\psi^+ = \begin{pmatrix} \psi^{+\uparrow} \\ \psi^{+\downarrow} \end{pmatrix}.$$

After using the approximations

$$\left(1 + \frac{E - v}{2m_e c^2} \right)^{-1} \approx 1 - \frac{E - v}{2m_e c^2} \tag{115}$$

and

$$\frac{E - v}{2m_e c^2} \psi^+ \approx -\frac{\hbar^2}{4m_e^2 c^2} \Delta \psi^+ \tag{116}$$

(where $\Delta = \nabla^2$ is the Laplace operator), we get

$$-\frac{\hbar^2}{2m_e} \left\{ \Delta\psi^+ + \frac{1}{2m_e c^2} \left[\frac{\hbar^2}{2m_e} \Delta^2 \psi^+ + \frac{1}{2m_e c^2} (\nabla v) \cdot (\nabla \psi^+) + \right. \right.$$
$$\left. \left. + \frac{i}{2m_e c^2} \left(\vec{\sigma} \cdot \left[(\nabla v) \times \nabla \psi^+ \right] \right) \right] + v(\vec{r}) \psi^+ \right\} = E \psi^+. \tag{117}$$

The terms in the big square brackets on the left-hand side of Eq. (117) represent the relativistic corrections to the Schrödinger equation. The relativistic corrections are usually important near the atomic nuclei only, because only there the electrons have enough kinetic energy to approach the relativistic regime. The effective potential $v(\vec{r})$ around the nuclei tends to be almost spherically symmetric. Exploiting the spherical symmetry of the potential allows us to rewrite the last term of the relativistic correction as

$$-\frac{i\hbar^2}{4m_e^2 c^2} \left(\vec{\sigma} \cdot \left[(\nabla v) \times \nabla \psi^+ \right] \right) \longrightarrow \frac{1}{2m_e^2 c^2 r} \left(\frac{dv}{dr} \right) \left(\vec{s} \cdot \vec{L} \right) \psi^+, \tag{118}$$

where

$$\vec{s} = \frac{\hbar}{2} \vec{\sigma} \tag{119}$$

is the spin moment operator and

$$\vec{L} = -i\hbar \vec{r} \times \nabla \tag{120}$$

is the orbital moment operator.

If the relativistic corrections have to be taken into account, the effective DFT potential $v_{\text{eff}}(\vec{r})$ is substituted for $v(\vec{r})$ into Eq. (117). This equation assumes the role of the Kohn-Sham equation. As soon as Eq. (117) for the 'large' part of the electron wave function is solved, the 'small' components $\psi^{-\uparrow}$ and $\psi^{-\downarrow}$ can be also easily found from the Dirac equation, Eq. (110). Then the spin-resolved electron densities can be calculated according to Eq. (113) and summed over all one-electron states below the Fermi level. Because of the spin-orbit coupling, however, the electron spin is no more a good quantum number; Eq. (117) cannot be solved for the 'up' and 'down' spin components separately. Therefore the basis set needed to set up and solve the eigenvalue problem would have to contain twice as much basis functions so as to cover both spin components at once. In order to keep the number of the basis functions in the LAPW/APW+lo computational scheme at a reasonable level, the *second variational treatment* may be used to carry out the relativistically-corrected calculation. The second-variational treatment is based upon the *scalar relativistic approximation*. This approximation consists in omitting the spin-orbit term in Eq. (117). As a first step of the second-variational scheme, the eigenfunctions in the scalar relativistic approximation are found. This scalar relativistic wave functions are then used as basis functions in the second step, which already takes into account all relativistic corrections including the spin-orbit coupling. The effective Hamiltonian of the second step is simplified by the fact that except for the spin-orbit part the Hamiltonian is already diagonal in the basis of the scalar relativistic wave functions. On the one hand, one cannot avoid doubling the basis set in the second step of the second-variational treatment because both spin components have to be included. On the other hand, the basis set needs contain significantly fewer scalar relativistic wave functions than how many augmented plane waves or other simple basis functions it would have to contain if the scalar relativistic wave functions were not used. Let me finally mention another point regarding calculations based on the linearized augmented plane waves, like LAPW and APW+lo: The augmentation parts of the basis functions have to be determined before the eigenvalue problem is solved. This is also done by applying the scalar relativistic approximation and using the symmetric part of the effective potential inside the atomic spheres.

The spin-orbit interaction that couples the electron spin to the spatial part of the electron wave function is one source of the magnetic anisotropy. The next to be mentioned here is the magnetic dipole-dipole interaction. Imagine a sample of an investigated material as a collection of magnetic point dipoles, each associated with one atom of the sample. The replacement of the atomic moments with point dipoles is a reasonable approximation, considering that a prevailing portion of the total magnetic moment is localized near the atomic nuclei. The contribution of the magnetic dipole-dipole interaction to the total energy amounts to

$$E_{dd} = \frac{\alpha}{2} \sum_{\substack{i,j=1 \\ (i \neq j)}}^{N_A} \left(\frac{\vec{\mu}_i \cdot \vec{\mu}_j}{|\vec{R}_{ij}|^3} - \frac{3\left(\vec{\mu}_i \cdot \vec{R}_{ij}\right)\left(\vec{\mu}_j \cdot \vec{R}_{ij}\right)}{|\vec{R}_{ij}|^5} \right), \tag{121}$$

where the summation indices i and j go over all atoms with a non-zero magnetic moment, $\vec{\mu}_i$ is the magnetic moment associated with the i-th atom, and the vector

$\vec{R}_{ij}$ describes the position of the atomic nucleus denoted by index i with respect to the atomic nucleus denoted by index j, $\vec{R}_{ij} = \vec{R}_i - \vec{R}_j$. If the magnitudes of the magnetic moments are expressed as multiples of the Bohr magneton μ_B, the coefficient α in Eq. (121) is

$$\alpha = \frac{\mu_0 \mu_B^2}{4\pi} \approx 8.60 \times 10^{-54}\,\mathrm{Jm}^3 \approx 5.37 \times 10^{-8}\,\mathrm{eV(nm)}^3, \tag{122}$$

μ_0 being the vacuum permeability. Naturally, the energy E_{dd} given by the sum on the right-hand side of Eq. (121) is, up to some higher-order corrections, directly proportional to the number of atoms N_A in the sample of a ferromagnetic material (or to the volume of the sample), so the contribution to the total energy per one atom (or per unit volume) is independent from the actual size of the sample provided that the sample is large enough. However, the sum over either of the two indices i and j in Eq. (121) is only conditionally convergent if the volume of a three-dimensional system is sent to infinity. As a consequence, E_{dd} per atom depends not only on the atomic structure but also on the macroscopic shape of the sample (or on the shape of magnetic domains if the sample is divided into more such domains). This contribution to the magnetic anisotropy is referred to as the *'shape anisotropy'*. Fortunatelly, the sum is absolutely convergent for two-dimensional systems like surfaces, in which we will be interested. The dependence of the anisotropy on the shape of the sample thus disappears. Let us assume that all magnetic atoms on the surface are equivalent and that they are arranged on a square lattice with a lattice parameter $a_\parallel$. Let us further consider a ferromagnetic system. The local magnetic moments of the surface atoms then all have the same magnitude and the same direction, $\vec{\mu}_i = \vec{\mu}$. We may expect the magnetic moments to be oriented either in the surface plane or perpendicular to it. The difference in energy per surface atom between the two orientations of the magnetic moments then amounts to

$$E_\parallel - E_\perp = -\frac{3\alpha\mu^2}{2a_\parallel^3} \sum_{n_x,n_y} \frac{n_x^2}{\left(n_x^2 + n_y^2\right)^{5/2}} \tag{123}$$

due to the dipole-dipole interaction. The summation indices n_x and n_y in Eq. (123) play the role of atomic coordinates on the surface. They go through all integers up to ∞ and down to $-\infty$ except for the case $n_x = n_y = 0$.

The contributions from the spin-orbit coupling and the dipole-dipole interaction have to be put together in order to determine the magnetization direction that leads to the lowest total energy. One thus eventually arrives at the easy magnetization axis, which represents the direction of spontaneous magnetization in the ground state of the studied system.

3 $Fe_{64}Ni_{36}$ (Invar) surface (001)

Invar, an alloy of about 65 atomic percent iron and 35 at. % nickel, is well known for exhibiting nearly zero thermal expansion in a wide range of temperatures. This feature makes Invar a technologically important material, which can be used for constructing precise devices that are supposed to retain stable parameters independent from temperature changes. Invar was discovered by C. E. Guillaume in 1897 and its importance for precision measurements in physics was acknowledged by awarding the Nobel Prize to the discoverer in 1920. The unusual thermal behavior of this material is a consequence of two opposing tendencies that govern the temperature dependence of the specific volume of the alloy and that nearly compensate each other. One the one hand, there is the usual thermal expansion due to the lattice anharmonicity, on the other hand, there is also a tendency to contraction of the volume with increasing temperature. The latter tendency is closely related to complex magnetic properties of the FeNi alloys.

The traditional explanation of the anomalous thermal expansion is that there exist two different magnetic states—usually referred to as a low-moment state and a high-moment state—of the alloy in the vicinity of the Invar composition [27]. The high-moment state, which is stable at lower temperatures, is characterized by a smaller volume per atom as compared to the low-moment state, which occurs at higher temperatures. A thermally induced transition from the high-moment to the low-moment state then leads to the so called Invar effect, i.e. to the negative thermal expansion. There are still some disputed ditails concerning the two magnetic states and the transition between them or even doubts about the existence of a sharp transition between two distinguishable magnetic states [28, 29]. It is, however, not the aim of this thesis to deal with the unresolved questions of the Invar effect or with the complexities of the magnetic order in this alloy. We will focus here on the surface properties of the $Fe_{64}Ni_{36}$ alloy and, in particular, on the interpretation of an STM experiment on the surface of this technologically important material.

The atoms that form the $Fe_{64}Ni_{36}$ alloy are arranged on a face centered cubic (fcc) lattice. Any lattice site may be, in principle, randomly occupied by either an iron or a nickel atom. The chemical disorder removes the symmetries of the fcc lattice. However, there can be still found some degree of short range order (see, e.g., [29]) in the composition of the alloy. At zero temperature, the alloy is essentially ferromagnetic with possible small non-collinearity or even a small fraction of antiferromagnetically aligned local spin moments due to locally iron-enriched areas, in which a tendency to the antiferromagnetic state known from pure fcc iron can be expected.

It is in general more difficult to achieve atomic resolution with STM on metallic surfaces in comparison with the imaging of semiconductor surfaces or surfaces covered by some non-metallic adsorbate. The delocalization of conductive electrons in metals leads to a smooth electron density not only in the bulk but also above the metallic surfaces, resulting into a rather low contrast in STM images. In spite of the relative difficulty of the task, individual atoms on metal surfaces has been successfully imaged in many cases, including the close-packed surfaces—e.g. the gold

(111) surface [30] became the first such surface for which the atomic resolution was achieved. Surfaces of various alloys have been imaged by STM too and chemical resolution at atomic level has been achieved in some cases like for PtNi(111) [31], PtRh(100) [32], and PtCo(100) [33], i.e., atoms of different elements were distinguished from each other on these surfaces. When investigating disordered structures like alloys, the STM as a local-probe method is an especially valuable tool. It enables one to study phenomena like short-range ordering, clustering, surface segregation, etc., in a real-space picture. So as to utilize the information offered by the STM experiments, it is, however, always necessary to begin with the most basic analysis that consists in identifying the patterns observed in images (and spectra) with real objects on the surface. Such questions have to be answered as: Do apparent elevations observed in the image correspond to real atoms (normal contrast) or do they rather correspond to interatomic positions while the atoms themselves are imaged as depressions (reversed contrast)? Can we distinguish atoms of different elements on the surface, and if so, which type of atom seen in the picture should we attribute to which element? Is a certain observed feature directly related to the composition of the topmost atomic layer and to the arrangement of atoms therein or does the feature rather originate from the properties of the sub-surface atomic layer or layers? A theoretical study of the imaged system can help us to solve many questions like those above.

The following sections of this chapter are devoted to the theoretical analysis of an experimental study that has been carried out at the *Institut für Allgemeine Physik* of the Vienna University of Technology. The study involved an investigation of the $Fe_{64}Ni_{36}$ (001) alloy surface using the techniques of the STM and scanning tunneling spectroscopy (STS). In Section 3.1, I will sketch the main achievements of the experimentalists regarding the $Fe_{64}Ni_{36}$(001) surface. In the next two Sections, I will discuss *ab-initio* calculations that aim to explore the same surface from a theoretical point of view. In Section 3.2, I will deal with the problems concerning the geometry and atomic structure of the surface: relaxation, buckling, and nickel segregation on the surface. In Section 3.3, I will focus on the electronic structure and its relation to the tunneling spectra.

3.1 Experiment

This section is intended to present some basic information about the experimental work on which my theoretical analysis is going to be based, concentrating on the main results of the STM/STS experiments. Further details, especially those concerning the surface preparation and the experimental setup and conditions, may be found in our joint publication [34] with the Viennese experimentalists. The subject of the investigation was the (001) surface of a chemically disordered $Fe_{64}Ni_{36}$ alloy with a face-centered cubic (fcc) crystal lattice (the Invar alloy). The experiments were done at low temperatures, either at 80 K or at 5 K. Clean and atomically flat surfaces were prepared by Ar^+ sputtering and subsequent annealing. Atomically resolved STM images of the surface were obtained in the constant current regime. One such image is shown in Fig. 1(a). The tunneling voltage was set to -2 mV and

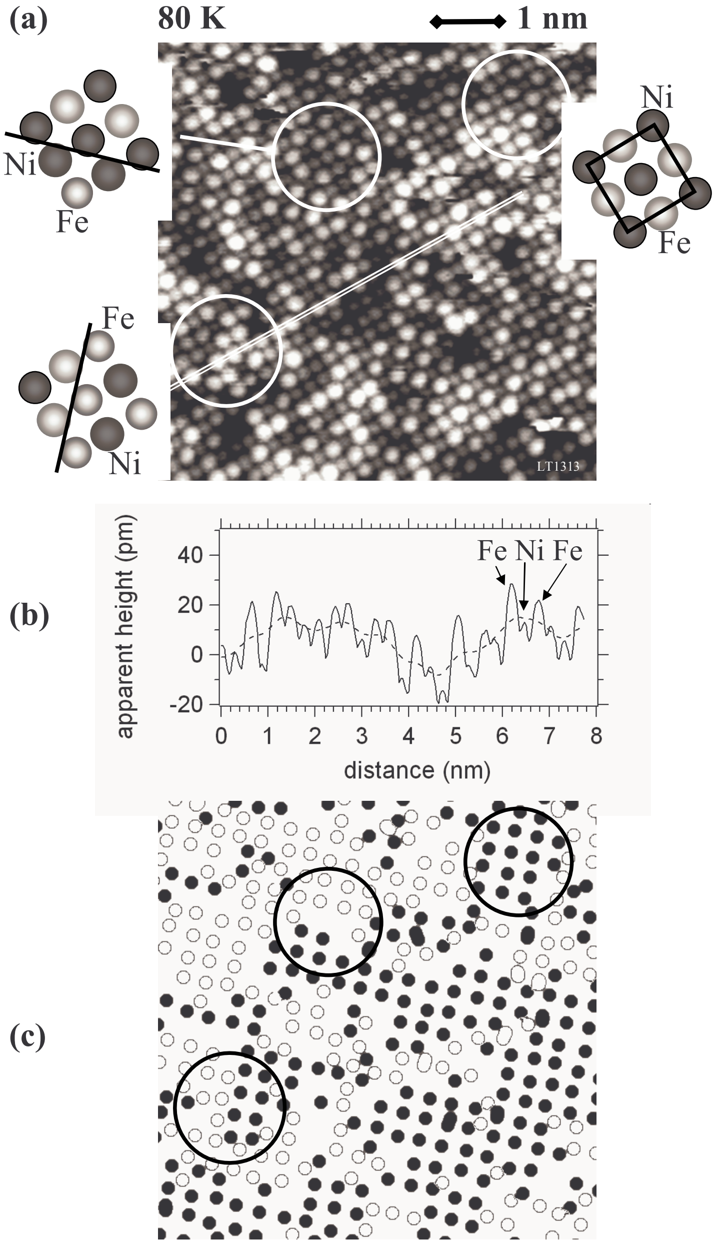

Figure 1: *(a) STM image of the* $Fe_{64}Ni_{36}$*(001) surface [34]. The three details highlight a* $c(2 \times 2)$*-ordered area (unit cell marked by a square) and both a short Ni-rich and a short Fe-rich anti-phase domain boundary. (b) Image profile along the white line marked in (a). The dashed average curve indicates a long-wavelength buckling on the nanometer scale in contrast to the short-wavelength buckling distinguishing Fe and Ni atoms. (c) Map of automatically detected Fe atom locations (corrugation maxima) in the STM image, omitting the Ni atoms, with each of the Fe atoms assigned to one of the two* $c(2 \times 2)$ *anti-phase sublattices (open and full circles).*

the tunneling current was maintained at 8 nA. The tunneling voltage is conventionally defined as the voltage bias of the sample with respect to the tip, so negative tunneling voltage means a negatively charged sample and a positively charged tip.

Apparent elevations of the surface are represented by lighter shades and apparent depressions by darker shades in the image. The round-shaped lighter spots on the darker background presumably mark the positions of surface atoms. The arrangement of the spots forms a roughly periodic square lattice, although disturbed by local defects like vacancies, in agreement with what can be expected for atoms on the (001) surface of a face-centered crystal. The spacing of the supposed atoms agrees with the value of lattice parameter of the Invar alloy and akin iron–nickel alloys, which is known from experiments to be $a \approx 0.36$ nm (see, e.g., [35] or [36]). The spots exhibit a noticeable dispersion of their apparent height, thus reflecting the partially disordered character of the alloy and its surface. We expect to observe two different types of spots, which could be identified with the iron and the nickel atoms, respectively. It is not obvious at first sight if the the spots that we see in the image can be sorted into two groups in a unique way. The expected chemical contrast is obscured by other sources of contrast, which probably stem from the composition variations in the sub-surface region. Nevertheless, after a high-pass filter was applied to the image so that the variations of apparent height on a nanometer and larger scale be quenched and only the most localized contributions to the contrast remain, the experimentalists were able to distinguish two separate peaks in the histogram of apparent heights. The two peaks in the histogram corresponded to two different types of atoms. The experimentalists then tried to change the composition of the surface by additional deposition of iron and found that the more protruding atoms (lighter spots) are those of Fe and the lower atoms (darker spots) are those of Ni. Most of the surface turns out to be covered by small domains of a $c(2 \times 2)-$FeNi structure, a checkerboard pattern formed by alternating Fe and Ni atoms. Neighboring domains are characterized by mutually interchanged Fe and Ni sublattices within the $c(2 \times 2)$ two-dimensional lattice. The prevailing type of the so-called anti-phase boundary between two such domains is the Fe-rich one, but Ni-rich boundaries are also present. Examples of the ordered structure and of both kinds of anti-phase domain boundaries are highlighted in Fig. 1(a). Based on the analysis of the STM images, the overall composition of the surface layer was estimated to $59\% \pm 2\%$ of atoms being iron and the complementary part (i.e. $41\% \pm 2\%$ of surface atoms) being nickel [34].

Tunneling spectra, i.e. the curves that describe the voltage dependence of the tunneling current, were measured for voltages spanning from -1 V to $+1$ V. The first derivative of the spectra was calculated numerically afterwards. The height of the tip above the surface during the spectroscopic measurement was set so that a tunneling current of 1 nA flowed at the voltage of -1 V. Therefore a constant current image at 1 nA and -1 V could be recorded simultaneously with the spectra. The constant current image is shown in Fig. 2(a). Current maps for a given voltage, such as the one displayed in Fig. 2(b), can be extracted from the spectroscopic data in a straightforward way. Unfortunately, the experimentalists were not able to obtain both an atomically resolved image and tunneling spectra for one and the same surface area. Examples of the spectra, presented as a voltage dependence of

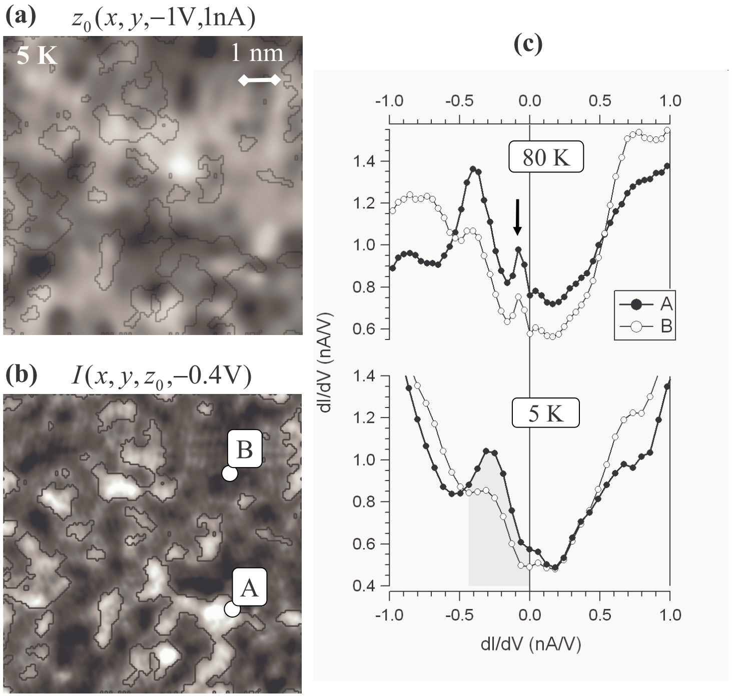

Figure 2: *(a) Constant current image of the $Fe_{64}Ni_{36}$(001) surface at the temperature of* 5 *K, tunneling current* 1 *nA, and sample voltage* -1 *V. (b) Corresponding current map at* -0.4 *V, showing the intensity of the spectroscopic feature discussed in the text (shaded area in the* 5 *K spectrum to the right). (c) Differential conductance spectra at* 5 *K corresponding to the images on the left and other differential conductance spectra obtained at* 80 *K on of a separately prepared sample. Shown are spectra from surface points where the prominence of the conductance peak reaches its extremum, maximum for A and minimum for B. The small peak at* -0.1 *V in the* 80 *K spectra (arrow) originates from a tip-related state. The contour lines in (a) and (b) encompass the fraction of the surface that displays spectra more similar to A than to B. The figure was taken from [34].*

the differential conductance, are given in Fig. 2(c). The most conspicuous feature of the spectra is a peak of the differential conductance at about -0.35 V. The curves shown in Fig. 2(c) are averages of spectra acquired in several tens of individual positions, chosen so that the peak in question would be either as much pronounced as possible or as small as possible. Obviously, the peak is present in virtually all spectra, no matter at which position on the surface the particular spectrum was obtained, but the size of the peak varies considerably among spectra from different parts of the surface.

3.2 Surface geometry

3.2.1 Methods and models

First, let me focus on the atomic structure of the surface, including the question of prevailing chemical composition of the surface and the surface corrugation at the atomic scale. All these subjects are closely related to the topography observed in the STM experiment. The equilibrium positions of the iron and nickel atoms in the surface and sub-surface layers were estimated via *ab initio* calculations for several models of the surface. The models were chosen to represent various parts of the surface that differ from each other by their local composition; the diversity of the models thus reflected the partially random arrangement of Fe and Ni atoms in the alloy and on its surface. Comparison of calculated total energies between the various models can help us to estimate the relative stability of different surface structures. The calculated total energies and especially the calculated atomic forces—the quantities which are needed when performing the relaxation of the surface structure into the energetically optimal equilibrium geometry—are sensitive to the faithful representation of the effective potential and electron density. So as to avoid imposing arbitrary restrictions on the shape of the effective potential and on the electron-density distribution, a full-potential linearized-plane-wave method (FP-LAPW) was applied to the solution of the problem. The program package WIEN2k [37], which implements the FP-LAPW method within the DFT framework, was used to carry out the calculations.

The FP-LAPW method implemented in WIEN2k allows one to deal with periodic structures only. The surface was thus replaced by a slab consisting of 9 atomic layers each. The slab was always symmetric with respect to the plane of the middle atomic layer. Periodically repeating slabs were separated from each other by empty spaces representing the vacuum above the surface. The empty spaces separating the slabs were roughly as thick as the slabs themselves (1.44 nm) to ensure that the slabs are properly isolated from each other. The surface unit cell defined by the periodicity in directions parallel to the surface plane always contained two atoms per atomic layer. The atoms were arranged in positions corresponding to the fcc lattice of the Invar alloy. The in-plane lattice parameter $a_{\|}$ that defined the size of the surface unit cell was set to $a_{\|} = 0.360$ nm. This value had been determined theoretically as the bulk lattice parameter of the ordered Fe_3Ni alloy; total energy minimization with respect to the lattice parameter had been performed for the Fe_3Ni structure using the GGA [38] exchange-correlation potential. The in-plane lattice parameter thus obtained was in reasonable accord with the experimental lattice parameter $a_{exp} = 0.358$ nm of the $Fe_{64}Ni_{36}$ alloy [35].

The seven models that have been explored are shown in Fig. 3. The models of the alloy structure are all based on the Fe_3Ni structure, while only the chemical composition and atomic arrangement in few topmost surface atomic layers vary from model to model. The ordered Fe_3Ni alloy was adopted as a suitable model substrate because its chemical composition and lattice parameter are similar to those of the Invar alloy, but unlike Invar, the Fe_3Ni has a periodic structure, as demanded by the numerical method in use. Fig. 3 also illustrates (taking model I as an example)

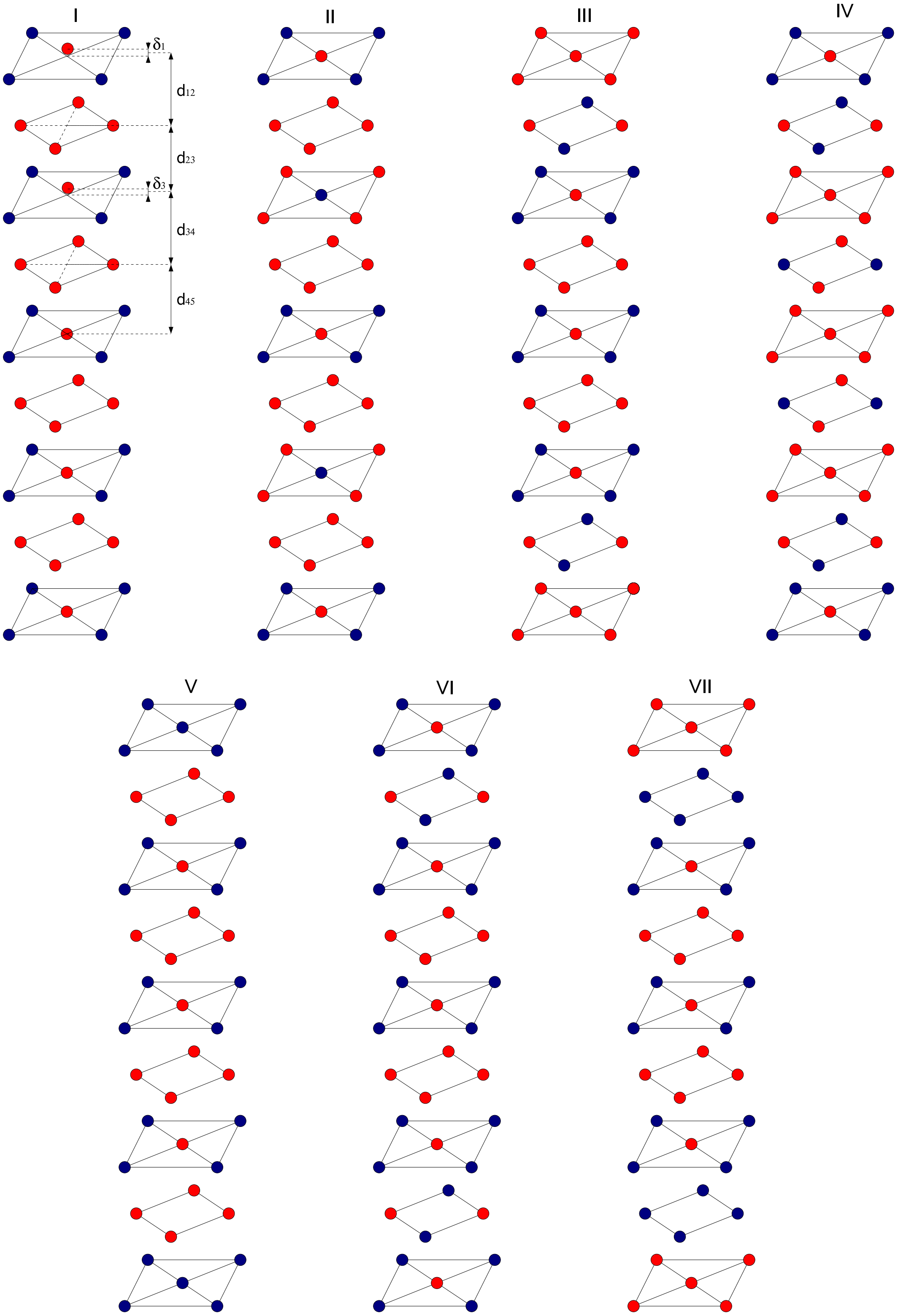

Figure 3: *Layer-by-layer structure of the seven models employed to represent the (001) surface of the FeNi alloy. The light red circles represent iron atoms, the dark blue circles represent nickel atoms. The notation used to describe the geometry of the surface is shown for model I.*

the notation that is going to be used in describing the calculated geometry of the surface structure. In brief, the inter-layer distance between the layers number i and j (counted from the surface) is denoted as d_{ij} while the 'buckling' of the i-th atomic layer, i.e. the height difference between the two inequivalent atomic positions in that layer, is denoted as δ_i. If an atomic layer is buckled, some care has to be taken to define the position of the layer for the purpose of measuring d_{ij} unambiguously. Here, the position of an atomic layer is to be defined as the arithmetic means of the vertical positions of both inequivalent atoms in the layer.

The surface Brillouin zone was sampled by a mesh consisting of 20 × 20 Bloch wave vectors ($\vec{k}$-points). The exchange-correlation potential was approximated according to the Perdew, Burke, and Ernzerhof [38] GGA prescription. However, using the LDA (namely that of Vosko, Wilk, and Nusair) for the exchange-correlation potential would not substantially change the findings which are going to be presented here [34]. The number of the augmented plane waves in the basis set is given by the upper cutoff $K_{max} = 68.7\ \mathrm{nm}^{-1} = 3.64\ \mathrm{a.u.}^{-1}$ (1 a.u. being equal to the Bohr radius) for the wave vectors. This maximal wave vector corresponds to the maximal kinetic energy of 13.2 Ry. The plane wave expansion of the effective potential and charge density outside the atomic spheres (in the interstitial and in the vacuum region, which are treated on the same footing by WIEN2k) was limited by the upper bound $G_{max} = 265\ \mathrm{nm}^{-1} = 14\ \mathrm{a.u.}^{-1}$. The calculations were carried out as spin-polarized; the ferromagnetic order was assumed.[3] The basis functions and the effective potential inside the atomic spheres were expanded into spherical harmonics up to the angular quantum number $l_{max} = 10$, but only spherical harmonics for $l \leq 4$ in the expansion of the wave functions were employed to calculate the (comparatively small) non-spherical parts of the effective potential. The radii of the atomic spheres were set to 2.2 a.u., which equals 0.116 nm. With this atomic sphere radii, the space left between the most closly neighboring atomic spheres in the bulk $\mathrm{Fe_3Ni}$ amounted to 8.5 % of the distance between the centers of these spheres. The $1s$, $2s$, $2p$, and $3s$ electron states were treated as the atomic core, which means that no energy dispersion over the Brillouin zone (no band structure) was considered for them. Further, the $3p$ and $4s$ states were treated as semi-core levels: The $\vec{k}$-dependent energy dispersion was taken into account for the energy levels of these semi-core states just as for the valence states and special local orbitals were added to the set of basis functions so that the basis set was capable of representing the semi-core states adequately. Finally, the remaining electron states corresponding to higher-lying energy levels were the valence electron states, which were represented by the LAPW/APW+lo basis set along with the semi-core states but without any

---

[3] The possibility that a local antiferromagnetic order or disordered local magnetic moments may occur on the alloy surface was checked for several models of the surface. So as to speed up the calculations, the TB-LMTO method was used for this purpose instead of the FP-LAPW method, because these calculations did not require so much precision as compared to, e.g., the calculations of the surface buckling. It turned out that flipping the local (atomic) magnetic moments from the ferromagnetic into the $c(2 \times 2)$ antiferromagnetic order or introducing the disorder into the local moments (the disorder could be adequately treated within the TB-LMTO by means of the CPA but not in the FP-LAPW calculations) increased the total energy of the system; the order of magnitude of this energy cost was found to be 0.1 eV per surface unit cell. The assumption of the ferromagnetic order is thus justified.

additional local orbitals needed. The APW+lo scheme was used to define the augmentation part of basis wave functions inside the atomic spheres for $l \leq 2$ while the LAPW scheme was used for the same purpose for $l > 2$. All these parameters that describe the construction of the basis set inside the atomic spheres applied equally to both Fe and Ni atoms.

The method of damped Newtonian dynamics was employed to perform the relaxation of the structures representing the alloy surface and thus to arrive at zero-temperature equilibrium atomic positions. The in-plane lattice parameter $a_{\parallel}$ was fixed to the above quoted value 0.360 nm. The positions of the three central atomic layers in the slab (i.e. the 4th, 5th, and 6th atomic layer) were also kept fixed. The distance between the forth and fifth atomic layer (and by symmetry also that between the fifth and the sixth) was set to $d_0 = a_{\parallel}/2 = 0.180$ nm. The structures were considered to be fully relaxed if the force that acted upon any of the atoms within the particular structure except the fixed ones was smaller than 0.1 eV/nm. For the details of the method of calculating the atomic forces see [23].

In the preceding calculation of the bulk Fe_3Ni structure that was aimed at determining $a_{\parallel}$, the three-dimensional Brillouin zone was sampled by a mesh containing $20 \times 20 \times 20$ $\vec{k}$-points. Other parameters of the calculation concerning the bulk Fe_3Ni, like the plane wave cutoff K_{max} for the plane wave basis set or the cutoff G_{max} for the plane wave expansion of the effective potential and charge density, were the same as the corresponding parameters of the slab calculations.

3.2.2 Results and discussion

The models of the alloy structure presented in Fig. 3 are summarized again in Tab. 1. In addition, the dependence of the calculated total energy on atomic arrangement is shown for the respective relaxed structures in the table. When models with the same overall stoichiometry are compared in terms of total energy, the models that involve the $c(2 \times 2)-$FeNi structure in the top surface layer come out as the most favorable. Interchanging a Ni atom on the surface with a sub-surface Fe atom to form a purely Fe surface layer (I→III, II→III, or VI→VII) invariably increases the total energy. Interchanging a surface Fe atom with a sub-surface Ni atom to form a purely Ni surface layer from the $c(2 \times 2)-$FeNi surface (VI→V) increases the total energy too, even though by a smaller energy than in the previously mentioned cases of pure-iron surface formation. This is in accord with the experimental observation that locally ordered $c(2 \times 2)-$FeNi areas are the prevailing structure on the (001) surface of the $Fe_{64}Ni_{36}$ alloy.

Tab. 2 contains a detailed description of the calculated relaxed geometry of all the model structures. The deviations of the interlayer distances from the ideal unrelaxed fcc structure are given in terms of a percentage of the ideal interlayer distance $d_0 = a_{\parallel}/2 = 0.180$ nm. In the same way—as a percentage of d_0—the buckling of the first three surface layers is tabulated. The largest surface buckling, which amounts to 0.0135 nm in terms of an absolute height difference, has been found for model II. Note that if the top surface layer contains both Fe and Ni atoms, the Fe atoms always stick out of the surface and the Ni atoms sink down towards the

model #	composition	E_{tot} [meV]
I	FeNi/FeFe/FeNi/FeFe/FeNi/...	0
II	FeNi/FeFe/NiFe/FeFe/FeNi/...	+13
III	FeFe/FeNi/FeNi/FeFe/FeNi/...	+39
IV	FeNi/FeNi/FeFe/NiFe/FeFe/...	—
V	NiNi/FeFe/FeNi/FeFe/FeNi/...	+27
VI	FeNi/FeNi/FeNi/FeFe/FeNi/...	0
VII	FeFe/NiNi/FeNi/FeFe/FeNi/...	+127

Table 1: *Chemical composition of first five atomic layers from the surface is indicated for each model. The composition of the rest of the layers (from the sixth to the ninth) is determined by symmetry. The order of atoms in a particular layer (FeNi vs. NiFe) generally matters. For example, models I and II differ only by whether an Fe atom in the third layer is positioned directly below another Fe atom in the first layer (this is so in model I) or whether it is below an Ni atoms in the first layer (model II). Furthermore, a comparison of calculated total energies per surface atom is made. The shown numerical values of the total energy are differences of the total energy of the particular system from the total energy of a reference system with the same composition stoichiometry. The systems I (for the slab composition of* $\mathrm{Fe}_{13}\mathrm{Ni}_5$*) and VI (for* $\mathrm{Fe}_{11}\mathrm{Ni}_7$*) were chosen as the reference.*

model #	δ_1/d_0	$\Delta d_{12}/d_0$	δ_2/d_0	$\Delta d_{23}/d_0$	δ_3/d_0	$\Delta d_{34}/d_0$
I	**+3.3** %	−1.0 %	0	+1.4 %	−1.0 %	+1.2 %
II	**+7.5** %	0.0 %	0	+2.6 %	−0.1 %	+1.9 %
III	−4.1 %	+1.4 %	+0.3 %	−2.3 %	−0.4 %	+2.3 %
IV	**+2.8** %	−4.5 %	+0.9 %	+2.6 %	+1.5 %	+1.5 %
V	0.0 %	−6.0 %	0	+2.8 %	−0.9 %	+1.5 %
VI	**+2.6** %	−3.9 %	+0.5 %	−1.4 %	+0.2 %	+2.5 %
VII	+2.2 %	−2.1 %	0	−2.6 %	+0.3 %	+2.7 %

Table 2: *Atomic layer buckling (*δ_1 *to* δ_3*) and the changes of the inter-layer distances (*Δd_{12} *to* Δd_{34}*) with respect to the calculated* $\mathrm{Fe}_3\mathrm{Ni}(001)$ *interlayer distance,* d_0*=0.180 nm, are listed here for the various models of the FeNi(001) surface in the form of the corresponding percentage of* d_0*. If the tabulated buckling reads "0", the buckling is exactly zero due to the symmetry of the respective model, while "0.0 %" means that the buckling was calculated to be zero within the precision indicated. The sign of the buckling is chosen so that the buckling of a given atomic layer is positive if the atom that goes first in the formula for that layer in Tab. 1 is shifted upwards (towards the surface) and the atom that goes second in the formula is shifted downwards (towards the substrate).*

bulk, which is indicated by a positive sign of δ_1 in the first column of Tab. 2 (see the entries printed in bold). However, the amount of buckling that takes place in the top surface layer depends substantially on the chemical composition of the subsurface layers, as demonstrated by the differences found between the models I, II, IV, and VI. Comparison of model I with model II reveals that even the structure of the third atomic layer has an important influence on the buckling in the topmost atomic layer. Furthermore, the surface areas in which one element (Fe or Ni) locally prevails may exhibit a notable buckling on the atomic scale too, as demonstrated by models III and VII. The interlayer distances also differ from model to model by several per cent of d_0, so the positions of atomic layers are different as well. The fact that the position of the top atomic layer differs between various models of the alloy structure suggests that the surface buckling also occurs on a larger scale than just between the nearest atomic neighbors, because the vertical atomic positions on the real disordered surface must then differ among places that locally correspond to different ordered models. The chemically insensitive contributions to the buckling interfere with the chemical contrast between Fe and Ni and blur this contrast. All these findings agree well with the topography of the STM images, in which the Fe atoms appear as more protruding from the surface than the Ni atoms while the apparent height of atoms belonging to the same element varies considerably too, making it difficult but still possible to distinguish the Fe atoms from the Ni atoms. The height variances observed by the STM are thus not only apparent but they generally correspond to real vertical differences in atomic positions on the surface. Finally, I shall note that part of the results presented here has been also published in [39]; however, the notation for the models does not completely agree, model III of the paper [39] is model IV here.

Surprisingly, while the observed contrast between the Fe and Ni atoms on the Invar (001) surface agrees with what could be expected from the calculated surface buckling, it is at variance with the picture based on the Tersoff-Hamann theory of STM imaging. So as to obtain the theoretical prediction in the spirit of Tersoff and Hamann, one should compare the local density of states (LDOS) at the Fermi level in vacuum above the surface iron atoms with the corresponding LDOS above the surface nickel atoms. The comparison should be made between points in the same height above the surface, i.e., one compares points that are located on one and the same plane parallel to the surface. It will be argued in the next section that any feasible slab thickness is insufficient for a faithful modeling of the vacuum density of electron states related to the STM images and spectra. However, calculations performed on four different slabs consisting of 25 atomic layers indicate that the LDOS at the Fermi level is higher above the Ni atoms than above the Fe atoms. The LDOS was evaluated 0.3 nm above the top surface atomic layer. The structure of the 25-layer slabs was derived from models I, II, IV, and VI. These are the model structures that contain both Fe and Ni atoms in the topmost surface layer. The positions of atoms in the four outermost atomic layers on both sides of the slab were taken from the previously performed surface relaxation of the respective models. The remaining central part of the 25-layer slabs was an ideal Fe_3Ni structure that consisted of alternating Fe and $c(2 \times 2)-$FeNi layers. The contrast found for the vacuum Fermi-level LDOS thus seems to be the inverse of the STM contrast that was seen in the experiment. A calculation for an ideally smooth surface, which was represented by a 25-layer slab based on the model I without the surface buckling and relaxation, showed that the inverse contrast in the Fermi-level LDOS existed above the smooth surface too and that the Fermi-level LDOS above the Ni atoms was even more enhanced there. The surface buckling that involves shifting the Fe atoms upwards from the surface acts against this kind of contrast, enhancing the LDOS above Fe atoms, although it does not suffice to change the contrast so that it would correspond to the STM images. The simple Tersoff–Hamann theory thus fails to explain the appearance of the STM images as they have been found in the experiment. The experimental contrast is obviously related to the chemically sensitive surface buckling but does not directly correspond to the DFT-calculated equilibrium electronic structure of the alloy surface. The effect of the surface buckling must be enhanced by some effects which were not taken into account in my calculations and which are most probably related to the interaction between the surface and the tip of the microscope.

3.3 Electronic spectra

3.3.1 Methods and models

According to the Tersoff-Hamann model, the peak of the differential tunneling conductance observed on the alloy surface at the voltage of ≈ -0.3 V should correspond to a peak that is reached by the local density of states above the surface at ≈ 0.3 eV below the Fermi level. A peak in the LDOS in vacuum above a surface usually originates from surface states or resonances, i.e. from electron states localized in the surface atomic layer or in several atomic layers near the surface. Thus the feature found in the tunneling spectra at -0.35 V indicates the presence of such a surface state or resonance. Although the Tersoff-Hamann model is an oversimplified description of the actual STM/STS experiment, because the electronic structure of the probing tip and the interaction between the tip and the surface can significantly influence the tunneling spectra, a distinct peak of the local density of electron states in vacuum above the surface may still play a decisive role in the formation of the tunneling spectra. A direct correspondence between a surface state/resonance and a peak in tunneling conductance has been previously reported, e.g., for the Fe(001) and Cr(001) surfaces [40]. It is therefore worthwhile to analyse the structure of electron states near the surface of the alloy in the vicinity of the Fermi level and especially the local density of states in vacuum above the surface to see how it relates to the observed tunneling spectra.

Unfortunately, the calculations in the slab geometry described in the previous section, which were performed to find the equilibrium atomic positions on the surface, are not suitable for the purpose of analysing the spectroscopy. The slab effectively behaves as a potential well in the direction perpendicular to the surface and the electron states in the slab thus become quantized. The effect of such a quantization is demonstrated in Fig. 4. The $\vec{k}_{\|}$-resolved local density of states (or Bloch spectral function, BSF) localized at $\vec{k}_{\|} = \bar{\Gamma} \equiv 0$ in the reciprocal space and in vacuum 0.18 nm above the surface in real space is depicted in this figure for three different models, all of which represent a pure Fe surface layer on a homogeneous $Fe_{64}Ni_{36}$ substrate. First, it is a genuinely semi-infinite $Fe/Fe_{64}Ni_{36}$ system with only one surface facing the vacuum on one side and attached to an infinite bulk of the $Fe_{64}Ni_{36}$ on the other side; second, a 30-layer slab (two pure Fe atomic layers on both surfaces, 28 atomic layers of $Fe_{64}Ni_{36}$ in between, and vacuum bordering the slab on both sides); and, third, a 10-layer slab (two Fe layers, eight $Fe_{64}Ni_{36}$ layers, and again vacuum on both sides). The oscillation of the spectral function due to the confining boundaries—even in the slab that was 30 atomic layers thick—is clearly visible. A potential surface resonance that may appear in the semi-infinite case becomes lost amidst this oscillation if the calculation is performed in a slab geometry. Having slabs much thicker than 30 atomic layers in the FP-LAPW calculations is not tractable because of the demands on both time and computer memory. While one would expect the LDOS, which can be expressed as the integral of the site-projected

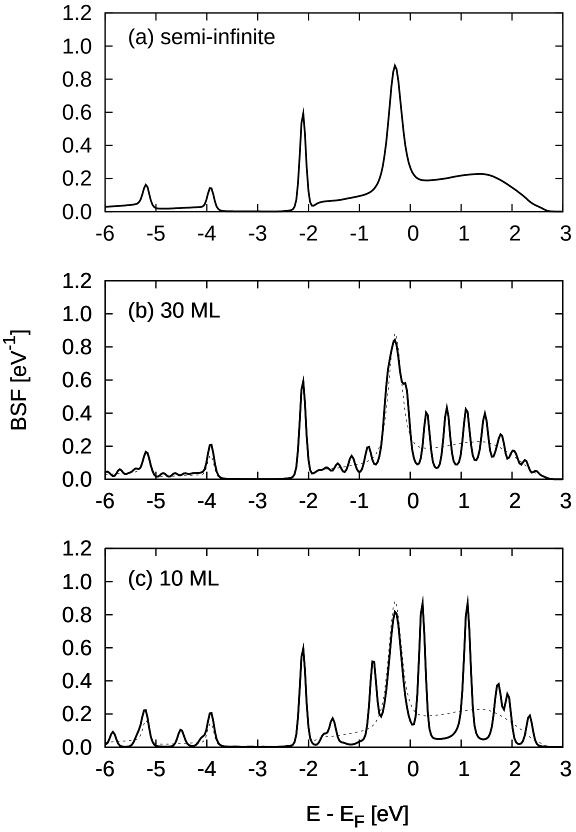

Figure 4: *Bloch spectral function at* $\vec{k}_{\parallel} = (0, 0)$*, i.e. at the central point* $\bar{\Gamma}$ *of the surface Brillouin zone, projected onto a sphere in vacuum 0.18 nm above the* $Fe/Fe_{0.64}Ni_{0.36}$ *surface. The surface was represented (a) by a truly semi-infinite system, (b) by a slab that consisted of 30 atomic layers of the material, and (c) by a slab that consisted of 10 atomic layers of the material. The projected Bloch spectral density above the semi-infinite system from the top panel is also indicated by a dotted line in the other two panels for easier comparison.*

Bloch spectral functions over the whole surface Brillouin zone, to be considerably smoother inside the material than a single BSF (like the one for $\vec{k}_{\|} = \bar{\Gamma}$) because the oscillations of BSF from different parts of the surface Brillouin zone may partially compensate, the situation is different in vacuum above the surface. Typically, only wave functions from a small part of the Brillouin zone penetrate into the vacuum significantly. Consequently, the oscillation of the $\vec{k}_{\|}$-resolved spectral function from the most contributing $\vec{k}_{\|}$ point prevails and it shows in the resulting local density of states in the vacuum.

The Bloch spectral functions in Fig. 4 were calculated by the linear muffin-tin orbital method in the atomic sphere approximation (LMTO-ASA) using the coherent potential approximation (CPA) to represent the homogeneous alloy. The main advantage of the LMTO-ASA method is its ability to treat the surface as a semi-infinite system within the formalism of surface Green's functions, together with its ability to deal with the substitutional disorder in the alloy by means of the CPA. In the LMTO-ASA method, the whole space occupied by the model systems is divided into atomic spheres, including the vacuum, which formally consists of atomic spheres with zero atomic number. Therefore expressing the BSF projected onto an atomic sphere was a natural way to obtain a real-space local characteristics of the electronic structure. The site-projected BSFs shown in Fig. 4 were evaluated in an atomic sphere of the first vacuum layer adjacent to the topmost surface atomic layer; the above mentioned distance of 0.18 nm is the distance between the planes going, respectively, through the center of the first vacuum layer and through the center of the top surface atomic layer.

Spin-polarized scalar-relativistic calculations using the LDA of Vosko, Wilk, and Nusair [41] for the exchange-correlation potential were performed to obtain Fig. 4 and also in all the further discussed cases in which the LMTO-ASA method was employed to analyze the electronic structure of the Invar surface. The surface Brillouin zone was sampled by 15×15 $\vec{k}$-points. The number of $\vec{k}$-points that was needed for the LMTO-ASA calculation was smaller as compared to the FP-LAPW calculation described in the previous section. The reason is that no calculation of atomic forces was undertaken with the LMTO-ASA method. The *spd* basis was used, i.e., the basis contained orbital wave functions with angular quantum numbers $l \leq 2$ (as both Fe and Ni are $3d$ metals). An optimized screening transformation was applied on the structure constants and the Green's functions [24]. Owing to the screening transformation, the structure constants that coupled atomic layers more distant than the next-nearest neighbors were negligible and *principal layers* consisting of only two atomic layers each therefore could be used to evaluate the surface Green's functions. No surface buckling or surface layer relaxation was considered in the LMTO-ASA calculations; the atomic spheres were placed on an ideal fcc lattice. The previous FP-LAPW calculations indicated that the density of states is not substantially affected by small changes of the surface geometry.[4] The atomic sphere radius of

---

[4] Of course, the FP-LAPW results for the vacuum LDOS are spoiled by the above discussed quantization effects, but it still makes sense to compare the LDOS that was calculated for the relaxed geometry with that calculated for the ideal geometry to see how the relaxation changes the LDOS.

$r = 0.140$ nm was used for the purpose of the ASA. This radius corresponds to the experimental lattice parameter of the fcc Invar lattice $a_{exp} = 0.358$ nm.

Apart from the above discussed cases in panels (b) and (c) of Fig. 4, which were only intended to illustrate the importance of proper boundary conditions, all other models of the surface that were handled with the LMTO-ASA method had the form of a semi-infinite system bordered by a vacuum region on one side only. These models consisted of 10 layers of the atomic spheres for which the electron density and effective potential were determined in a self-consistent way. Three of the layers represented the vacuum above the surface and the other seven represented the atomic layers of the alloy near the surface including the topmost surface layer. The boundary conditions for such a slab of 10 atomic layers were defined by attaching it to a semi-infinite vacuum region on the side of the 3 vacuum layers and to a semi-infinite region of a homogeneous $\mathrm{Fe}_{64}\mathrm{Ni}_{36}$ alloy on the other side. The semi-infinite vacuum region was characterized by a flat effective potential. The work function that set the level of the vacuum potential was calculated self-consistently along with the effective potential in the atomic spheres of the 10-layer slab, thus taking into account the surface dipole barrier. The effective potential for the atomic spheres in an infinite $\mathrm{Fe}_{64}\mathrm{Ni}_{36}$ bulk had been calculated in advance and was used to define the surface Green's function of the semi-infinite $\mathrm{Fe}_{64}\mathrm{Ni}_{36}$ region.

The local densities of states and Bloch spectral functions (BSF; see section 2.10 for definition) were explored for several models of the surface. All the models were based on the $\mathrm{Fe}_{64}\mathrm{Ni}_{36}$ homogeneous alloy. Only the composition of the top atomic layer or the two topmost atomic layers on the surface varied among the models. The differences in the model surface composition were introduced so as to mimic local deviations from the average surface composition; this deviations arise on the real alloy surface due to the partially random arrangement of atoms. Furthermore, even the average composition of the alloy near the surface differs from the bulk composition, e.g. due to preferential segregation of one element on the surface or due to the formation of surface structures like the partially ordered $c(2 \times 2)-$FeNi structure that has been discussed in the previous section. In the following, I will use the notation $\mathrm{Fe}_x\mathrm{Ni}_{1-x}/\mathrm{Fe}_{0.64}\mathrm{Ni}_{0.36}$ and $\mathrm{Fe}_x\mathrm{Ni}_{1-x}/\mathrm{Fe}_y\mathrm{Ni}_{1-y}/\mathrm{Fe}_{0.64}\mathrm{Ni}_{0.36}$ to describe the composition of the model structures. The subscripts denote the relative content of the respective element in the respective atomic layer and, at the same time, they can also be interpreted as the probability that a given atomic site in the respective layer be occupied by the particular element. Unless indicated otherwise, all sites in one atomic layer are considered equivalent, in the sense that the probability of being occupied by an atom of a particular element (Fe or Ni) is the same for all sites in the layer. Such models can be treated as periodic structures within the CPA; more precisely, they are characterized by configurationally averaged Green's functions which are periodic in the two dimensions parallel to the surface. The surface unit cell of these structures contains one atom per atomic layer.

3.3.2 Results and discussion

Figures 5–8 show (in the panels on the left-hand side) the local density of electronic states around the Fermi level as found above the model surfaces of various composi-

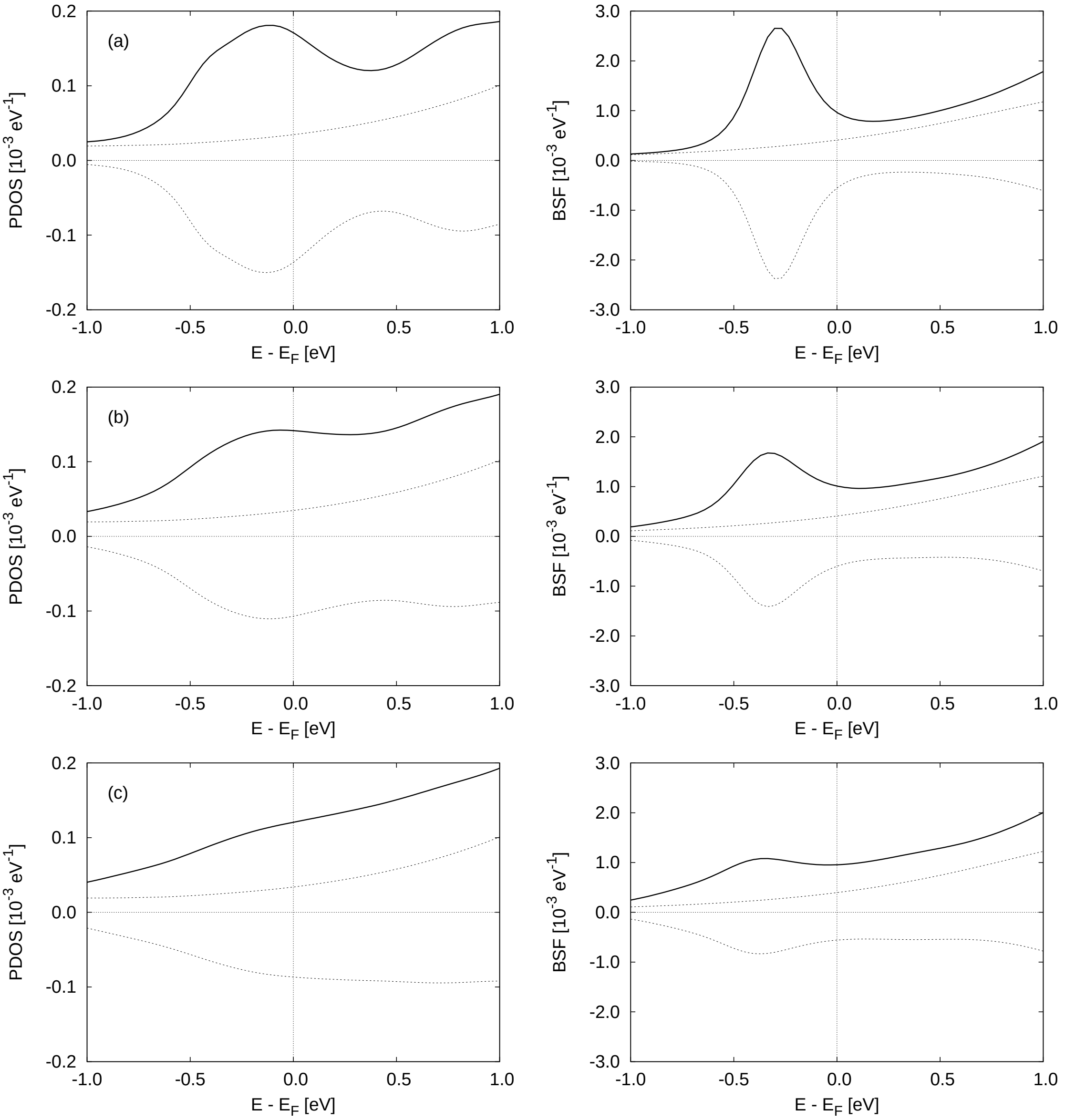

Figure 5: *Densities of states projected onto a sphere 0.54 nm above the alloy surface (panels to the left) and Bloch spectral functions at the center of the surface Brillouin zone* ($\vec{k}_{\parallel} = \bar{\Gamma}$) *in the same location above the surface (panels to the right) for the following models of the surface: (a)* $\mathrm{Fe/Fe_{0.64}Ni_{0.36}}$*, (b)* $\mathrm{Fe_{0.875}Ni_{0.125}/Fe_{0.64}Ni_{0.36}}$*, and (c)* $\mathrm{Fe_{0.75}Ni_{0.25}/Fe_{0.64}Ni_{0.36}}$*. Full lines represent the total (all-spin) densities and spectral functions whereas dotted lines represent the corresponding spin-resolved components; the minority-spin components are flipped over the horizontal axes into the negative half-plane.*

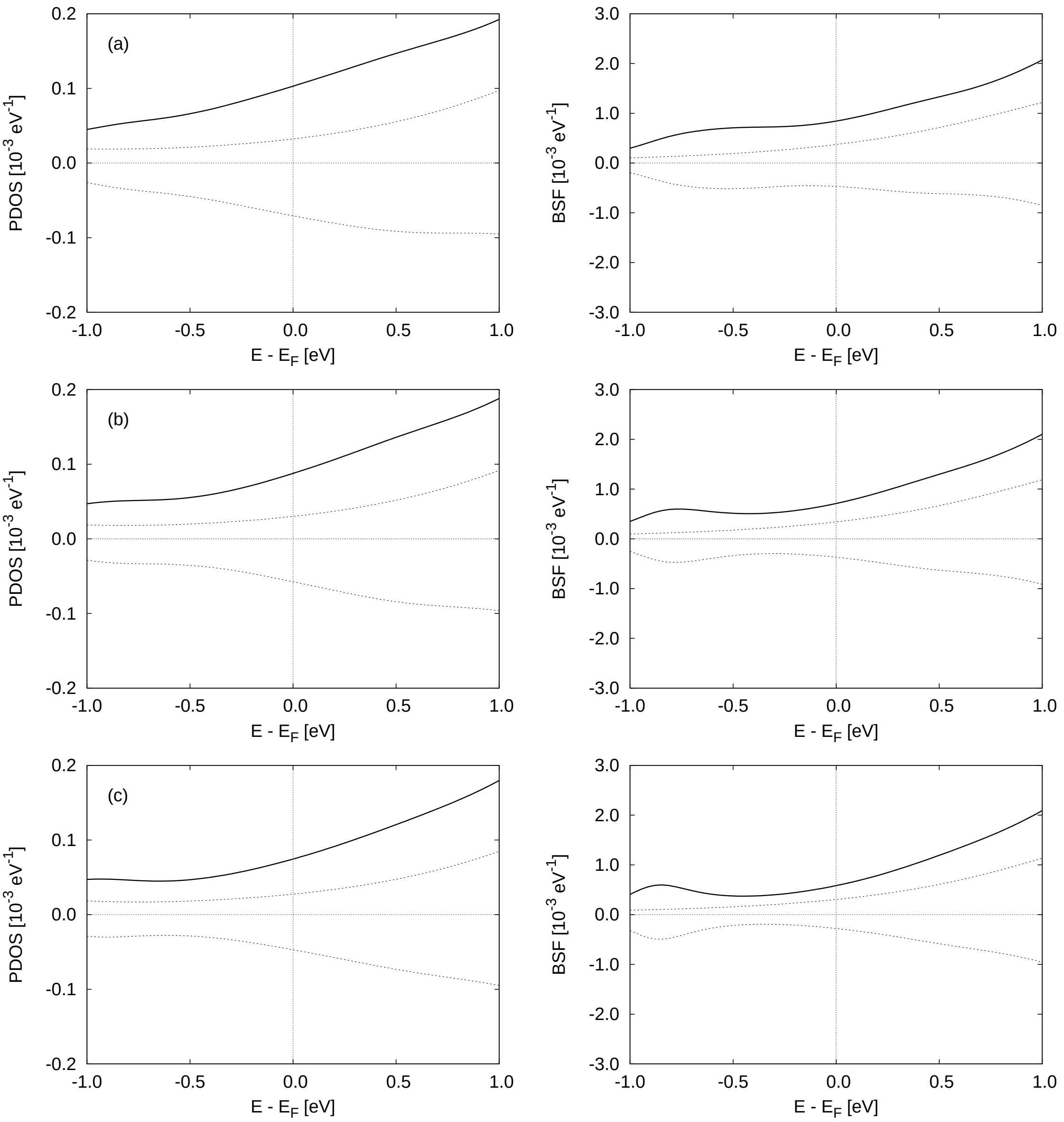

Figure 6: *Projected densities of states (left) and the Bloch spectral functions at* $\vec{k}_{\|} = \bar{\Gamma}$ *(right) in vacuum 0.54 nm above the alloy surface (just as in Fig. 5) for the following models of the surface: (a)* $\mathrm{Fe}_{0.625}\mathrm{Ni}_{0.375}/\mathrm{Fe}_{0.64}\mathrm{Ni}_{0.36}$*, (b)* $\mathrm{Fe}_{0.5}\mathrm{Ni}_{0.5}/\mathrm{Fe}_{0.64}\mathrm{Ni}_{0.36}$*, and (c)* $\mathrm{Fe}_{0.375}\mathrm{Ni}_{0.625}/\mathrm{Fe}_{0.64}\mathrm{Ni}_{0.36}$.

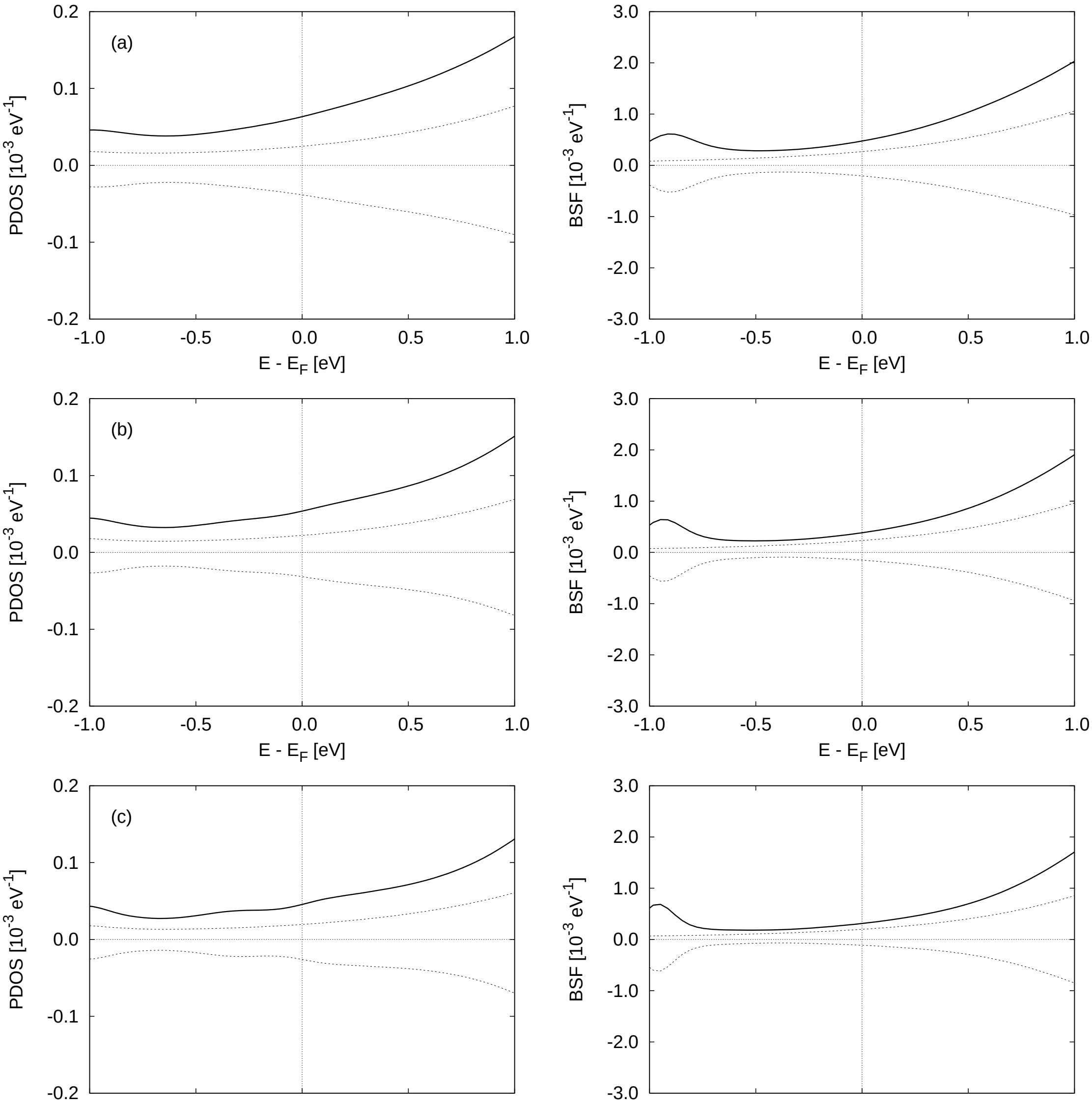

Figure 7: *Projected densities of states (left) and the Bloch spectral functions at* $\vec{k}_\parallel = \bar{\Gamma}$ *(right) in vacuum 0.54 nm above the alloy surface (just as in Figs. 5 and 6) for the following models of the surface: (a)* $\mathrm{Fe}_{0.25}\mathrm{Ni}_{0.75}/\mathrm{Fe}_{0.64}\mathrm{Ni}_{0.36}$*, (b)* $\mathrm{Fe}_{0.125}\mathrm{Ni}_{0.875}/\mathrm{Fe}_{0.64}\mathrm{Ni}_{0.36}$*, and (c)* $\mathrm{Ni}/\mathrm{Fe}_{0.64}\mathrm{Ni}_{0.36}$.

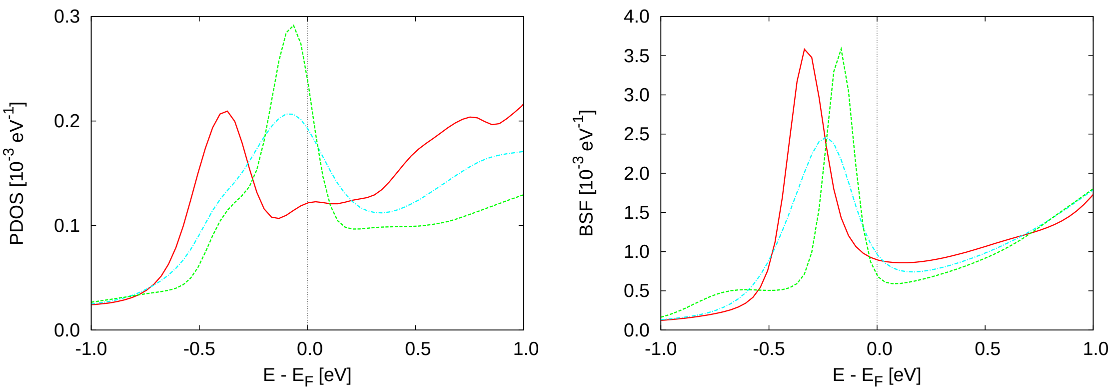

Figure 8: *Total (all-spin) projected densities of states (panels to the left) and the Bloch spectral functions at* $\vec{k}_{\|} = \bar{\Gamma}$ *(panels to the right) in vacuum 0.54 nm above a surface covered with a pure iron layer are shown here for the following models of the surface:* $\mathrm{Fe/Fe/Fe_{0.64}Ni_{0.36}}$ *(full red line),* $\mathrm{Fe/Fe_{0.5}Ni_{0.5}/Fe_{0.64}Ni_{0.36}}$ *(dash-dotted light blue line), and* $\mathrm{Fe/Ni/Fe_{0.64}Ni_{0.36}}$ *(dashed green line).*

tion. More precisely, the plotted quantity (PDOS) is the density of states projected onto a sphere in the third layer (counted from the surface) of empty atomic spheres representing the vacuum; this third vacuum layer is centered 0.54 nm above the surface of the alloy. The projected density of states equals the integral of the LDOS over the respective atomic sphere and thus is—up to a factor equal to the volume of the atomic spheres—a good representation of the LDOS at a point near the center of the sphere. The projected densities of states were decomposed into the majority-spin and the minority-spin components; this spin-resolved components are presented in each panel of Figs. 5–7 along with their sum that gives the total PDOS.

The right-hand side panels of Figs. 5–8 show the BSF projected onto the third vacuum layer for $\vec{k}_{\|} = \bar{\Gamma} \equiv 0$ and for the same composition of the surface layers for which the projected density of states is shown in the corresponding panels to the left. Again, the majority-spin and the minority-spin components of the Bloch spectral functions are shown along with the total (all-spin) BSFs in Figs. 5–7. As it will be discussed below, the principal contribution to the feature that we expect to find in the vacuum LDOS 0.35 eV below the Fermi level comes from the center of the surface Brillouin zone and its close neighborhood. Indeed, a peak at about −0.3 eV is visible in the minority-spin PDOS above iron-rich surfaces (Fig. 5) and this peak is even sharper in the corresponding Bloch spectral functions at $\vec{k}_{\|} = 0$. The peak, however, disappears as the content of Fe in the top surface layer becomes smaller than 75 %. Instead, another peak of the BSF at $\vec{k}_{\|} = \bar{\Gamma}$ develops at about 0.9 eV below the Fermi level for Ni content above 25 % in the topmost atomic layer and this peak also becomes apparent in the vacuum-projected densities of states as the nickel content in the top layer approaches 100 %. The PDOS and the BSF at $\vec{k}_{\|} = \bar{\Gamma}$ of the majority spin channel are rather featureless in the energy region for which the densities of states and spectral functions are plotted. The shapes of the total projected DOS and the corresponding BSF (at $\vec{k}_{\|} = \bar{\Gamma}$) are thus primarily controlled by the minority-spin component.

Fig. 8 illustrates the effect that the sub-surface composition can have on the PDOS and BSF above the surface. The models presented in this figure all involve a pure iron layer that covers the alloy surfaces. The vacuum electronic-structure feature ≈ 0.3 eV below the Fermi level is especially distinct above such surfaces. The composition of the sub-surface layer varies from pure iron to pure nickel in these models. We see that the peak in both the PDOS and the BSF (at $\vec{k}_{\|} = \bar{\Gamma}$) appears for any sub-surface composition, only the width of the peak varies and its position on the energy scale slightly shifts as the sub-surface composition changes. The influence of deeper atomic layers is expected to be even smaller.

The three panels on the left-hand side of Fig. 9 demonstrate that the peak in the minority-spin Bloch spectral function at $\vec{k}_{\|} = \bar{\Gamma}$ and 0.3 eV bellow the Fermi level is indeed a feature localized on the surface and penetrating into the empty space above it. Nevertheless, we can also see that the BSF for $\vec{k}_{\|} = \bar{\Gamma} \equiv 0$ at the energy of the surface peak does not fall completely to zero even deep in the bulk material. There are evidently some bulk states at the same energy for $\vec{k} = (0, 0, k_z)$ (which are the $\vec{k}$-points that project onto $\vec{k}_{\|} = 0$), so strictly speaking the peak corresponds to a *surface resonance* rather than a genuine surface state, since there is a possible hybridization among the surface resonance and the bulk states.

Due to the tetragonal symmetry of the underlying crystal lattice, the spectral functions at $\bar{\Gamma}$ can be decomposed into parts that correspond to different irreducible representations of the C_{4v} symmetry group. Fig. 9 shows that the surface resonance originates from orbitals that are invariant under any $n\pi/2$ rotation around the four-fold axes perpendicular to the surface (as well as under a reflection with respect to one of the four vertical mirror planes). Such orbitals and the wave functions composed of them transform according to the trivial representation of the symmetry group that is conventionally denoted as A_1 [42] (or Δ_1, as in, e.g., [43]). Namely, the orbitals that exhibit this symmetry are s, p_z, and $d_{z^2-r^2/3}$ (for the last, a shortened notation d_{z^2} can be used); this notation assumes that the z-axis is oriented perpendicular to the surface and thus along the four-fold rotation axis. The symmetric wave functions at $\vec{k}_{\|} = \bar{\Gamma}$ that belong to the A_1 representation penetrate into the vacuum more easily than any wave functions that correspond to the same energy but to a different representation of the symmetry group. To see why it should be so, consider an expansion of the wave functions into plane waves along the surface. If we assume, for simplicity, that the electrons in the free space above the surface possess a constant potential energy Φ, a one-electron wave function in this vacuum region can be written as

$$\psi_{\vec{k}_{\|}}(\vec{r}) = \sum_{\vec{K}_{\|}} a_{\vec{K}_{\|}} \exp\left\{ i(\vec{k}_{\|} + \vec{K}_{\|}) \cdot \vec{r} - \left(\sqrt{\frac{2m_e(\Phi - E)}{\hbar^2} + (\vec{k}_{\|} + \vec{K}_{\|})^2} \right) z \right\}, \quad (124)$$

where E is the one-electron energy corresponding to the wave function, m_e is the mass of the electron, and z is the component of $\vec{r}$ in the direction perpendicular to the surface. The summation index $\vec{K}_{\|}$ runs over all points of the two-dimensional reciprocal lattice, while $\vec{k}_{\|}$ is a wave vector from within the first surface Brillouin zone. The decay is controlled by the terms under the square-root sign. The slowest decay is achieved if $\vec{k}_{\|} = 0$ and $\vec{K}_{\|} = 0$. The first condition simply means that the wave

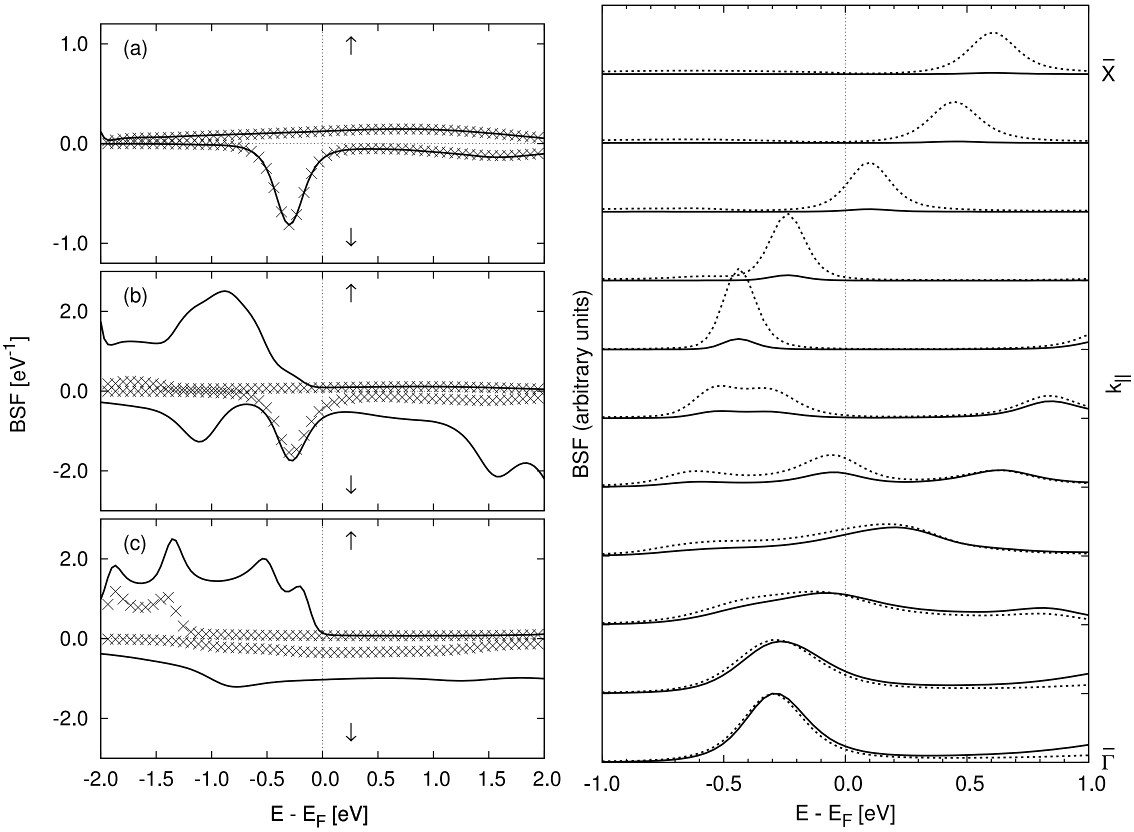

Figure 9: *Panels on the left: Spin-resolved Bloch spectral function (BSF) at the center of the Brillouin zone ($\vec{k}_\parallel = \bar{\Gamma}$) located (a) in the first vacuum layer* 0.18 *nm above the* Fe/Fe$_{0.64}$Ni$_{0.36}$ *surface, (b) on the iron surface layer, and (c) deep in the* Fe$_{0.64}$Ni$_{0.36}$ *alloy bulk. Majority-spin components are plotted in the upper (positive) half-planes, minority-spin components are flipped into the lower (negative) half-planes. The solid lines represent the complete spin-resolved BSFs, which include all orbital components, while crosses denote the sum of components projected onto the orbitals s, p_z and d_{z^2}. Panel on the right: Part of the surface-projected band structure of the* Fe$_{0.64}$Ni$_{0.36}$ *system represented by a series of the minority-spin Bloch spectral functions in vacuum 0.18 nm (dotted line) and 0.54 nm (solid line) above the surface from $\vec{k}_\parallel = \bar{\Gamma} \equiv (0,0)$ to $\vec{k}_\parallel = \bar{X} \equiv (1,0)/(\sqrt{2}a_0)$, where a_0 is the fcc lattice constant of the substrate and the axes of the coordinate system are aligned with the tetragonal lattice of the surface. Curves belonging to different $\vec{k}_\parallel$ are shifted with respect to each other vertically so as to make them distinguishable. The two sets of curves that correspond to the two different heights above the surface are scaled differently so as to compensate for the decay of the BSF magnitude when going away from the surface.*

function belongs to the point $\bar{\Gamma}$, the central point of the Brillouin zone. If $\vec{k}_{\|} = 0$, however, then the coefficient $a_{\vec{K}_{\|}}$ in front of the term with $\vec{K}_{\|} = 0$ may be non-zero only in the expansion of a wave function that belongs to the A_1 representation. The transformation properties of wave functions in other irreducible representations of the symmetry group would be violated by the presence of the term with $\vec{K}_{\|} = 0$.

The expected prevalence of electron states of the A_1 type in the vacuum region is in accord with what has been actually found about the character of the BSFs in Fig. 9. The A_1 component is just a minor part of the BSF at $\vec{k}_{\|} = \bar{\Gamma}$ deep in the bulk for energies around the Fermi level—see panel (c) in the left-hand column of Fig. 9—but it becomes the only noteworthy component of the BSF at $\vec{k}_{\|} = \bar{\Gamma}$ in the vacuum for the same energies—panel (a) in the same column. The panel (b), which shows the BSF again for $\vec{k}_{\|} = \bar{\Gamma}$ but in the top surface layer, reveals the presence of several surface resonances; apart from the resonance in the minority-spin channel 0.3 eV below the Fermi level, there is another minority-spin resonance about 1.1 eV below the Fermi level and a majority-spin resonance 0.8 eV below the Fermi level. However, only the resonance at 0.3 eV below the Fermi level originates from the A_1-type electron states and only this one extends substantially above the surface. Since the valence electron states in both iron and nickel have a predominantly d-orbital character, we may characterize this surface resonance as being d_{z^2}-like. Similar electron states near the center of the Brillouin zone with a prevailing d_{z^2}-like component have been previously demonstrated to cause peaks in differential tunneling conductance (measured in the STS) on the clean Fe(001) and Cr(001) surfaces [40] and at atoms of various $3d$ metals incorporated as impurities into the Fe(001) surface [43].

The panel on the right-hand side of Fig. 9 shows a series of the minority-spin components of BSFs in vacuum above the surface for various Bloch vectors $\vec{k}_{\|}$ in the surface Brillouin zone. This kind of graph is analogous to a vacuum-projected electron band structure of an ordered periodic system, as it also illustrates the energy dispersion of the electron states in the Brillouin zone. We see that the surface resonance is significant only in the close vicinity of $\bar{\Gamma}$. The position of the peak exhibits a notable dispersion in energy together with a broadening of the peak and a reduction of its height as going away from the center of the Brillouin zone. There are also other features in the BSF, apart from the peak at $\vec{k}_{\|} = \bar{\Gamma}$ and about -0.3 eV, which appear at different energies and in various parts of the surface Brillouin zone if one looks into the vacuum close enough to the surface, but these other features quickly decay with increasing distance from the surface, as the comparison between the dotted and the solid curves on the right-hand panel of Fig. 9 makes clear. The large energy dispersion in the vicinity of $\bar{\Gamma}$, however, causes a significant broadening of the peak in the vacuum-projected DOS at -0.3 eV with respect to the corresponding sharp peak in the BSF right at $\vec{k}_{\|} = 0$ (cf. Fig. 5, the left-hand side and the right-hand side panel, respectively). In spite of the broadening effect of the large dispersion around $\bar{\Gamma}$, which affects the peak in the LDOS (or projected DOS) above the surface, the experiment still yields a clearly distinguishable peak in the differential conductance at -0.35 V. This observation suggests that interaction with the tip of the STM, which was completely disregarded in the simple consideration based on the LDOS, enhances the relative contribution of the electronic states at $k_{\|} = 0$ to the tunneling current at the expense of the contributions from the other parts of the surface Brillouin zone.

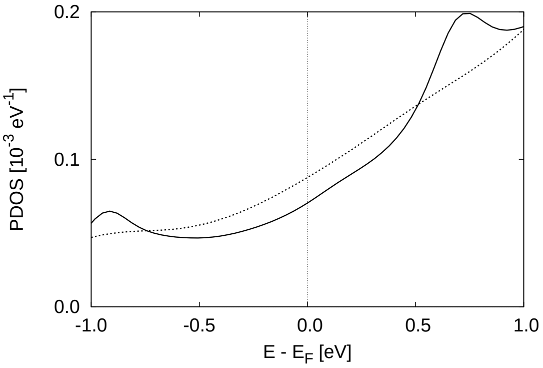

Figure 10: *Projected density of states 0.54 nm above the* $c(2 \times 2)$ *ordered* FeNi/$Fe_{0.64}Ni_{0.36}$ *surface (solid line) in comparison with the analogous projected DOS above a disordered surface with the same chemical composition,* $p(1 \times 1)$ $Fe_{0.5}Ni_{0.5}/Fe_{0.64}Ni_{0.36}$ *(dotted line).*

Based on the results of the calculations, one would expect the feature in tunneling conductance at -0.35 V to occur locally above iron-rich areas of the surface. The STS, nonetheless, shows the presence of this feature all over the alloy surface, although it is more pronounced at some locations than at others. One may ask how much the assumption of a complete chemical disorder on the surface affects the theoretical results—especially since we know from the corroborative evidence of the STM images and total energy calculations that a $c(2 \times 2)$ pattern of alternating Fe and Ni atoms tends to form on the surface. In order to check the importance of the local ordering, the LDOS should be calculated above an ordered surface of the alloy and compared with a corresponding LDOS above a completely disordered surfaces with the same layer-by-layer chemical composition. A disordered $Fe_{0.64}Ni_{0.36}$ substrate covered with one atomic layer of an ordered $c(2 \times 2)-$FeNi structure has been chosen as an example of the ordered surface. The projected DOS above this surface is to be compared with the projected DOS above the $Fe_{0.64}Ni_{0.36}$ substrate covered with one atomic layer of a completely disordered $Fe_{0.5}Ni_{0.5}$ surface alloy. The comparison is made in Fig. 10. Obviously, the surface ordering does not introduce any new feature into the vacuum LDOS (or PDOS) at energies around 0.3 eV below the Fermi level. The conclusions drawn from Figs. 5–7 can be thus generalized to the case of surfaces with a partial chemical order. The formation of the experimentally detected surface resonance even above surface areas with an approximately equal content of iron and nickel in the topmost layer must be caused by some other reason than the partial ordering, probably again by an enhancement of the resonance by an interaction with the tip.

3.4 Summary of results for the $Fe_{0.64}Ni_{0.36}$ (001) surface

The low-bias STM images taken on the (001) oriented surface of the fcc substitutional $Fe_{0.64}Ni_{0.36}$ alloy (Invar) allow the experimentalists to identify the Fe and Ni atoms on the surface. The images reveal a slight enrichment of the top surface atomic layer by Ni atoms ($\approx 41\,\%$ of Ni atoms on the surface as compared to the $36\,\%$ in the bulk) and a formation of $c(2 \times 2)$ FeNi patches on the surfaces separated mainly by Fe-rich boundaries. The Fe atoms appear as brighter spots (higher-reaching protrusions) in the STM images in comparison with the less bright (less protruding) Ni atoms. This observation is in accord with the buckling of the (001) surface that has been calculated for several models of an FeNi alloy. The calculated atomic positions on the surface were always such that the Fe atoms were positioned higher (farther from the substrate) than the Ni atoms. Moreover, the buckling of the surface layer also turns out to be influenced by the composition of the sub-surface layers, which explains the additional modulation of the apparent height in the STM images that obscures the Fe vs. Ni chemical contrast. The prevalence of the $c(2 \times 2)-$FeNi areas on the surface is consistent with what can be expected from comparing the various surface models in terms of the calculated total energy.

The electronic structure calculations show that the peak in the differential tunneling conductance that has been found by the STS at the voltage bias of about -0.35 V can be explained by a surface resonance at the corresponding energy below the Fermi level. The resonance has been found to arise on iron-rich surfaces of the FeNi alloy at the center of the surface Brillouin zone and in its close vicinity. The electron states that compose the surface resonance have a predominantly d_{z^2}-orbital character. Its reciprocal-space location and its d_{z^2} character allow the surface resonance to protrude far into the vacuum potential barrier above the surface. The height of the tunneling-conductance peak and its sharpness greatly varies among different regions of the surface. The results of the electronic structure calculation suggest that the parts of the surface above which the STS detects the strongest peak are the areas where the content of Fe atoms locally exceeds the average iron content on the surface. However, the origin of the tunneling-conductance peak in areas with approximately equal content of Fe and Ni, in which the peak is weaker but still discernable, remains unclear. Its explanation would require a much more detailed treatment, one which would have to take into full account the probing tip of the STM and its interaction with the surface. Such a treatment would not be limited to describing the ground state of the tip-sample system but it would rather handle the out-of-equilibrium state brought about by the flowing electric current.

4 Layers of $3d$ transition metals on the tungsten (001) surface

Spin-polarized scanning tunneling microscope (to be abbreviated SP-STM, see e.g. [4] for a review of this experimental method) enlarges the range of potential applications of the STM by allowing us to study the *magnetic* structure of surfaces at the atomic level. The sensitivity of the SP-STM to local magnetization makes it a precious tool for exploring complex or disordered surface magnetic structures, which would be difficult to probe with other, less localized experimental methods (based on, e.g., X-ray magnetic dichroism, magneto-optical Kerr effect, neutron scattering, etc.). An example of a magnetic structure successfully determined by the SP-STM is the $c(2 \times 2)$ antiferromagnetic structure of one atomic layer of iron on the (001) tungsten surface [44]. Although this particular surface structure is neither disordered nor very complex, its magnetic properties are still difficult to probe with non-local experimental methods because of its zero total magnetization. While previous experiments indicated that the Fe monolayer on W(001) possessed no macroscopic magnetization (see references in [44]), the question whether the iron layer was truly non-magnetic (with no magnetic moments even at the atomic level) or antiferromagnetic or whether it had perhaps an even more complicated magnetic structure (spin spirals, for example) had not been settled until the application of the SP-STM. The SP-STM clearly showed the checkerboard pattern arising from the $c(2 \times 2)$ periodicity of the antiferromagnetic structure. The magnetic origin of the $c(2 \times 2)$ pattern was confirmed by a contrast inversion which occurred when switching the magnetization of the tip into the opposite direction. Moreover, it could be also established that the magnetization of the surface in question was out of plane (perpendicular to the surface) rather than in plane, since the magnetization of the tip had to be perpendicular to the surface plane so as to observe the checkerboard pattern. The experimentally observed antiferromagnetic ground state is in accord with the results of *ab-initio* calculations [44, 45]. The successful study of Fe/W(001) initiated a theoretical analysis of other $3d$ transition metals in a monoatomic layer on the (001) tungsten surface [46]. This analysis provided quite surprising conclusions regarding the magnetic order of the investigated monolayers. Like the iron monolayer, also the cobalt monolayer was predicted to be $c(2 \times 2)$ antiferromagnetic, nickel monolayer was shown to be non-magnetic, while the monolayers of vanadium, chromium, and manganese were found to be ferromagnetic. Such a trend along the row of the $3d$ elements is almost exactly the opposite of what is known from the corresponding bulk materials or from monolayers on some other substrates. Bulk iron and cobalt (and nickel too) are ferromagnets while chromium and manganese assume more complex magnetic structures akin to antiferromagnetism (see [47] and references therein for the magnetic properties of Cr and [48, 49] for Mn). Vanadium is paramagnetic as a bulk material, although its clean (001) surface may be ferromagnetic—the issue regarding the vanadium surface is still controversial [50, 51]. Furthermore, V, Cr, and Mn monolayers are $c(2 \times 2)$ antiferromagnets and Fe and Co monolayers are ferromagnets on, e.g., Pd(001) or Ag (001) surfaces [52, 53]. Fe is known to be ferromagnetic even in a monolayer on a crystallographically different tungsten surface, W(110) [54], while a monolayer of Mn on W(110) tends to an antiferromagnetic magnetic order [55]; the latter fact has been also revealed by the SP-STM. Similarly, a Cr monoatomic layer on the W(110) has been found to display a $p(2 \times 1)$ (row-wise) antiferromagnetic order [56]. The Mn/W(110) monolayer actually exhibits a more complex magnetic order than the simple $c(2 \times 2)$ antiferromagnetic pattern. It has been shown recently [57] that the local magnetic moments of Mn atoms on W(110) are arranged in spin spirals, in which neighboring Mn atoms bear nearly but not exactly opposite magnetic moments. The possibility that such complex magnetic structures occur on the W(001) cannot be excluded either, and indeed, spin spirals in Mn/W(001) have been also reported [58].

The magnetic properties of the $3d$ transition metals on the (001) tungsten surface get even more complicated if some disorder is introduced into the overlayers. This can be done by mixing more $3d$ elements on the surface, thus forming a two dimensional alloy. In thinner than monolayer films, a surface site may be either empty or occupied by an atom of the $3d$ adsorbate, which also contributes to the disorder if the vacancies and adsorbate atoms are distributed in a random way. In both cases, new phenomena can potentially arise, not only due to the disorder but also due to the mere presence of more than one element (in the two-dimensional alloys) or due to the the presence of vacancies and a reduced number of the nearest neighbors surrounding a typical surface atom (in the submonolayer films). A local-probe method like the SP-STM would be an outstanding tool to study such disordered overlayers. However, the interpretation of the SP-STM scans also becomes more difficult as compared to those obtained for the chemically pure complete monolayers, because the magnetic sources of contrast become entangled with the chemical and geometrical ones. A theoretical survey of the disordered surface structures that would reveal what effects can be expected on such surfaces is therefore desirable, as it will be useful for the interpretation of future experimental studies. In the subsequent parts of this thesis, I will proceed to carry out a theoretical study on model systems representing two-dimensional alloys as well as incomplete overlayers on the W(001) surface [59, 60, 61]. I will mainly focus on the zero-temperature magnetic properties of these systems.

4.1 Binary surface alloys

4.1.1 Methods and notation

The goal of this section is to explore the magnetic properties of chemically disordered monoatomic layers on the W(001) substrate that consist of two different $3d$ metals. Special attention will be devoted to the overlayers that are composed of two metals one of which alone would form a ferromagnetic monoatomic layer on the surface while the other one would be antiferromagnetic in a chemically pure monoatomic layer. The impact of alloying is expected to be especially interesting in the case of such layers because of the competing tendencies to different types of magnetic ordering.

In the subsequent calculations, I will assume that the atoms of the two elements are distributed in a completely random way amongst the available surface sites. The probability for an atom of a particular element to occupy a particular site will

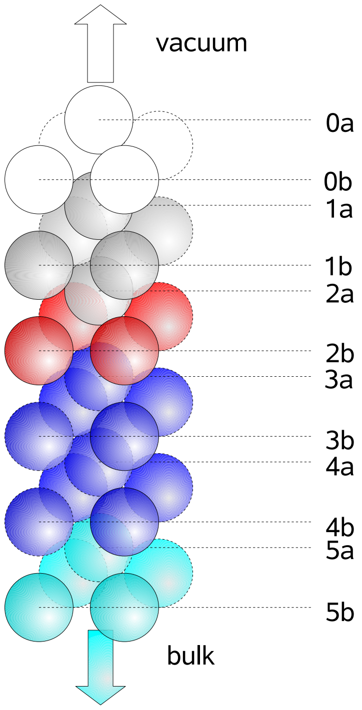

Figure 11: *One unit cell of the structure under investigation, as it was represented in the LMTO-ASA calculations. White spheres represent part of the semi-infinite vacuum region with the free-space effective potential, gray spheres represent the vacuum near the surface (where the electrons leaking out from the surface modify the effective potential), red spheres represent the atoms of* 3d *transition elements which form the monoatomic overlayer, blue spheres stand for tungsten atoms in the surface region, and cyan spheres represent tungsten atoms in the semi-infinite region with the bulk effective potential. The labels in the picture denote individual atomic layers; the principle layers are numbered while atomic layers within one principle layer are distinguished by letters.*

be independent from the atoms occupying the neighboring sites. Furthermore, the same occupational probabilities will be assumed for every surface site. Each of the investigated surface layers thus represents a homogeneous two-dimensional binary alloy. Pseudomorphic growth on the (001) surface of the body centered cubic (bcc) tungsten crystal is assumed, so the ‘surface sites’ will always be fourfold hollow positions on the W(001) surface. The fourfold hollow position was indeed shown to be the preferred adsorption position for Fe on W(001) [62] and it is expected to be the preferred one for the other elements too. The chemically disordered surface layers that conform to the above assumptions are represented within the CPA (see Section 2.11) by a $p(1 \times 1)$ periodic structure, which contains only one surface atom in the two-dimensional unit cell. The actual structure of the surface films may approach our models with total chemical disorder more or less, depending on the details of how the films would be prepared (the deposition rate and temperature, subsequent annealing and/or quenching, etc.).

A computer code based on the LMTO-ASA method and on the CPA approximation was used as the primary tool for the theoretical investigation of the two-dimensional binary alloys on the W(001) surface. The surface Green's function formalism (SGF) implemented in this code (see [24]) allows for smooth matching of the surface region to the bulk. The self-consistent electronic structure of the bulk material has to be provided by an independent calculation. In our case, the bulk material is the bcc crystalline tungsten. The atomic-sphere radius $r_{\mathrm{W}} = 0.1558$ nm was used for tungsten, corresponding to the value of the bulk lattice parameter $a_{\mathrm{W}} = 0.3165$ nm known from experiment [63]. The surface region was modelled by 4 atomic layers of tungsten, one atomic layer with variable composition standing for the overlayer, and three layers of empty atomic spheres that represented the vacuum above the surface (see Fig. 11, layers 1a–4b). The boundary conditions reflected the fact that the surface region was attached to a semi-infinite region of the bulk tungsten on one side and to a semi-infinite vacuum region on the other side. The atomic spheres in the surface region were arranged in such a way that they formed an ideal continuation of the bcc lattice of the bulk tungsten. A possible influence of the surface relaxation on the magnetic properties will be discussed later.

The off-diagonal elements of the TB-LMTO effective Hamiltonian matrix are negligible if they connect two distant atomic layers. The criterion that decides which off-diagonal elements are taken into account and which are not is specified within the SGF formalism by means of so called *principal layers.* Only matrix elements within one principal layer and elements connecting two directly neighboring principal layers are considered non-zero. Throughout the calculations discussed here, principal layers that consisted of two atomic layers each were used. This implied that off-diagonal elements between the nearest and second-nearest atomic layers were always included while off-diagonal elements between atomic layers beyond the third-nearest neighbors were always omitted. According to [24] (chapter 3.2), the off-diagonal elements beyond second-nearest atomic neighbors are negligible in the tight-binding calculations. For the division of the structural model into principal layers, refer to Fig. 11.

The reciprocal space was sampled by 15×15 $\vec{k}$-points (Bloch vectors) in the surface (two-dimensional) Brillouin zone. This sampling corresponds to 36 points in the irreducible wedge of the two-dimensional Brillouin zone (the wedge being 1/8 of the whole Brillouin zone), which is the same number as used in [46]. The basis was composed from muffin-tin orbitals with angular quantum number $l \leq 2$, or, in other words, the *spd* basis was used. The LSDA exchange-correlation potential in the parameterization of Vosko, Wilk, and Nusair [41] was employed in the calculations performed by the LMTO-ASA method. The DFT self-consistent cycle had always been converged so that the calculated total energy would change by less than 10^{-6} Ry ($\approx 10^{-5}$ eV) in further iterations.

The calculations were performed for several representative magnetic configurations of the two-dimensional surface alloys. The representative configurations were chosen so that the $p(1 \times 1)$ surface unit cell were preserved in the spin-polarized CPA calculations. Note that the $c(2 \times 2)$ antiferromagnetic order does not belong to such magnetic configurations. A spin-polarized calculation consists in considering the energy functional of the DFT as a functional of two separate densities, those of the 'spin-up' and the 'spin-down' electrons. Accordingly, the axial vectors representing local magnetic moments of individual atoms are allowed to orient in only two different mutually opposite directions. The models of the magnetic binary alloys that conform to the so-far imposed restrictions can be described in a formal way as a four-component homogeneous alloy: each of the two elements contained in the alloy is represented by two components that differ in the direction of their local magnetic moments. The chemical and magnetic composition of such alloys is given by the general formula

$$\mathrm{X}_{\alpha}^{\uparrow}\mathrm{X}_{\beta}^{\downarrow}\mathrm{Y}_{\gamma}^{\uparrow}\mathrm{Y}_{\delta}^{\downarrow}, \tag{125}$$

where the symbols X and Y represent two ($3d$-transition) elements, the superscripts $\uparrow$ and $\downarrow$ distinguish the two opposite orientations of the local magnetic moments, and α, β, γ, and δ are real numbers that denote the proportion of the respective kinds of atoms (the atomic fraction) on the surface. At the same time, α, β, γ, and δ also express the probability that a particular surface site would be occupied by an atom of the respective element with the respective orientation of magnetic moment. Since there is only one surface atomic site per surface unit cell, all the surface sites are equivalent in the statistical sense, or, in other words, the same probabilities apply for an arbitrary surface site. In the following, I shall relabel the probabilities (or atomic fractions) in an intuitive way:

$$x^{\uparrow} \equiv \alpha, \tag{126a}$$

$$x^{\downarrow} \equiv \beta, \tag{126b}$$

$$y^{\uparrow} \equiv \gamma, \tag{126c}$$

$$y^{\downarrow} \equiv \delta. \tag{126d}$$

Furthermore, $x = x^{\uparrow} + x^{\downarrow}$ will denote the relative amount of all atoms of element X, and, similarly, $y = y^{\uparrow} + y^{\downarrow}$ will denote the relative amount of element Y. The condition

$$x + y = 1 \tag{127}$$

has to be fulfilled, so as to ensure that all surface sites are occupied by an atom and the binary alloy thus forms a complete monolayer on the surface. The cases of incomplete coverage will be treated in the next section.

Let me now introduce a few magnetic states of the surface alloy to which special attention is going to be devoted. All of them can be represented by the above given formula (125). First, it is the ferromagnetic state (FM), in which the magnetic moments of all atoms point in the same direction. The general formula for a ferromagnetic surface film will be $\mathrm{X}_{x}^{\uparrow}\mathrm{Y}_{1-x}^{\uparrow}$. Another notable magnetic state is that of *disordered local moments* (DLM), which is characterized by randomly oriented local moments with a uniform probability distribution over all possible directions in space. Although the DLM state may seem to fall out of reach of the simple spin-polarized calculations, because it involves all possible orientations of local magnetic moments rather than magnetic moments aligned with a preferred magnetization axis, it can be proven [64] that as long as the CPA description is concerned, the DLM state is equivalent to a random two-component mixture of 50 % atoms with an 'upward' orientation of their magnetic moments and another 50 % atoms with the opposite ('downward') orientation of magnetic moments. We thus arrive at the formula $\mathrm{X}^{\uparrow}_{x/2}\mathrm{X}^{\downarrow}_{x/2}\mathrm{Y}^{\uparrow}_{(1-x)/2}\mathrm{Y}^{\downarrow}_{(1-x)/2}$ for a binary alloy in the DLM state.

The DLM state described by the last formula somewhat resembles the antiferromagnetic state. Just as in the antiferromagnetic state, there are local magnetic moments of opposite orientations and both of these orientations of the magnetic moments occur for exactly half of the atoms, resulting in zero total magnetization. However, while the antiferromagnetic state is ordered, the DLM state is a disordered one, lacking not only the long-range but even any short-range order. In spite of this important difference, we may still expect that whenever the antiferromagnetic state is favored over the ferromagnetic one (i.e., when the former possess lower total energy than the latter), the DLM state will be most probably also favored over the ferromagnetic state, although typically not over the antiferromagnetic state. The reason for this is that the mutual orientation of local magnetic moments at nearest neighboring atoms usually decides about total energy differences between the various magnetic states: either parallel or antiparallel alignment of neighboring local moments turns out to be preferable. If the antiparallel alignment (as in the antiferromagnetic state) bears lower energy than the parallel alignment (present in the ferromagnetic state), the DLM state in which pairs of nearest neighbors with both parallel and antiparallel mutual alignment can be found will be something in between from the point of view of the total energy: favored over the ferromagnetic state but less preferable than the antiferromagnetic state. As far as we avoid investigating the antiferromagnetic states, the preference for a DLM state is a good indication that in fact an antiferromagnetic state would be preferred, possibly being the ground state.

The next special magnetic state to be treated here is the 'antiparallel arrangement of (the local magnetic) moments' (APM). In contrast to the DLM or FM state, this state is defined specifically for the binary alloys and it would make no sense to introduce it for a system with only one chemical component. The formula that defines the APM state reads $\mathrm{X}^{\uparrow}_{x}\mathrm{Y}^{\downarrow}_{1-x}$. Just like the DLM is a disordered analogy to the antiferromagnetic state, the APM can be viewed as a disordered analogy to an ordered ferrimagnetic state. A ferrimagnetic state is characterized by two classes of lattice sites that possess local magnetic moments of different magnitudes and possibly also of opposite orientations. In the APM state, all lattice sites are statistically equivalent, but there are atoms of two different elements. The equivalence of the lattice sites in the APM state stems from the fact that any site may be occupied by an atom of either element and the probabilities of being occupied by a given kind of atom are the same for all sites. The atoms of the two elements, however, carry magnetic moments that have generally different magnitudes and that are aligned in mutually opposite directions. A tendency towards the APM state indicates that the local magnetic moment of each atom tends to align parallel to local moments of neighboring atoms of the same element, but antiparallel to the local moments of atoms of the other element.

Finally, I will adopt the notation DLM(X)+FM(Y) to refer to the states that are described by the formula $\mathrm{X}^{\uparrow}_{x/2}\mathrm{X}^{\downarrow}_{x/2}\mathrm{Y}^{\uparrow}_{1-x}$. Recall that the binary surface systems in which we are primarily interested are composed of one component (say, Y) that

abbreviation	**formula**	$p_{\mathbf{X}}$	$p_{\mathbf{Y}}$
FM	$\mathrm{X}^{\uparrow}_{x}\mathrm{Y}^{\uparrow}_{1-x}$	+1	+1
DLM	$\mathrm{X}^{\uparrow}_{x/2}\mathrm{X}^{\downarrow}_{x/2}\mathrm{Y}^{\uparrow}_{(1-x)/2}\mathrm{Y}^{\downarrow}_{(1-x)/2}$	0	0
APM	$\mathrm{X}^{\uparrow}_{x}\mathrm{Y}^{\downarrow}_{1-x}$	+1	−1
DLM(X)+FM(Y)	$\mathrm{X}^{\uparrow}_{x/2}\mathrm{X}^{\downarrow}_{x/2}\mathrm{Y}^{\uparrow}_{1-x}$	0	+1

Table 3: *Summary of the notation for several special magnetic states of the two-dimensional binary alloys. The alloys are composed of two 3d transition metals, denoted here as X and Y, deposited on the W(001) surface. The up- or down-pointing arrows label components with different orientation of the atomic magnetic moments. The quantities in the last two columns, p_X and p_Y, describe the degree of 'polarization' with respect to the orientation of local magnetic moments.*

exhibits a ferromagnetic coupling between its atoms and of another component (component X) that exhibits an antiferromagnetic coupling. For this kind of alloys, the magnetic state DLM(X)+FM(Y) lets each component retain its 'natural' magnetic state, at least within the limits imposed by our restriction to the $p(1 \times 1)$ surface unit cell, which forces us to replace the antiferromagnetic state with the DLM one. If the interaction between atoms of different elements (i.e. between X and Y) were negligible, the DLM(X)+FM(Y) magnetic state could be expected to be close to the ground state. There is, however, no reason why the assumption of negligible interaction between X and Y should hold in general. Therefore the actual ground state may considerably differ from the DLM(X)+FM(Y) model configuration.

The notation for all the above discussed special magnetic states is summed up in Tab. 3. The last two columns of the table describe the magnetic states in terms of the quantities defined as

$$p_X = \frac{x^{\uparrow} - x^{\downarrow}}{x^{\uparrow} + x^{\downarrow}}, \tag{128a}$$

$$p_Y = \frac{y^{\uparrow} - y^{\downarrow}}{y^{\uparrow} + y^{\downarrow}}. \tag{128b}$$

We can interpret these quantities as a degree of 'polarization' of magnetic moments found for atoms of the respective elements: $p_X = 0$ means randomly oriented magnetic moments of atoms X while $p_X = 1$ means that all magnetic moments of atoms X are aligned in one direction. The sign of either p_X or p_Y can be chosen arbitrarily, it only matters whether the signs of p_X and p_Y are the same or the opposite.

4.1.2 Results for the special magnetic states

The results of total energy calculations for varying composition of the surface layer and for different magnetic states are summarized in Figs. 12 and 13. The total energies of distinct magnetic states for one given chemical composition are plotted as differences from the energy of the corresponding DLM state, which thus serves as a zero-energy level. Each panel in the two figures covers one particular system of two 3*d* transition metals on the tungsten surface. The composition of the surface

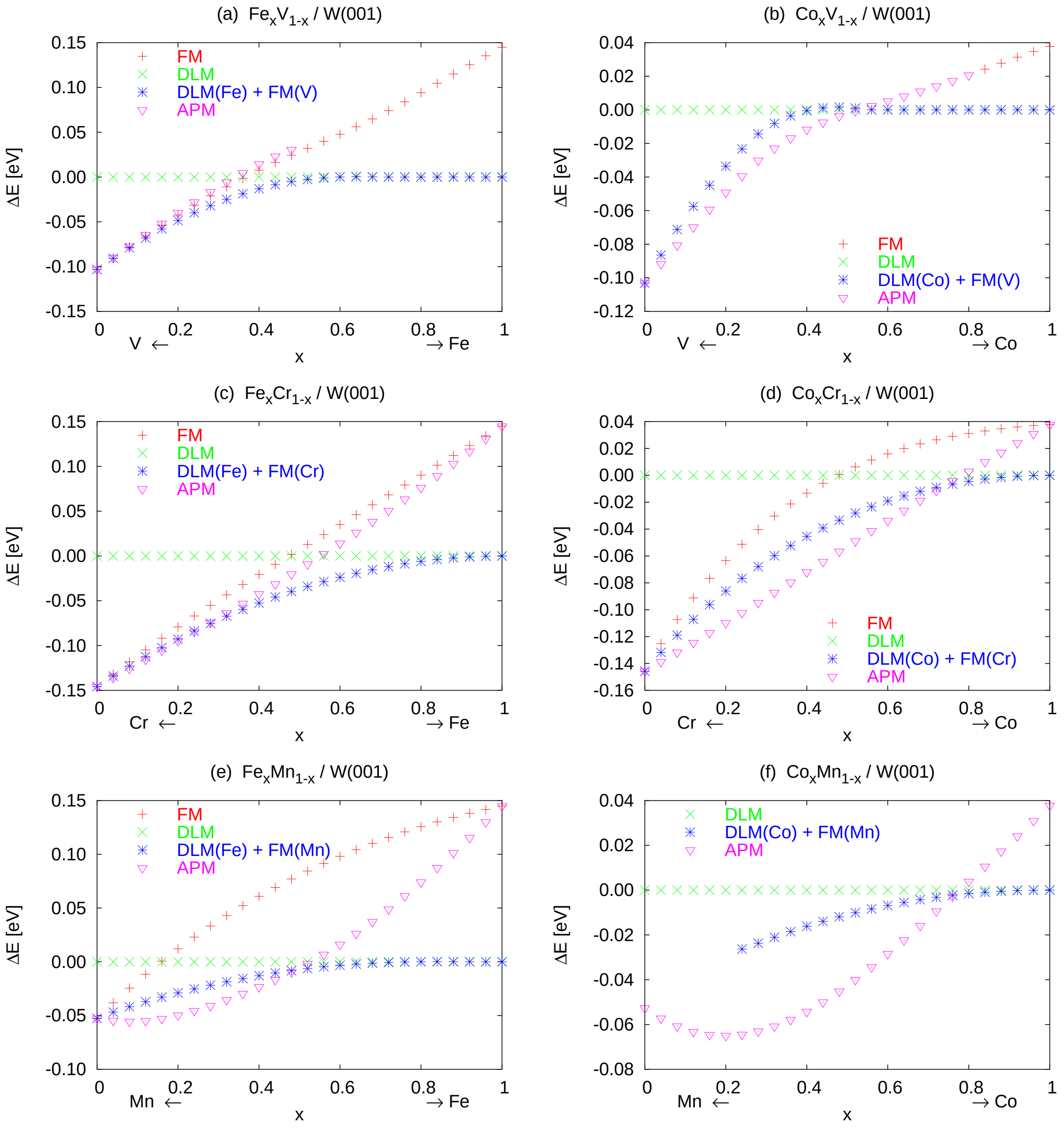

Figure 12: *Differences between the total energies of various magnetic states as a function of the surface composition are shown here for the following surface binary alloys: (a) iron with vanadium, (b) cobalt with vanadium, (c) iron with chromium, (d) cobalt with chromium, (e) iron with manganese, and (f) cobalt with manganese. The total energy of the DLM state is used as the zero energy level in all cases. The abbreviations used to label the magnetic states are explained in the text.*

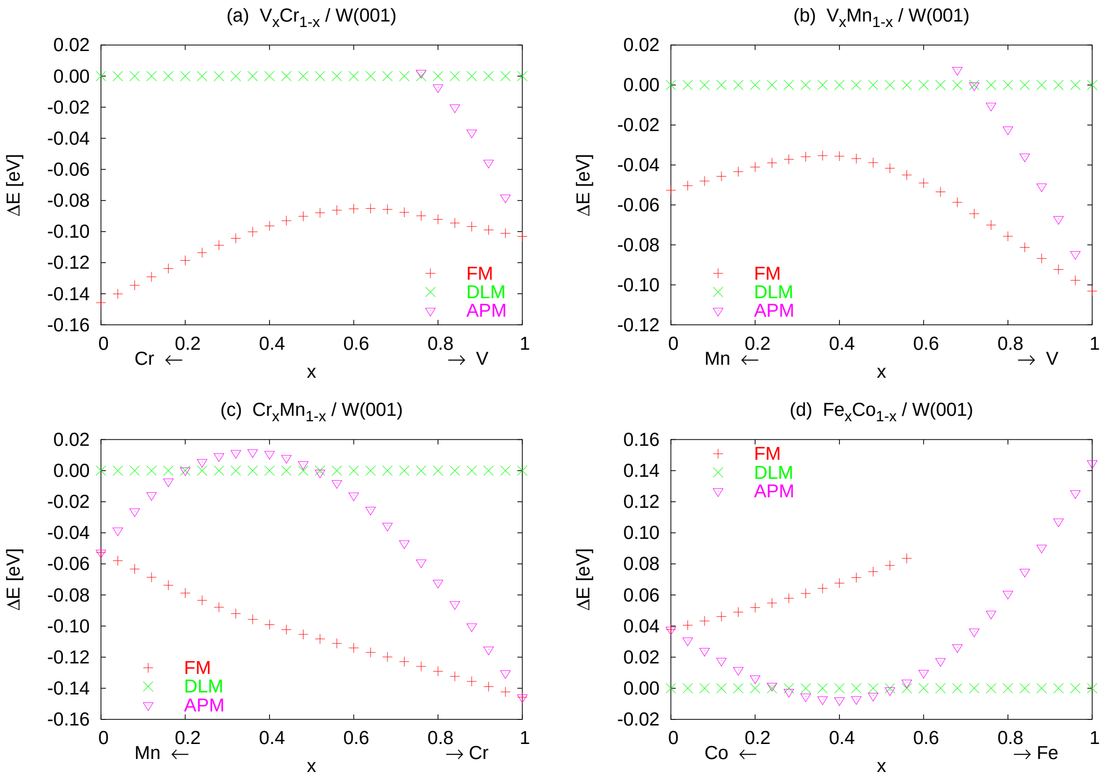

Figure 13: *Differences between the total energies of various magnetic states as a function of the surface composition are shown here for the following surface binary alloys: (a) vanadium with chromium, (b) vanadium with manganese, (c) chromium with manganese, and (d) iron with cobalt.*

alloy changes along the horizontal axis, beginning with a pure monolayer of the first component on the left and ending with a pure monolayer of the second element on the the right. The magnetic states are distinguished from each other by different shapes and colors of the symbols. When a symbol for a particular magnetic state is missing at some composition of the alloy, the self-consistent DFT solution corresponding to that particular magnetic state and composition has not been found. The non-existent solutions and solutions with very high total energy are of little interest here anyway. Our analysis should rather focus on magnetic configurations that have comparatively low total energy and hence a good chance to be close to the ground state.

Let me begin the discussion with the alloys composed of one element that tends to ferromagnetic coupling between its atoms (V, Cr, or Mn) and one that tends to antiferromagnetic coupling (Fe or Co). The results for such surface alloys are shown in Fig. 12. First, note the leftmost and rightmost points of the graphs, which represent the total energy of various magnetic states of chemically pure monoatomic layers. As could be expected based on the findings of Ferriani et al. [46], the FM state turns out to be that with the lowest total energy for the V, Cr, and Mn monolayers, while the DLM state assumes the lowest energy (among the magnetic states considered here) in the case of the Fe and Co monolayers. Actually, I have also recalculated the total energies of the pure Fe and pure Co monolayers in the ordered $c(2 \times 2)$ antiferromagnetic state, using the TB-LMTO ASA method. My calculation has confirmed that the antiferromagnetic states have lower energy than both the FM and the DLM states. In the case of the Fe monolayer, I have found the total energy of the $c(2 \times 2)$ antiferromagnetic state to be lower than the energy of the DLM state by 135 meV per Fe atom. The difference between the FM state of the iron monolayer and the antiferromagnetic one then amounts to 279 meV per Fe atom. In the case of the Co monolayer, I have found the $c(2 \times 2)$ antiferromagnetic state to have lower total energy than the DLM state by 49 meV per Co atom. The difference between the FM state of the cobalt monolayer and its antiferromagnetic state is then 87 meV per Co atom. For comparison, Ferriani et al. found the energy of the $(c2 \times 2)$ antiferromagnetic state of Fe monolayer to be about 150 meV per Fe atom below the ferromagnetic state and the energy of the $(c2 \times 2)$ antiferromagnetic state of Co monolayer to be about 60 meV per Co atom below the ferromagnetic state. Considering that my computational method (TB-LMTO) was substantially different from the method used by Ferriani et al. (FP-LAPW with surface relaxation taken into account), the agreement of our results is reasonable.

Although those magnetic states that can be meaningfully defined only for a two-component surface alloy, like APM and DLM(X)+FM(Y), can be studied theoretically even near the limits of a chemically pure overlayer, the component whose content in the surface alloy almost vanishes does not substantially influence the total energy of the system. Therefore the energy of the APM state coincides with the energy of the FM state at both limits of the composition range, just as it can be seen in the corresponding figures. Similarly, the energy of the DLM(X)+FM(Y) state also approaches the energy of the FM state for an almost pure overlayer composed mainly of the element X, while it approaches the energy of the DLM state for an almost pure overlayer composed mainly of Y.

Now, we turn our attention to the cases of intermediate composition, in which a non-zero amount of both components is present in the surface alloy. Notice that for most pairs of elements XY, there exists certain composition range in which DLM(X)+FM(Y) possesses lower total energy than all the other plotted special magnetic states. The DLM(X)+FM(Y) mostly remains the preferred magnetic state as long as the alloy is rich in the X component. Here, the component X may be either Fe or Co, while Y may be Cr or Mn. The alloys containing vanadium behave differently to some extent and they will be discussed later. The observed preference for the DLM(X)+FM(Y) state can be understood in the following way: The antiferromagnetic coupling between atoms of component X prevails in the X-rich overlayers over other tendencies . Since the antiferromagnetic state of the binary systems has not been considered, the tendency to the antiparallel alignment of magnetic moments is best satisfied in the DLM state. Therefore the component X assumes the DLM state. The local magnetic moments at atoms of the other component, Y, may be pushed to assume some particular orientation with respect to the local magnetic moments of X. Nevertheless, since the local magnetic moments of X are disordered, there is no particular orientation the magnetic moments of Y could be forced to reach by the interaction with X. The ferromagnetic coupling among the atoms of Y thus becomes decisive. The result is—at least in our restricted space of magnetic configurations—the DLM(X)+FM(Y) magnetic state.

The balance of the interactions changes as the content of element X decreases and the content of Y increases. On the one hand, the component Y retains the parallel alignment of its local magnetic moments. In fact, the tendency to the parallel alignment among the local magnetic moments of Y becomes even stronger with a larger amount of Y. On the other hand, the quest for the antiferromagnetic configuration inherent in the component X may be overridden by the tendency of its local magnetic moments to achieve some definite orientation with respect to the local magnetic moments of Y. As a consequence, the APM state assumes lower total energy than the DLM(X)+FM(Y) state (for all but one combination of elements considered, namely for FeCr, FeMn, CoV, CoCr, and CoMn) if the content of V, Cr, or Mn is sufficiently high. What a sufficiently high content of the element X is, depends crucially on the relative strength of the various types of magnetic coupling present in the alloy. The only exception from the above described behavior is the FeV overlayer, for which the favored magnetic state is the DLM(Fe)+FM(V) almost up to the limit of pure vanadium layer. A certain preference for the FM state over the APM states suggests a weak tendency to parallel rather than antiparallel alignment of the local magnetic moments between a vanadium and an iron atom. For extremely vanadium-rich layers (over 96 % vanadium, i.e. below 4 % iron), the energy of the FM state is even slightly lower than the energy of the DLM(Fe)+FM(V) state.

The properties of surface alloys containing vanadium deviate from the pattern observed in the other alloys. This difference concerns iron-rich FeV and cobalt-rich CoV overlayers. Fig. 12(a) shows the DLM(Fe)+FM(V) and DLM states of FeV as degenerate states if the Fe content is higher than about 70 %. Similarly, Fig. 12(b) shows the DLM(Co)+FM(V) and DLM states of CoV as degenerate for the Co content over about 55 %. Such a depiction may seem to indicate that there exist two distinct states with the same total energy in the above mentioned composition ranges of the FeV and CoV surface alloys. However, there is in fact only one magnetic state that is characterized by randomly oriented local moments (DLM) at cobalt or iron atoms and zero magnetic moment at vanadium atoms—see also Figs. 14(a,b) and 15(a,b). Such a magnetic state may be denoted as 'DLM(Fe)+NM(V)' or 'DLM(Co)+NM(V)', respectively, the letters NM standing for 'non-magnetic'. Since the vanadium atoms lack a magnetic moment, we cannot distinguish $V^{\uparrow}$ from $V^{\downarrow}$ as we did in Tab. 3. Looking at it from another point, we may separate the non-magnetic vanadium atoms into the $V^{\uparrow}$ and $V^{\downarrow}$ groups in an arbitrary way. Hence, the DLM(X)+NM(Y) state can be viewed as if it simultaneously complied with two formulas of Tab. 3, the one for the DLM state as well as the one for the DLM(X)+FM(Y) state. That is why I have chosen to represent the DLM+NM state as the degenerate DLM and DLM+FM states. For the CoV alloy, the genuine DLM(Co)+FM(V) never becomes the lowest energy state. The DLM+NM state is the favored one for both the iron-rich FeV and cobalt-rich CoV surface alloys. In the case of the FeV alloy, the DLM(Fe)+FM(V) is still the preferred magnetic state in a limited composition range, but it is so for the vanadium-rich layers rather than for the iron-rich ones.

Let me continue the discussion with the systems shown in Fig. 13, namely the VCr, VMn, CrMn, and FeCo surface alloys. These overlayers are composed of elements that either both display ferromagnetic coupling or that both display antiferromagnetic coupling between local magnetic moments of atoms of one particular element. The DLM+FM states have not been considered for these alloys, although a self-consistent DFT solution for a DLM+FM state may exist. The VCr, VMn, and CrMn layers remain ferromagnetic at any ratio of their two constituting elements. In contrast, we may spot the tendency of any two atoms in the FeCo surface alloy (be it two Fe or two Co atoms or one Fe with one Co atom) to align their local magnetic moments in a mutually antiparallel way. As a result of this antiferromagnetic coupling, the DLM state is favored over the other special magnetic states at the Fe-rich as well as at the Co-rich end of the composition range. Just in the intermediate case, in which the content of Fe and Co in the layer is approximately the same, the APM state prevails, having even lower total energy than the DLM state. The observation that the APM state is preferred to the DLM one around the half-to-half composition of the FeCo surface alloy indicates that the coupling of local magnetic moments between one Fe and one Co atom is stronger than the similar coupling between either two Fe or between two Co atoms.

Figs. 14 and 15 illustrate how much the magnitude of an atomic magnetic moment depends on the composition of the surface alloy in which the atom that bears the magnetic moment in question is present. In other words, the figures show how sensitive the magnitude of the magnetic moment of an atom is to the environment of that atom. The magnetic moments are calculated as the difference between the two spin-polarized electron densities integrated over the atomic sphere in the LMTO-ASA method. In the figures, I have chosen to show the magnetic moments pertaining to the DLM state because a self-consistent DFT solution that corresponds to the DLM state can be found for any composition of the surface alloy, thus allowing the comparison of the moments among different compositions. Moreover, the behavior displayed in the DLM states includes the noteworthy cases in which the spontaneous magnetization at vanadium atoms completely disappears. I have used the same range of values on the vertical axes in all panels in Figs. 14 and 15, so that the values of the magnetic moments could be easily compared between different graphs. The magnetic moments especially of the manganese and iron atoms but also of the cobalt and chromium atoms have a rather rigid magnitude, insensitive to the chemical composition of their environment. The magnetic moments of vanadium atoms behave differently; they are very sensitive to the chemical environment and, as mentioned above, they may be even quenched to zero under certain circumstances. This happens when the vanadium atom is surrounded by atoms of a different element with disordered local moments. While the graphs demonstrate the sensitivity (or insensitivity) of the atomic moments to the *chemical* composition of the environment, Tab. 4 shows their sensitivity to the *magnetic* state of the overlayer, i.e. to the orientation of the magnetic moments of surrounding atoms. The conclusions that can be drawn from the table are similar to those drawn from the graphs in Fig. 14 and Fig. 15. Again, manganese atoms turn out to possess the most rigid magnetic moment while the vanadium atoms have the most volatile magnetic moment. The almost invariant atomic magnetic moments found for the $3d$ transition metals from Cr to Co in the two-dimensional alloys on W(001) resemble the behavior of FeCo alloyed monolayers on the Cu(001) substrate studied by Turek et al. [65]. The atomic

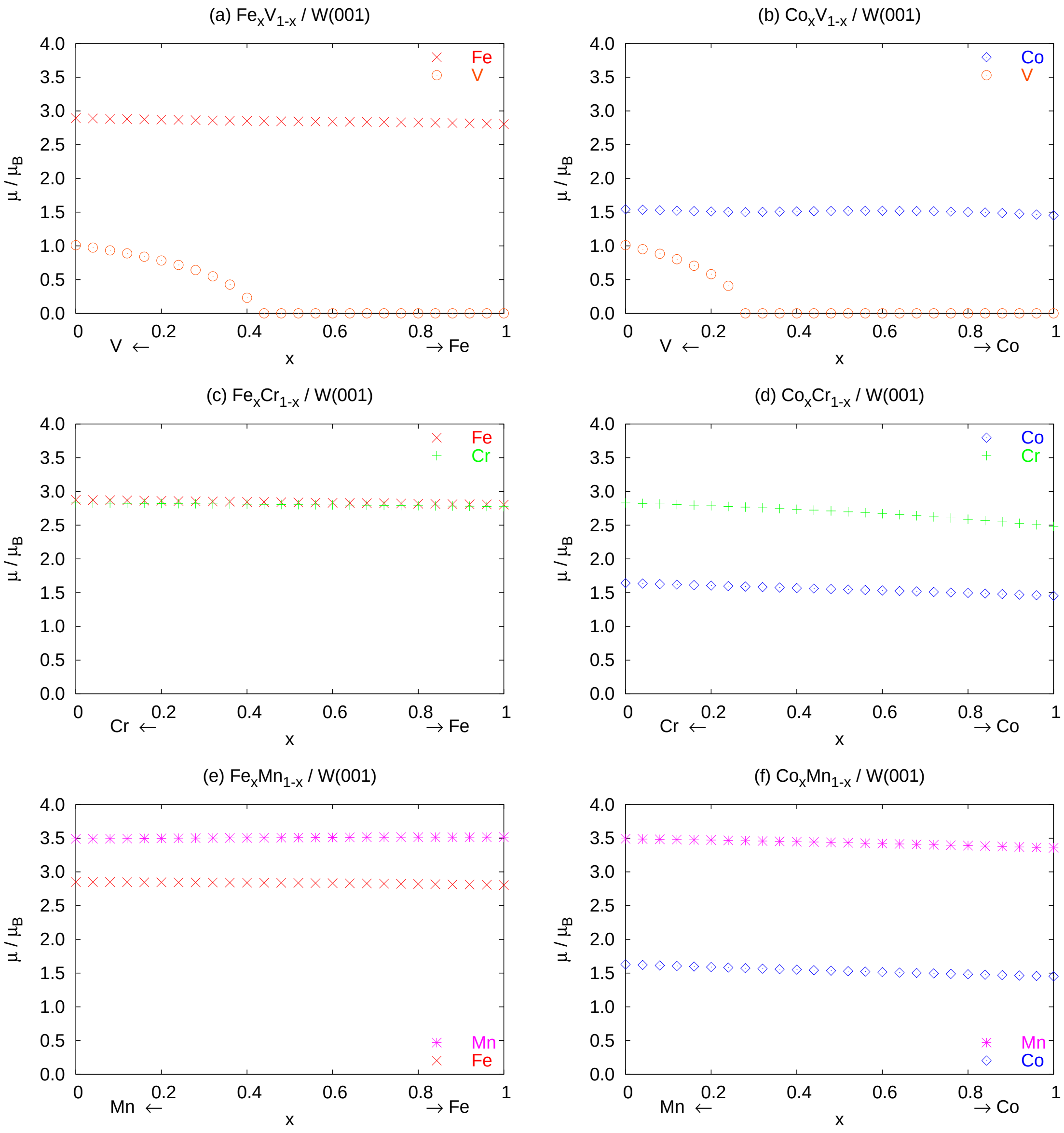

Figure 14: *Local magnetic moments at atoms of an overlayer in the DLM state as a function of the overlayer composition. Different symbols refer to atoms of different elements. The overlayer for which the values of magnetic moments are plotted consists of (a) iron (diagonal crosses) with vanadium (circles), (b) cobalt (diamonds) with vanadium, (c) iron with chromium (upright crosses), (d) cobalt with chromium, (e) iron with manganese (asterisks), and (f) cobalt with manganese, respectively.*

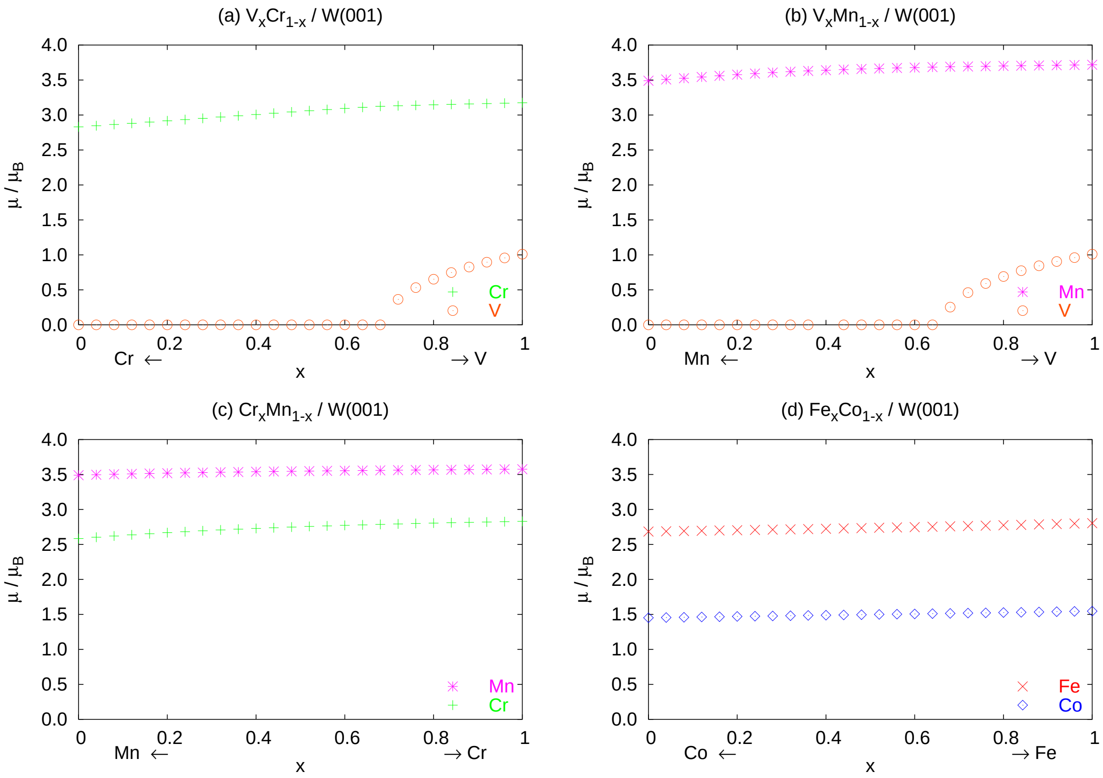

Figure 15: *Local magnetic moments at atoms of an overlayer in the DLM state as a function of the overlayer composition. Different symbols refer to atoms of different elements, like in Fig. 14. The overlayer for which the values of magnetic moments are plotted consists of (a) vanadium with chromium, (b) vanadium with manganese, (c) chromium with manganese, and (d) iron with cobalt, respectively.*

magnetic moments in the FeCo monolayers on Cu(001) exhibit only small changes with chemical composition too, in contrast to Fe-rich bulk (three-dimensional) FeCo alloys, where the magnetic moments of Fe atoms vary considerably with the Co content, leading to a non-monotonous dependence of saturation magnetization on alloy composition in the bulk case [66]. Another paper by Turek et al. [67], which deals with the surface magnetism of the FeCo and FeV alloys, also reports a behavior of the magnetic moments associated with the surface atoms that is similar to what I have found for the surface alloys on W(001): again, comparatively rigid values of magnetic moments for the Fe and Co atoms on the one hand and rather volatile magnetic moments of V atoms on the other hand.

4.1.3 More general magnetic states and a model description

So far, I have only dealt with a few selected magnetic states (FM, DLM, APM, DLM+FM). Let me now consider the most general magnetic states described by the formula (125). Such states (in which all four components are present in a non-zero amount) may be viewed as approximate representations of generalized ('uncompensated') DLM states, in which the local magnetic moments are still oriented randomly

element	**FM**	**DLM**	**change by**
V	1.58	1.01	−36.1 %
Cr	2.95	2.83	−4.1 %
Mn	3.53	3.49	−1.1 %
Fe	2.51	2.80	+11.6 %
Co	1.18	1.45	+22.9 %

Table 4: *Local magnetics moments (in Bohr magnetons) at atoms in a pure monolayer of a* 3*d transition element on the W(001) surface. Values for the DLM and FM magnetic states are given for comparison. The last column gives the relative change of the magnetic moment when going from the ferromagnetic to the DLM state.*

as in the ordinary DLM state, but with a distribution biased towards some predominant direction. As the number of possible magnetic configurations taken into account grows considerably now, it is desirable to provide the discussion of interactions between the atomic magnetic moments with a more formal basis. I will assume that the energy of the various magnetic states can be, at least approximately, described by the classical Heisenberg model,

$$E = E_0 + \frac{1}{2}\sum_{X_i,X_j} A_{ij}\cos\theta_{ij} + \sum_{X_i,Y_j} B_{ij}\cos\theta_{ij} + \frac{1}{2}\sum_{Y_i,Y_j} C_{ij}\cos\theta_{ij}, \tag{129}$$

where E_0 is the part of the total energy that is independent from the mutual orientation of local magnetic moments, the indices i and j denote individual atomic sites on the W(001) surface, the first sum runs over all pairs of sites such that both sites in that pair are occupied by the element X, the second sum runs over all pairs of sites such that the first site i is occupied by the element X and the site j is occupied by the element Y, and, finally, the third sum runs over all pairs of sites in which both sites are occupied by the element Y; θ_{ij} is the angle between the directions in which the magnetic moments of atoms at sites i and j are oriented. Furthermore, the angles θ_{ij} will be allowed to assume only two possible values, $\pm\pi$, corresponding to the 'up' and 'down' orientations of the locally prevailing spin. We thus arrive at a model akin to the Ising one. The coefficients A_{ij}, B_{ij}, and C_{ij} then represent half of the energy increase that would arise from flipping the magnetic moments of the two atoms at sites i and j from mutually parallel into mutually opposite orientation. The factors 1/2 in front of the summation signs remove a double-counting of atomic pairs. Instances in which $i = j$ are to be excluded from the summation, or, alternatively, we may put $A_{ii} = B_{ii} = C_{ii} = 0$.

We can further make use of the previously introduced assumption that there is no correlation between different sites with respect to the probability that the sites are occupied by some particular type of atom. Because of this assumption, the statistical properties of any site are fully defined by the occupation probabilities $x^{\uparrow}$, $x^{\downarrow}$, $y^{\uparrow}$, and $y^{\downarrow}$ (see Eqs. 126). Then, after averaging Eq. (129) over all possible configurations, we obtain

$$\begin{aligned} E = E_0(x,y) + \sum_{i\neq j} \Big[& \tfrac{1}{2} A_{ij} \left(x_i^{\uparrow} x_j^{\uparrow} - x_i^{\uparrow} x_j^{\downarrow} - x_i^{\downarrow} x_j^{\uparrow} + x_i^{\downarrow} x_j^{\downarrow} \right) + \\ & + B_{ij} \left(x_i^{\uparrow} y_j^{\uparrow} - x_i^{\uparrow} y_j^{\downarrow} - x_i^{\downarrow} y_j^{\uparrow} + x_i^{\downarrow} y_j^{\downarrow} \right) + \\ & + \tfrac{1}{2} C_{ij} \left(y_i^{\uparrow} y_j^{\uparrow} - y_i^{\uparrow} y_j^{\downarrow} - y_i^{\downarrow} y_j^{\uparrow} + y_i^{\downarrow} y_j^{\downarrow} \right) \Big] . \end{aligned} \tag{130}$$

Now, the energies E and E_0 stand for the configuration-averaged values of the corresponding energies that occurred in Eq. (129). If the occupation probabilities are the same for all sites, as I have assumed so far, the above formula simplifies to

$$\begin{aligned} E = E_0(x,y) \; & + \tfrac{1}{2} J_{XX} \left(\left(x^{\uparrow}\right)^2 - 2x^{\uparrow}x^{\downarrow} + \left(x^{\downarrow}\right)^2 \right) + \\ & + J_{XY} \left(x^{\uparrow}y^{\uparrow} - x^{\uparrow}y^{\downarrow} - x^{\downarrow}y^{\uparrow} + x^{\downarrow}y^{\downarrow} \right) + \\ & + \tfrac{1}{2} J_{YY} \left(\left(y^{\uparrow}\right)^2 - 2y^{\uparrow}y^{\downarrow} + \left(y^{\downarrow}\right)^2 \right) , \end{aligned} \tag{131}$$

where

$$J_{XX} = \sum_{i\neq j} A_{ij}, \tag{132a}$$

$$J_{XY} = \sum_{i\neq j} B_{ij}, \tag{132b}$$

$$J_{YY} = \sum_{i\neq j} C_{ij}. \tag{132c}$$

Making use of the notation introduced by Eqs. (128) and Eqs. (132) and considering that according to Eq. (127) $y = 1 - x$, we may rewrite Eq. (131) as

$$\Delta E = \frac{1}{2} \left[J_{XX} x^2 p_X^2 + 2 J_{XY} x(1-x) p_X p_Y + J_{YY} (1-x)^2 p_Y^2 \right] , \tag{133}$$

where $\Delta E = E - E_0(x,y)$. Since the right-hand side of Eq. (133) is zero in the DLM state, E_0 is the total energy of the DLM state and ΔE is the difference between the actual total energy and that of the DLM state, just like in Figs. 12 and 13.

Before I apply the above formalism to the magnetic states with arbitrary p_X and p_Y, let us see how well it describes the special states considered previously. As far as the surface alloys containing vanadium are concerned, our model that has lead to Eq. (133) necessarily fails. The model requires that the magnitudes of magnetic moments of individual atoms are not sensitive to the chemical and magnetic properties of the other atoms, only the orientation of the moments is influenced by interaction with the environment. This is not true for vanadium—the magnetic moment of vanadium atoms was found to change dramatically depending on the environment in which the vanadium atoms were situated. The parameters J_{XX}, J_{YY}, and J_{XY} that appear on the right-hand side of Eq. (133) are presumably dependent on the magnitude of local magnetic moments. Therefore these parameters cannot be expected to remain even approximately constant if one of the elements involved in the surface alloy is vanadium. Indeed, Eq. (133) predicts a quadratic dependence of ΔE on the alloy composition while the dependence of ΔE on the composition

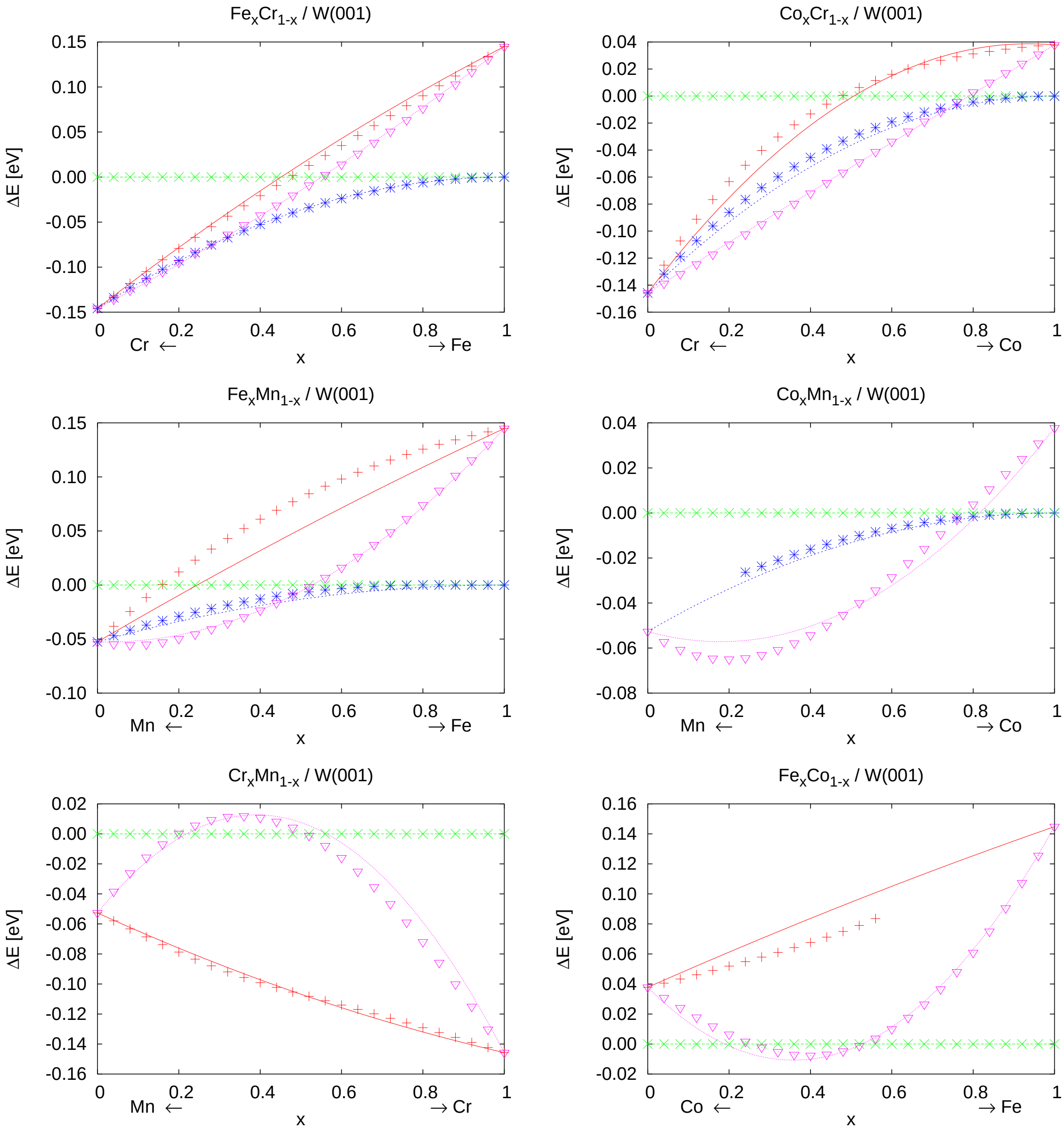

Figure 16: *Total energy differences ΔE of various magnetic states with respect to the DLM state that have been calculated from Eq. (133) are compared to the corresponding energy differences previously obtained from DFT calculations. Individual symbols denote the DFT results—these symbols form the same graphs as in the corresponding panels of Fig. 12 and Fig. 13—while lines represent the values derived from our Ising-like model, i.e. from Eq. (133). The values of the parameters J_{XX}, J_{XY}, J_{YY} that were substituted into the right-hand side of Eq. (133) are listed in Tab. 5.*

J_{XX}, J_{YY}	J_{XY}
	$J_{\mathrm{CrMn}} = -0.229$ eV
$J_{\mathrm{CrCr}} = -0.292$ eV	$J_{\mathrm{FeCr}} = +0.058$ eV
$J_{\mathrm{MnMn}} = -0.105$ eV	$J_{\mathrm{FeMn}} = +0.115$ eV
$J_{\mathrm{FeFe}} = +0.290$ eV	$J_{\mathrm{CoCr}} = +0.103$ eV
$J_{\mathrm{CoCo}} = +0.076$ eV	$J_{\mathrm{CoMn}} = +0.156$ eV
	$J_{\mathrm{FeCo}} = +0.195$ eV

Table 5: *Estimated values of the parameters J_{XX}, J_{YY}, and J_{XY} that describe the interaction between local magnetic moments of two atoms in the surface alloy. The values were chosen so that the DFT results for the total energy be exactly reproduced for all chemically pure monolayers in both the FM and the DLM state and also for the $Fe_{0.5}Cr_{0.5}$, $Co_{0.5}Cr_{0.5}$, $Fe_{0.5}Mn_{0.5}$, $Co_{0.5}Mn_{0.5}$, and $Fe_{0.5}Co_{0.5}$ surface alloys in the APM state and for $Cr_{0.5}Mn_{0.5}$ in the FM state.*

plotted in the respective graphs of Fig. 12 and Fig. 13 for vanadium alloys obviously cannot be approximated by any quadratic function. Nevertheless, our model may still represent reasonably well magnetic properties of the other surface alloys, those which contain elements characterized by more rigid magnetic moments than vanadium has, i.e. the alloys composed of Cr, Mn, Fe, and Co.

So let us compare the prediction of Eq. (133) concerning ΔE as a function of x for the $\mathrm{Fe}_x\mathrm{Cr}_{1-x}$, $\mathrm{Co}_x\mathrm{Cr}_{1-x}$, $\mathrm{Fe}_x\mathrm{Mn}_{1-x}$, $\mathrm{Co}_x\mathrm{Mn}_{1-x}$, $\mathrm{Cr}_x\mathrm{Mn}_{1-x}$, and $\mathrm{Fe}_x\mathrm{Co}_{1-x}$ alloys with the corresponding results of DFT calculations presented in Figs. 12 and 13. The comparison is shown in Figs. 16. To draw the curves corresponding to Eq. (133), the parameters J_{XX}, J_{YY}, and J_{XY} for all relevant elements X and Y had to be determined. The values of the parameters should be chosen so that they render, in some sense, the best fit of the expression on the right-hand side of Eq. (133) to the results found by the DFT calculations. However, the purpose I had in mind when I introduced the Ising-like model, which lead to Eq. (133), was just that it should help to reveal some overall trends, not that it should provide a precise quantitative description. There is therefore no need to invent some sophisticated way to find the best possible fit. Instead, I have determined the values of J_{XX}, J_{YY}, and J_{XY} by simply imposing the requirement that the value of ΔE derived from the model must exactly agree with the value comming from the DFT calculations in several selected cases. These cases were the following: First, it was the FM state of each chemically pure overlayer, i.e. of pure Cr, Mn, Fe, and Co layer. Next, it was either the FM or the APM state of a binary alloy that contained an equal amount of both its components. The FM state was chosen for $\mathrm{Cr}_{0.5}\mathrm{Mn}_{0.5}$ and the APM state was chosen for all the others, i.e. for $\mathrm{Fe}_{0.5}\mathrm{Cr}_{0.5}$, $\mathrm{Co}_{0.5}\mathrm{Cr}_{0.5}$, $\mathrm{Fe}_{0.5}\mathrm{Mn}_{0.5}$, $\mathrm{Co}_{0.5}\mathrm{Mn}_{0.5}$, and $\mathrm{Fe}_{0.5}\mathrm{Co}_{0.5}$, thus taking always that one of the two states, FM or APM, which had lower energy and which should be therefore closer to the ground state. The energies of the DLM states were always used as the zero level. The values of the parameters J_{XX}, J_{YY}, and J_{XY} thus obtained are listed in Tab. 5.

Having tested the analytical model description in the case of the special magnetic states, we eventually get to the partially polarized (uncompensated DLM) magnetic

composition	**model prediction**		**DFT results**	
$\mathrm{X}_x\mathrm{Y}_{1-x}$	p_X	p_Y	p_X	p_Y
$\mathrm{Fe}_{0.25}\mathrm{Cr}_{0.75}$	-0.60	$+1.00$	-0.5	$+1.0$
$\mathrm{Fe}_{0.50}\mathrm{Cr}_{0.50}$	-0.20	$+1.00$	-0.2	$+1.0$
$\mathrm{Fe}_{0.75}\mathrm{Cr}_{0.25}$	-0.07	$+1.00$	-0.1	$+1.0$
$\mathrm{Co}_{0.25}\mathrm{Cr}_{0.75}$	-1.00	$+1.00$	-1.0	$+1.0$
$\mathrm{Co}_{0.50}\mathrm{Cr}_{0.50}$	-1.00	$+1.00$	-1.0	$+1.0$
$\mathrm{Co}_{0.75}\mathrm{Cr}_{0.25}$	-0.45	$+1.00$	-0.5	$+1.0$
$\mathrm{Fe}_{0.25}\mathrm{Mn}_{0.75}$	-1.00	$+1.00$	-0.1	$+1.0$
$\mathrm{Fe}_{0.50}\mathrm{Mn}_{0.50}$	-0.40	$+1.00$	-0.5	$+1.0$
$\mathrm{Fe}_{0.75}\mathrm{Mn}_{0.25}$	-0.13	$+1.00$	-0.2	$+1.0$
$\mathrm{Co}_{0.25}\mathrm{Mn}_{0.75}$	-1.00	$+1.00$	-1.0	$+1.0$
$\mathrm{Co}_{0.50}\mathrm{Mn}_{0.50}$	-1.00	$+1.00$	-1.0	$+1.0$
$\mathrm{Co}_{0.75}\mathrm{Mn}_{0.25}$	-0.68	$+1.00$	-0.6	$+1.0$

Table 6: *The general partially polarized (uncompensated DLM) magnetic states with the lowest energy have been determined for several overlayers of different composition. The minimal-energy states are characterized by the parameters* p_X *and* p_Y *defined by Eqs. (128). The values of* p_X *and* p_Y *that were determined by minimizing the right-hand side of Eq. (133) under the constraints* $0 \leq p_X \leq 1$ *and* $0 \leq p_Y \leq 1$ *are compared to those obtained independently from the DFT calculations.*

states, which are characterized by arbitrary values of p_X and p_Y ranging from -1 to 1. A comparison between the Ising-like model, expressed by Eq. (133), and the DFT results is made in Tab. 6. The magnetic states in which the surface system reaches its minimal energy were independently determined using both approaches. The values of p_X and p_Y that were found by minimizing the analytical expression for ΔE, as given by the right-hand side of Eq. (133), differed from the corresponding values determined by direct DFT calculations by 0.1 at most. Again, the values of J_{XX}, J_{XY}, and J_{YY} listed in Tab. 5 were substituted into Eq. (133) for the purpose of this comparison. Just a few (namely 12, as the reader sees in Tab. 6) surface alloys of various composition were selected to perform the comparison. The reason is that carrying out the corresponding DFT calculations was rather demanding. The magnetic states considered here form a two-dimensional continuum that can be parameterized with p_X and p_Y. The continuum of the magnetic states was sampled by changing the parameters from -1.0 to 1.0 with the step of 0.1. Such a sampling adds up to $21 \times 21 = 441$ magnetic configurations for any particular composition of the surface alloy; this number can be reduced down to 221 if the symmetry with respect to the simultaneous sign change of p_X and p_Y is taken into account. The alloys selected for the test are those in which one of the components tends to the ferromagnetic and the other one to the antiferromagnetic coupling and in which both components have rather rigid magnitudes of their respective magnetic moments. This criteria limit the combination of the chemical elements in the overlayer to FeCr, FeMn, CoCr, and CoMn. Three cases of different composition have been explored for each pair of elements, namely $\mathrm{X}_{0.25}\mathrm{Y}_{0.75}$, $\mathrm{X}_{0.50}\mathrm{Y}_{0.50}$, and $\mathrm{X}_{0.75}\mathrm{Y}_{0.25}$.

Actually, the uncompensated DLM states have been explored in the case of chemically pure overlayers too. The task was much less demanding with the pure overlayers since the energy depended on one polarization parameter p only. These calculations lead to the expected result that either the FM (for V, Cr, and Mn) or the DLM (for Fe and Co) state of the chemically pure layers possess the lowest total energy of all the investigated magnetic states.

The surface alloys containing vanadium, however, do not conform to Eq. (133), because of the already discussed sensitivity of vanadium magnetic moments to the chemical and magnetic properties of the atomic neighborhood. Due to this sensitivity, there are many partially polarized magnetic states for which no DFT solution can be found. That is why the surface alloys containing vanadium are not included in Tab. 6. Moreover, among those magnetic states of FeV and CoV that *can* be handled with a DFT calculation, one of the formerly considered special states always turns out to be the state with the lowest energy. The lowest-energy state of an FeV or a CoV alloy is thus always either the DLM+FM or APM state or the DLM+NM state, just as suggested by the panels Fig. 12(a) and Fig. 12(b).

The magnetic configurations explored in this thesis were mainly limited to those that could be described within the CPA using a $p(1 \times 1)$ surface unit cell. The lowest energy states found here are therefore not necessarily the real ground state that would realize in nature. However, the calculations, although carried out in a limited space of magnetic configuration, reveal important characteristics of the magnetic interactions that take place in the surface alloys. The characteristics found in this way (expressed, e.g., by the coefficients J_{XY}, J_{XY}, J_{YY}) can be later inserted into models of more complicated magnetic structures that would be too difficult to treat with first-principles calculations. The rather good agreement between the DFT results and the prediction of our Ising-like model for the overlayers containing Fe, Cr, Mn and Co suggests that such models based on pair-wise magnetic interaction would be indeed useful to study some more complicated magnetic structures in these systems.

4.2 Incomplete coverage of the tungsten surface

4.2.1 Disordered submonolayer films

Apart from the possibility of treating binary alloys, the LMTO-ASA method combined with the CPA also provide means of treating disordered layers of a submonoatomic thickness. An incomplete (sub-monoatomic) overlayer can be represented by a two-dimensional surface alloy, one of whose components consists of empty atomic spheres (like those representing the vacuum above the surface). This possibility will be used to explore the magnetic properties of incomplete overlayers formed of a $3d$ transition metal on the W(001) surface. The clean W(001) surface is known to undergo a reconstruction into a $c(2 \times 2)$ surface structure at low temperatures [68, 70], but Spišák and Hafner [62] have shown that this reconstruction disappears when iron is adsorbed on the surface. Even at very low coverage, the reconstructed tungsten surface reverts locally to an almost unreconstructed structure under individual iron atoms. I will assume that a similar de-reconstruction takes place after adsorption of other $3d$ metals as well. The absence of surface reconstruction allows me to retain the idealized surface structure depicted in Fig. 11, which was adopted in the previous calculations for surface binary alloys. Furthermore, it will be assumed that all available surface sites have the same probability of being occupied by an adsorbed atom of the $3d$ transition element in question. Then the probability that a surface site is occupied by an adsorbed atom may be interpreted as fractional coverage of the surface by the overlayer. This occupational probability or the surface coverage will be denoted by the symbol θ in the following. To sum up, the incomplete overlayer will be formally described as a two-dimensional homogeneous binary alloy, just like those in the previous section, but the second component of the alloys will always be the vacuum. Admittedly, real incomplete overlayers (which may be encountered, e.g., during the deposition of the monolayers) can be expected to display a more complex structure due to the formation of islands, clusters, ordered phase domains etc. However, I will focus on the general trends resulting from the lowered surface coverage and reduced average number of atomic neighbors surrounding a typical surface atom rather than exploring the effects of the the actual surface structure. In fact, we will see that the most prominent phenomenon exhibited by the incomplete overlayers, namely the reduction of the magnetic moment predicted for some of the $3d$ transition elements at low coverages, is primarily determined by the overall coverage while it is less dependent on the detailed structure of the surface layer.

Figs. 17 and 18 show how the properties of the partially covered surface depend on the coverage θ. Fig. 17 shows differences between the respective total energies of the ferromagnetic, DLM, and non-magnetic[5] (NM) states. The energies presented in Fig. 17 are expressed as the amount of energy per occupied surface site, that means per one adatom, rather than as the amount of energy per any surface site. The total energy per one (any) surface site has to be divided by θ to obtain the total energy per one adatom. The latter representation of total energies allows one to see the energy differences between different magnetic configurations clearly even if the coverage is very low. In contrast, the differences of the energy per one surface site inevitably tend to zero when going to very low coverages, because the clean tungsten surface is non-magnetic. The energy of the non-magnetic state is chosen as a zero energy level here. In the previous section, which dealt with the full monoatomic layers of binary alloys on the tungsten surface, the non-magnetic states were not discussed at all. The reason for their omission was that their energy considerably exceeded the energies of all the various magnetic states. The NM state of the complete overlayers was thus highly unfavorable in terms of total energy. However, this is no longer true as we start looking at the partially covered surfaces. Fig. 17 reveals that the non-magnetic state turns out to be the preferred one for vanadium, chromium and manganese films at low coverage, namely for coverage below $\theta \approx 0.65$ for V, below $\theta \approx 0.50$ for Cr, and below $\theta \approx 0.10$ for Mn. Correspondingly, the magnetic moments

---

[5] What I mean by the 'non-magnetic' state here is a state in which the local magnetic moments of all atoms are zero. This state is sometimes referred to as 'paramagnetic', however, the DLM state may be considered paramagnetic as well, so I will stick to the term 'non-magnetic' to avoid ambiguity.

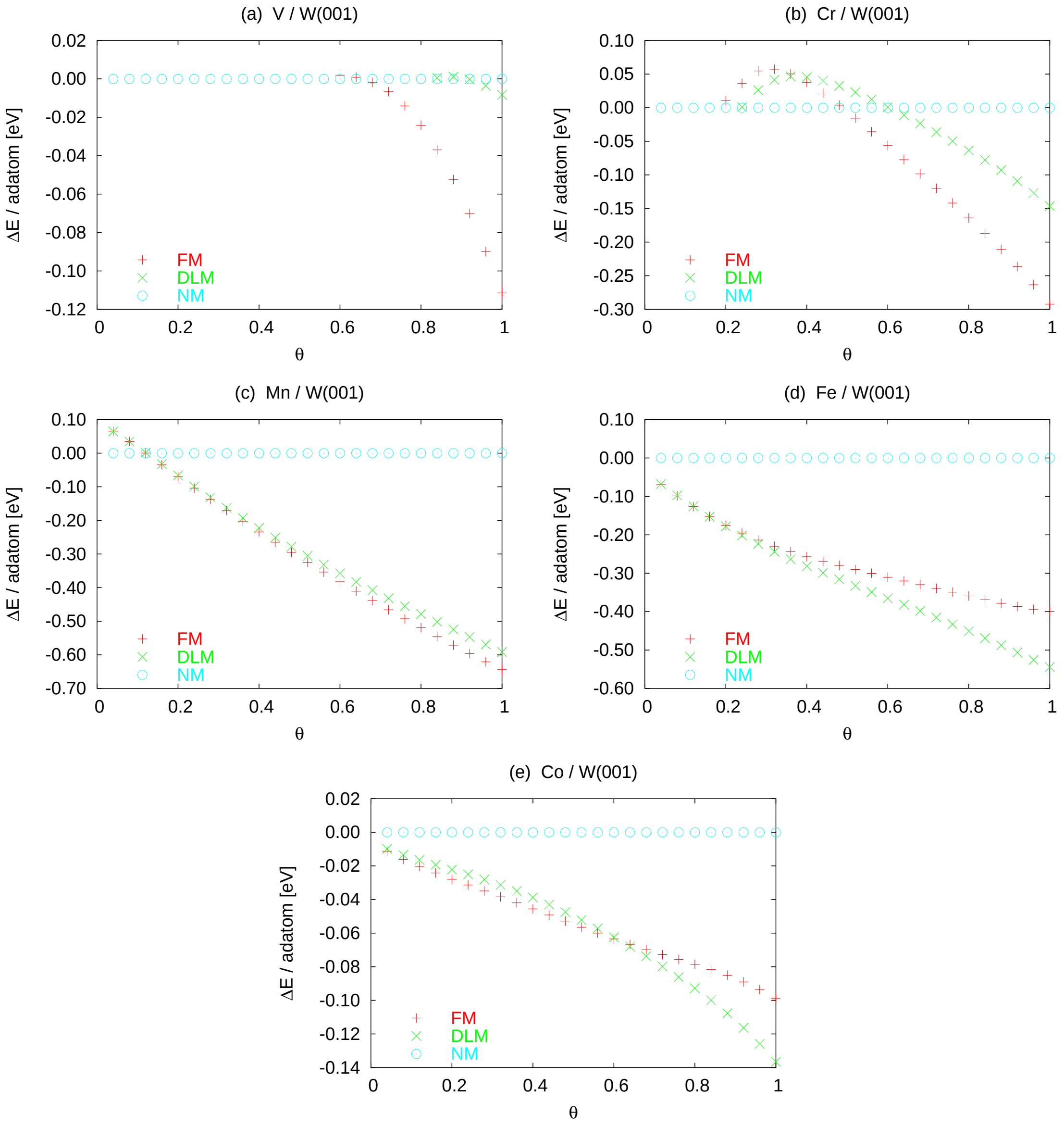

Figure 17: *Total energies of the ferromagnetic (FM, denoted by red upright crosses) and DLM (denoted by green diagonal crosses) states of (a) vanadium, (b) chromium, (c) manganese, (d) iron, and (e) cobalt layers on the W(001) surface as a function of surface coverage* θ. *The energies are rendered as differences from the energy of the corresponding non-magnetic state, which thus serves as the zero energy level. The total energies are represented by their values per one adatom, i.e., per occupied surface site.*

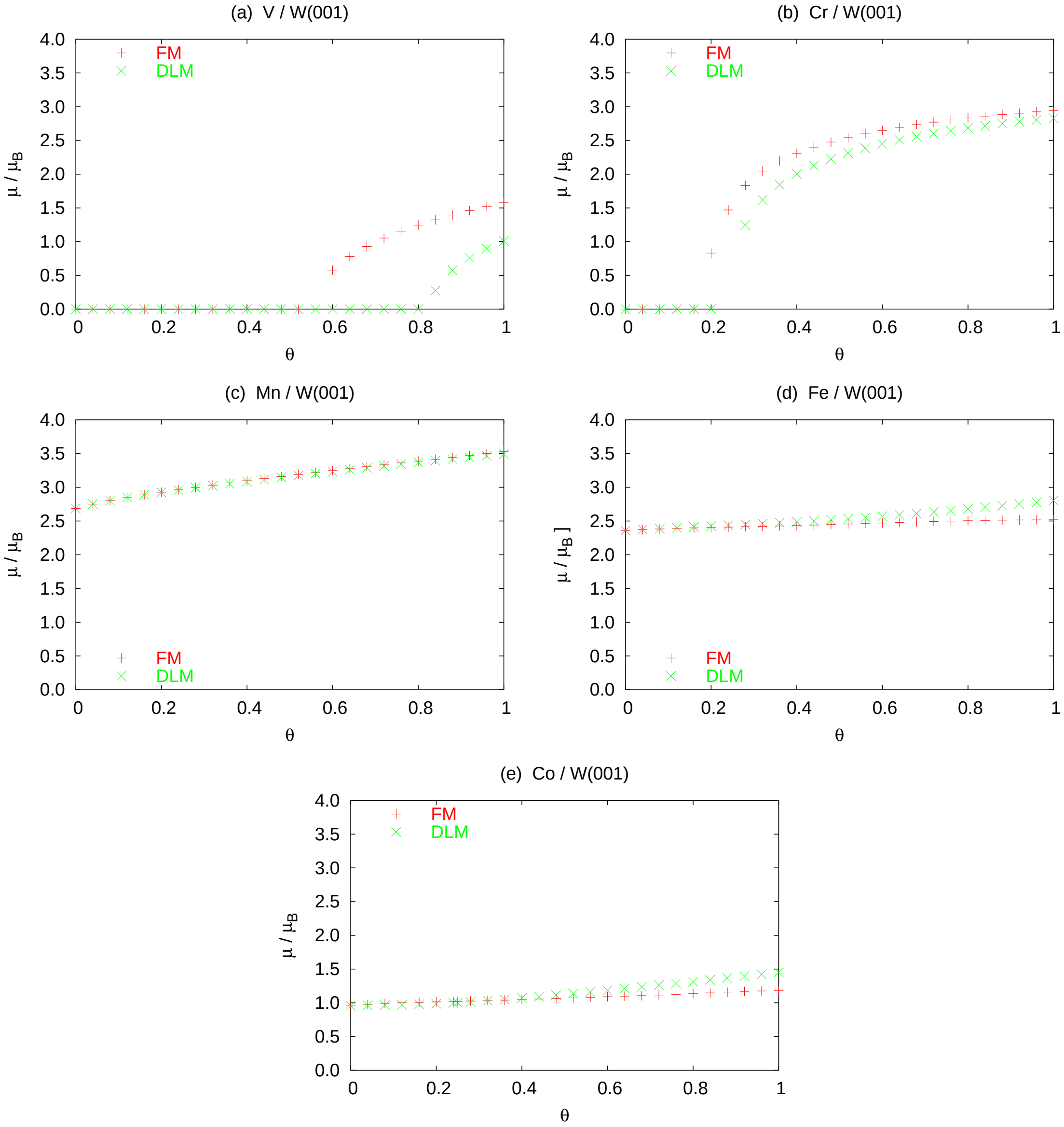

Figure 18: *Local magnetic moments at atoms of the incomplete overlayers in the FM (upright crosses) and DLM (diagonal crosses) states as a function of the surface coverage.*

of adsorbate atoms—i.e. of V, Cr, Mn, Fe, and Co (shown in Fig. 18)—decrease with decreasing coverage. This trend is especially pronounced in the cases of vanadium and chromium, for which no DFT solution with non-zero magnetic moments exists at all if the coverage is too low. Interestingly, the changes of the atomic magnetic moments exhibited by manganese are substantially smaller in comparison to the changes observed for vanadium and chromium, and magnetic solutions exist for the manganese overlayer at arbitrarily low coverage, although the non-magnetic state is the one with the lowest energy for very thin manganese layers.

The non-magnetic ground state of vanadium, chromium and manganese submonolayer films may seem surprising. The magnetic moments of atoms adsorbed on surfaces are usually enhanced in comparison with the magnetic moments of the same atoms in bulk materials [69]. The enhancement is due to the reduced coordination number (the number of nearest neighbors) of surface atoms with respect to the bulk atoms. Therefore it seems reasonable to expect even more enhancement of the magnetic moments with further reduction of the average coordination number at lower than monoatomic coverage. However, this is apparently not what the self-consistent DFT calculations predict for V, Cr, and Mn on W(001). The argument that links the tendency to spontaneous generation of magnetic moments with the coordination number is too simplistic to hold generally. There are two basic assumptions on which this argument relies. The first assumption is that the tendency to spontaneous magnetization or the absence thereof is decided by the Stoner criterion [71]. In brief, the Stoner criterion says that the ferromagnetic state of a given system will be preferred if the density of states at the Fermi level is sufficiently high for the corresponding non-magnetic system, namely

$$I \cdot n(E_F) > 1 \tag{134}$$

where $n(E_F)$ is the density of states at the Fermi energy and the exchange-correlation integral or so called Stoner parameter I plays the role of a proportionality constant that relates the splitting of energy bands caused by the spin-dependent part of the exchange-correlation potential to the magnetic moment of atoms. The density of states has to be replaced by the local (surface-projected) density of states when applying the criterion on a two-dimensional system (surface). Considering that the d-electrons of the $3d$ transition metals are especially relevant to the magnetism of the surface systems investigated in this thesis, the Stoner parameter can be estimated from the calculated magnetic moment per adatom and from the splitting observed at these adatoms between the centers of the $3d$ electron bands pertaining to different spin orientations:

$$I = \frac{\Delta\epsilon_d}{\mu}, \tag{135}$$

where μ is the magnetic moment of an atom of a $3d$ transition metal expressed in the Bohr magnetons and $\Delta\epsilon_d$ is the $3d$-band splitting. The band splitting can be easily extracted from the results of the LMTO calculation as $\Delta\epsilon_d = C_{3d}^{\uparrow} - C_{3d}^{\downarrow}$, since the parameters C, which denote the centers of the respective spin-resolved energy bands, appear directly in the linearization formula of the LMTO method, Eq. 86. Let us focus on the DFT calculations carried out for the ferromagnetic state of the overlayers, so as to arrive at an estimate for the Stoner parameter. The numerical

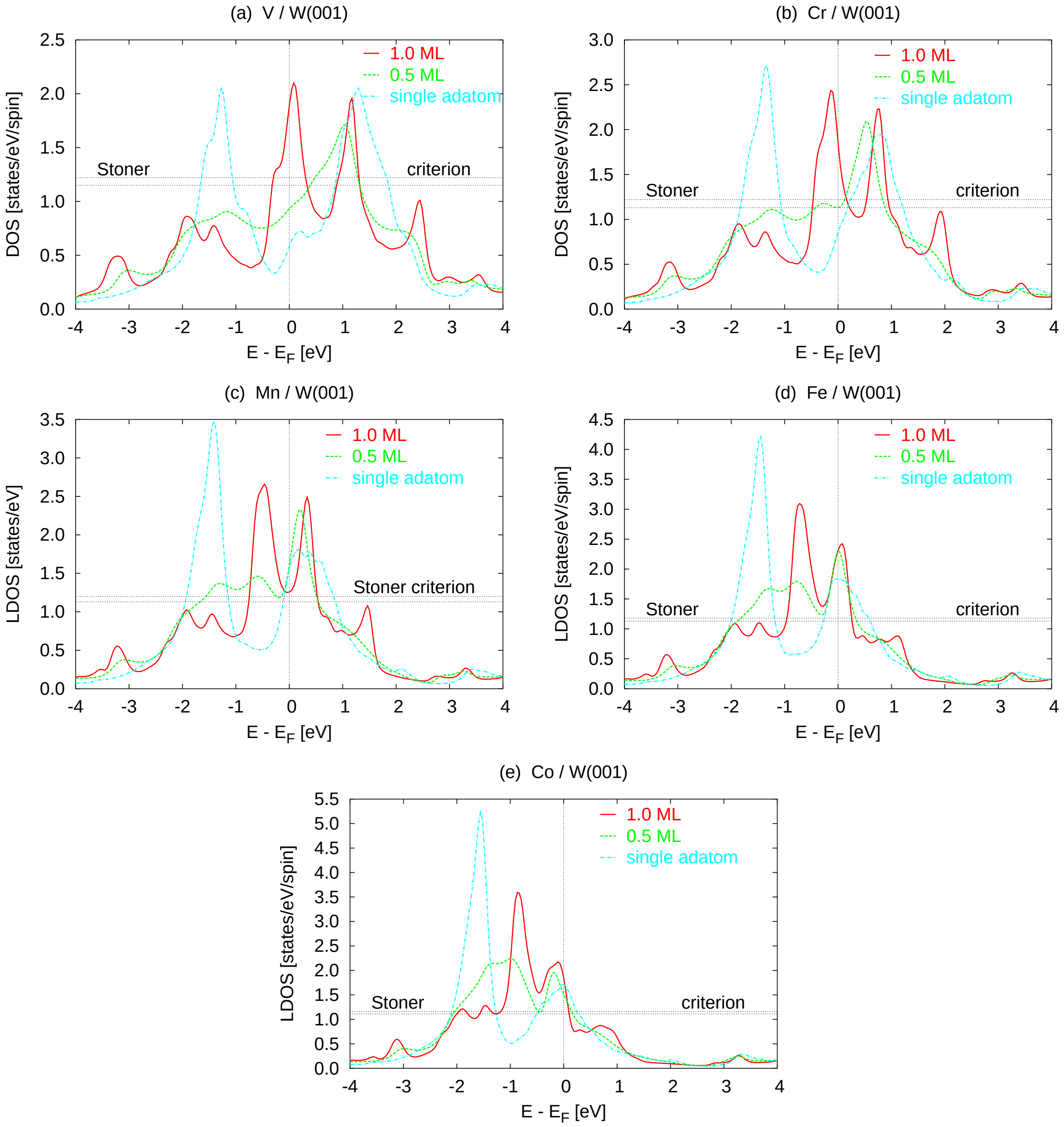

Figure 19: *Non-magnetic density of states around the Fermi level projected onto the adatoms is shown for (a) vanadium, (b) chromium, (c) manganese, (d) iron, and (e) cobalt overlayers on W(001), each for three different levels of coverage: full monolayer ($\theta = 1.0$, full red line), half a monolayer ($\theta = 0.5$, dashed green line), and the limit of zero coverage, i.e. a single isolated adatom ($\theta = 0.0$, dash-dotted light blue line). The double horizontal lines denote the threshold density of states pertaining to the the Stoner criterion (upper and lower estimate of the reciprocal Stoner parameter I^{-1}).*

values of the Stoner parameter I we thus obtain ranges from 0.81 eV to 0.91 eV (cf. the values of I found for bulk materials in [72]). This value is not particularly sensitive to the level of coverage or to the chemical nature of the adatoms, indicating that I is indeed a well-defined parameter. Of course, if the Stoner criterion indicates that ferromagnetism is preferred over the non-magnetic state, it does not mean that the ferromagnetic state must be the ground state, since other magnetic states (like DLM, antiferromagnetism, etc.) cannot be excluded. Note, however, that the energy of the non-magnetic state often differs from the energies of all the various magnetic states with non-zero local magnetic moments much more than the energies of these magnetic states differ from each other. Consequently, the satisfied Stoner criterion may be still taken as an indication that some state characterized by non-zero local magnetic moments is indeed the ground state, although it is not necessarily the ferromagnetic one. The second assumption on which the supposed relation between the coordination number and magnetism relies is that the width of the electron bands increases with increasing coordination number of atoms constituting the system; hence a reduction of the density of states with increasing coordination number. The other way round, the density of states increases when the coordination number is reduced, making the ferromagnetic state more favorable.

Fig. 19 shows that the simplistic consideration regarding the link between the coordination number of surface atoms and their magnetic moments fails on the grounds of both its fundamental assumptions. Neither does the fulfillment of the Stoner criterion guarantee that the system will be magnetic, as demonstrated by the case of very thin manganese overlayers—see panel (c) of Fig. 19—nor does the (surface-projected) density of electron states at the Fermi level necessarily increase with the reduction of the coordination number—in fact, the opposite is true for most cases shown in Fig. 19. The Stoner criterion may be a good indication of ferromagnetism in simple bulk materials; however, a simple generalization of such a rule of thumb is not possible for the more complex surface systems. The *ab-initio* DFT treatment is thus absolutely indispensable so as to arrive at any meaningful predictions regarding the magnetic properties of these surface systems.

4.2.2 Ordered half-a-monolayer-thick Cr film

In order to make the conclusion about the non-magnetic ground state of ultra-thin films on W(001) more reliable, a calculation for one selected system, namely Cr on W(001) at 50 % coverage, has been carried out using the FP-(L)APW method in the implementation of the WIEN2k computer code [37]. The calculation was aimed at finding the dependence of the total energy on the magnetic moment in a ferromagnetic state of the system. So as to explore this dependence, a constraint was imposed on the total spin moment[6] during the DFT calculation. The search for the electron distribution that minimized the energy functional was thus restricted by the condition that the number of the spin-up and the number of the spin-down electrons differed by a predetermined value. The calculation with a fixed spin moment was

---

[6] The orbital magnetic moment was always zero because the spin-orbit coupling was not considered.

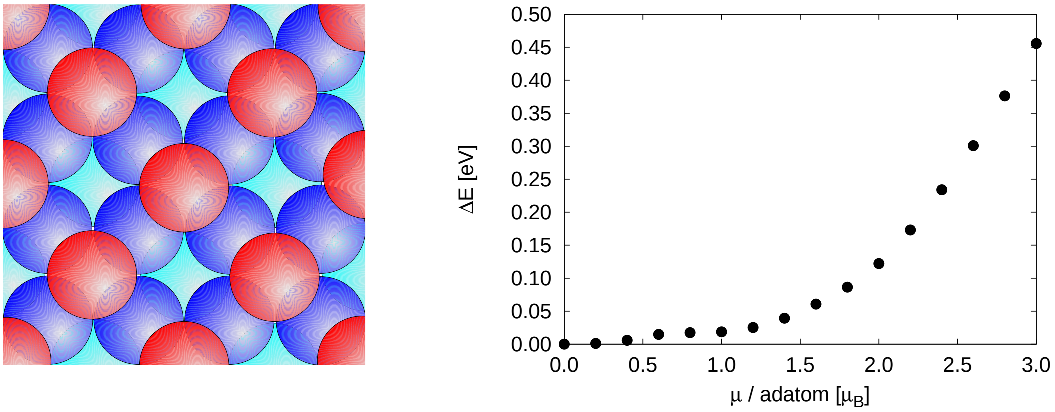

Figure 20: *On the left: Top view of the 0.5 monolayer of chromium arranged on the tungsten (001) substrate in the form of the* $c(2 \times 2)$ *superstructure. Red spheres represent the Cr atoms, blue spheres the W atoms. On the right: Total energy of the* $c(2 \times 2)$*–Cr/W(001) system as a function of the total magnetic moment per one Cr atom. The energy of the non-magnetic system is chosen as the zero energy level.*

repeated for several different magnitudes of the magnetic moment. The comparison of total energies found for different magnetic moments allows us to check whether the functional for the total energy is really minimal for the zero magnetic moment. This is an advantage over the previous calculations, which could not definitely exclude the possibility that the energy minimum at the zero magnetic moment was just a local minimum that had been accidently reached by the iterative DFT calculation instead of being the genuine ground state.

Since the WIEN2k code can only deal with periodic structures, the calculation was performed on a repeated slab and the chromium atoms on the tungsten surface were assumed to form a $c(2 \times 2)$ regular pattern (see the left panel of Fig. 20). The slab consisted of 9 atomic layers of the bcc tungsten and the $c(2 \times 2)$–Cr superstructure on both its surfaces. About 1 nm wide empty space was left between the neighboring slabs to ensure that the slabs do not influence each other. The spacing between the tungsten atomic layers in the slab was kept at its bulk value while the distance between the chromium overlayer and the underlying tungsten layer was reduced by 14.4 %, i.e. to 85.6 % of the tungsten interlayer distance. This position of the Cr overlayer on the tungsten substrate was taken from [46], although it had been determined there for a full monoatomic layer of chromium rather than for one half of a monolayer. The surface Brillouin zone was sampled by 15×15 $\vec{k}$-points, which resulted in having 36 $\vec{k}$-points in the irreducible wedge of the Brillouin zone. The size of the (L)APW basis set was limited by the plane wave cutoff $K_{max} = 60.1\ \text{nm}^{-1} = 3.18\ \text{a.u.}^{-1}$, corresponding to the maximal kinetic energy of 10.1 Ry. The augmentation part of the plane waves was constructed according to the APW+lo scheme for $l \leq 2$ (corresponding to the s, p, and d orbitals) in the atomic spheres of Cr and for $l \leq 3$ (corresponding to the s, p, d, and f orbitals) in the atomic spheres of W. The LAPW scheme was applied to all higher angular numbers l. Spherical harmonics up to $l = 10$ were considered. The $3p$ electronic states of Cr atoms and $5p$ and $4f$ states of W atoms were treated as semi-core states, while all the lower lying states were treated as parts of the atomic core. The GGA representation of the exchange-correlation potential due to Perdew, Burke, and Ernzerhof [38] was employed. The self-consistency of the DFT solution was considered to be reached when the 'distance'[7] between electron-density distributions in two consecutive iterations was less than 10^{-4} electrons per unit cell. The total energy per unit cell differed by about 1 meV or less between two consecutive iterations upon satisfying the condition for a self-consistent electron distribution. The preset value of the magnetic moment per surface unit cell was maintained throughout the iterations of the DFT calculation by adjusting the Fermi level for spin-up electrons and spin-down electons independently.

The dependence of the total energy per surface unit cell on the total magnetic moment per one Cr adatom (which equals half the magnetic moment per one surface unit cell) is shown in the right panel of Fig. 20 for the investigated system $c(2 \times 2)-$Cr/W(001). As expected, we find that the non-magnetic state is the one with the lowest energy. The ordered $c(2 \times 2)$ surface structure of the Cr adatoms is of course a different system from the completely disordered chromium overlayers which were investigated using the LMTO-ASA method. Since the non-magnetic state turns out to be the ground state of the $c(2 \times 2)-$Cr overlayer as well as of the disordered Cr overlayers thinner than 0.5 monolayer, we may conclude that the chromium-covered W(001) surface is non-magnetic at a sufficiently low coverage regardless of the details of how the Cr atoms are arranged on the surface.

Now, let me return to the question of surface relaxation of the $c(2 \times 2)$ chromium layer on W(001). The distance between the chromium overlayer and the underlying tungsten substrate was set to a value that had been actually found for a Cr monolayer rather than half a monolayer. The fixed-spin calculations were too time consuming to search for the equilibrium positions of the Cr atoms in these calculations. The calculated force that acted on the Cr atoms in the non-magnetic state had a magnitude of 47.3 eV/nm (i.e. 7.57×10^{-9} N) and was directed towards the tungsten substrate, so the Cr overlayer would tend to relax inwards with respect to the position in which it was fixed. It will be shown in the next section of this thesis (chapter 4.3) that the magnetic moments of the $3d$ transition metals adsorbed on the W(001) surface invariably decrease as the adsorbate atoms come closer to the substrate. We can thus reasonably expect that the inward relaxation does not change the non-magnetic ground state.

4.3 Effects of surface layer relaxation

Because of the surface relaxation, the distances between atomic layers near the surface differ from the interlayer spacing inside the bulk. The effects originating from

---

[7] The distance between two different electron distributions is defined here as the Euclidean distance between the said distributions viewed as multi-component vectors, each vector component standing for the electron density at one particular point of the physical three-dimensional space.

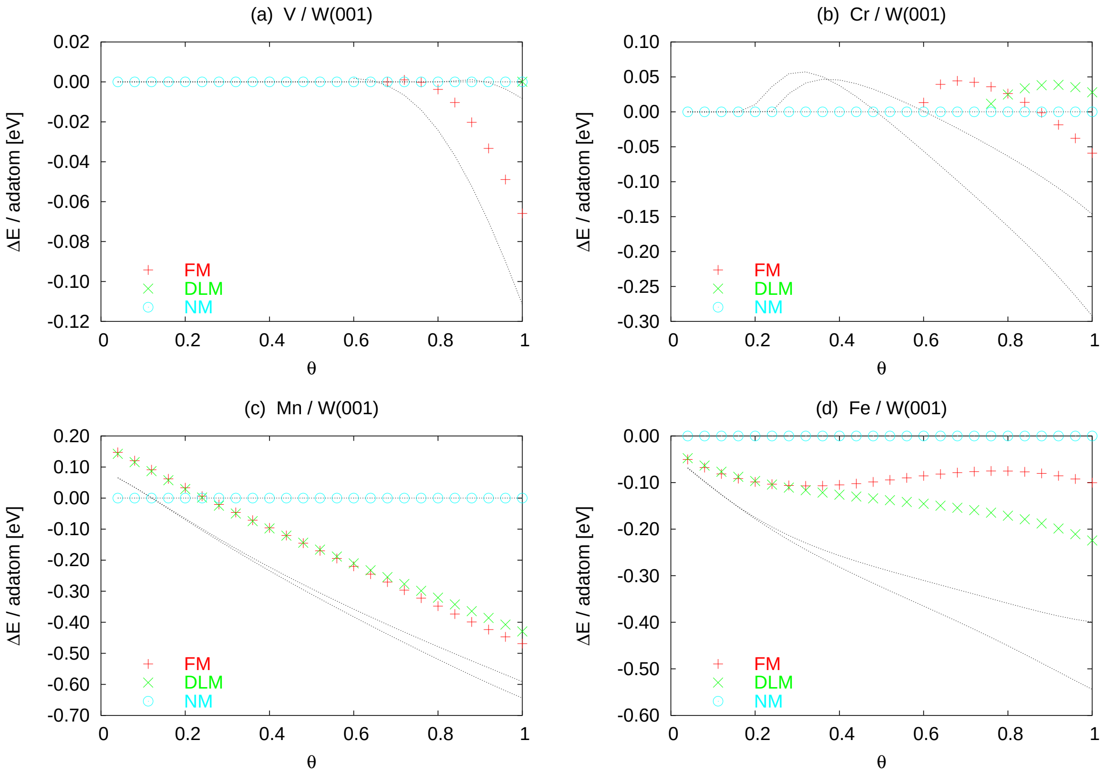

Figure 21: *Differences between the total energies of various magnetic states as a function of surface coverage. Results for the relaxed submonolayer films of (a) vanadium, (b) chromium, (c) manganese, and (d) iron are presented here. The corresponding graphs obtained for the unrelaxed systems at submonolayer coverage, which can be seen in Fig. 17 are shown here for comparison as black dotted curves.*

the surface layer relaxation have been neglected so far. All calculations regarding the disordered surfaces that have been discussed until now involved an ideal surface structure, in which not only the distance between neighboring tungsten layers near the surface but also the distance between the overlayer and the tungsten substrate equaled the interlayer distance in bulk tungsten, i.e. half of the bcc tungsten lattice parameter. However, the calculations carried out by Ferriani et al. [46] for the pure (one-component) $3d$ metal layers on W(001) reveal that an appreciable inward relaxation occurs for these overlayers. The inward relaxation amounts to 8.4 %, 14.4 %, 4.7 %, 13.7 %, and 22.1 % of the ideal W(001) interlayer spacing for V, Cr, Mn, Fe, and Co monolayers, respectively. Ferriani et al. did not publish the equilibrium distances between the underlying tungsten layers. In order to assess how important is the relaxation of these tungsten layers beneath the adsorbate, I have repeated the geometry optimization for the complete chemically pure monolayers on the W(001) surface using VASP (Vienna Ab-initio Simulation Package), software based on the *projector augmented wave* method (PAW) [73, 74]. For the purpose of these calculations, the systems of interest were represented by 11-layer symmetric slabs which consisted of 9 tungsten atomic layers and the monoatomic overlayer on both sides. The calculations have shown that the tungsten layers are shifted only slightly from

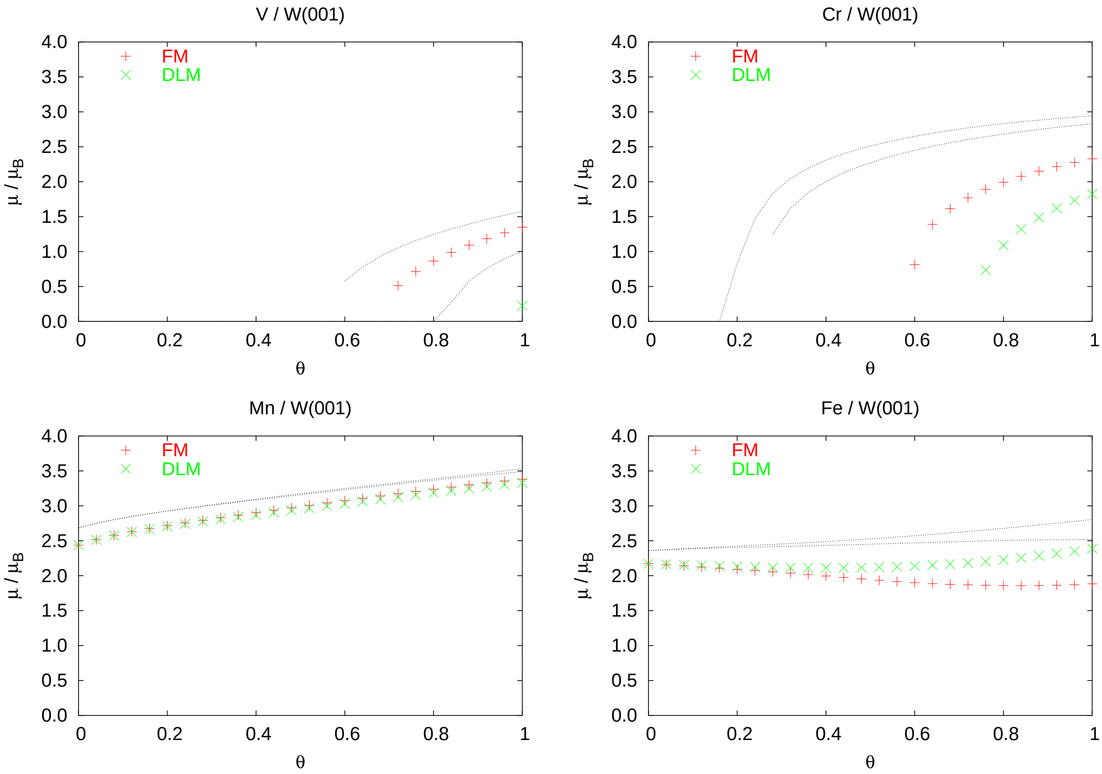

Figure 22: *Local magnetic moments at atoms of the 3d transition elements for the systems in the DLM state as a function of surface coverage. Results for the relaxed submonolayer films of (a) vanadium, (b) chromium, (c) manganese, and (d) iron are presented here. The corresponding graphs obtained for the unrelaxed systems at submonolayer coverage, which can be seen in Fig. 18, are shown here for comparison as black dotted curves.*

the ideal positions, by less than 2 % in the case of the top tungsten layer and by less than 1 % in the case of the deeper tungsten layers. Consequently, the ideal bcc bulk structure is a good approximation for the actual tungsten structure even near the surface. The only important change of the surface geometry is thus due to the relaxation of the topmost atomic layer, which consists of the adsorbed 3*d* transition metals.

The LMTO-ASA method is not suitable for performing a structure optimization, so I was not able to determine the relaxed structure of the disordered surfaces (the two-dimensional alloys and the incomplete films). I have to content myself with a mere estimate of the effects brought about by the surface relaxation. To carry out this estimate, some of the earlier calculations were repeated with an arbitrarily reduced distance between the overlayer and the top tungsten layer. The ideal bcc structure of the tungsten substrate was preserved. The arrangement of the empty atomic spheres that represented the vacuum above the surface was kept unchanged too. As the distance between the adsorbate layer and the topmost tungsten layer was altered, the radii of the atomic spheres adjacent to the surface had to be modified accordingly. The determination of the new radii relied upon the concept of

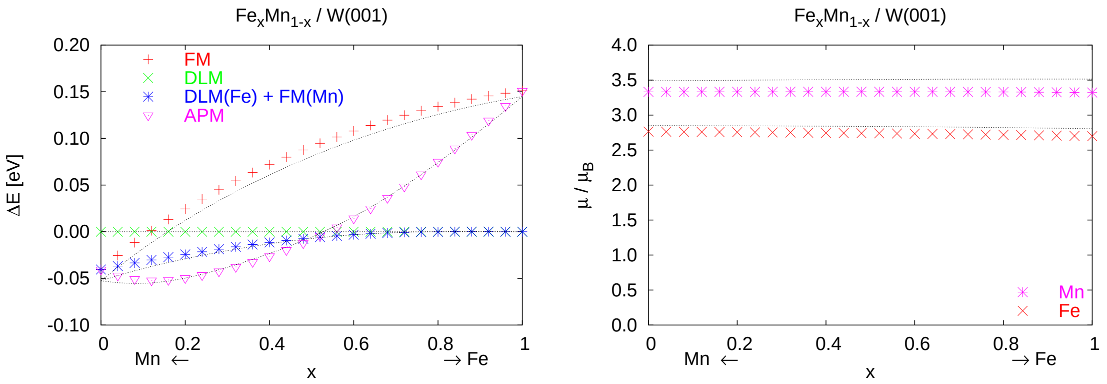

Figure 23: *Differences between the total energies of various magnetic states (left panel, symbols) and the local magnetic moments at Fe (red diagonal crosses) and Mn (purple asterisks) atoms in the DLM state (right panel) for the relaxed FeMn overlayers. The corresponding graphs obtained for the unrelaxed FeMn layers, which can be seen in Fig. 12(e) and Fig. 14(e), are shown here for comparison as black dotted curves.*

unrelaxed	relaxed
$J_{\mathrm{MnMn}} = -0.105$ eV	$J_{\mathrm{MnMn}} = -0.081$ eV
$J_{\mathrm{FeMn}} = +0.115$ eV	$J_{\mathrm{FeMn}} = +0.144$ eV
$J_{\mathrm{FeFe}} = +0.290$ eV	$J_{\mathrm{FeFe}} = +0.302$ eV

Table 7: *The parameters J_{XX}, J_{YY}, and J_{XY}, which characterize the effect of interaction between the adatoms on the mutual orientation of their magnetic moments. Comparison between the values found for the unrelaxed and for the relaxed case is made here for the FeMn overlayer. The method how the relaxation was taken into account is described in the text. The values of the parameters were determined in the same way as those in Tab. 5.*

Wigner-Seitz cells. A Wigner-Seitz cell is a locus of points that are closer to a particular lattice point than to any other lattice point (the centers of atomic spheres assumed the role of the lattice points here). The radii of the atomic spheres were set so that each atomic sphere would have the same volume as the corresponding Wigner-Seitz cell. As far as the chemically pure films were concerned, I adopted the relaxation of the overlayer position found by Ferriani et al. and used it even at submonolayer coverage. Apart from the chemically pure overlayers, the effects of the inward relaxation is also shown for the FeMn overlayer, which represents here the monoatomic layers of the binary alloys. Again, the inward relaxation of 13.7 % was assumed at the pure Fe end of the composition range and the inward relaxation of 4.7 % at the pure Mn end. In between, the model relaxation of the FeMn layer scaled linearly with the composition.

The magnetic properties of systems with the inwards-shifted adsorbate layer are compared to those of the original systems having an ideal unrelaxed geometry. The comparison can be seen in Fig. 21 and Fig. 22 for the incomplete overlayers and in Fig. 23 and Tab. 7 for the FeMn surface alloy. Fig. 22 and the right panel of Fig. 23 clearly demonstrate that the magnetic moments of the surface atoms are systematically diminished by the inward relaxation. Alongside with the decrease of magnetic moments in the magnetic states, the non-magnetic state becomes more favorable in terms of total energy as compared to the unrelaxed case (see Fig. 21). Nevertheless, the main trends that can be spotted in the magnetic properties as they change with the chemical composition—like, e.g., the FM versus DLM preference—remain essentially unchanged by the surface relaxation. For instance, if we compare the relaxed and unrelaxed overlayers of the FeMn two-dimensional alloy in terms of the parameters J_{XY} introduced by Eqs. (132)—their numerical values are listed in Tab. 7—we find out that the surface relaxation changes the numerical value of the parameters (quite notably) but does not change their sign. The tendency of local magnetic moments to parallel or antiparallel alignment may thus become stronger or weaker after the relaxation is taken into account, but it remains the same in the qualitative sense. The Co films (or surface alloys containing cobalt) are a noteworthy exception to this observation. The cobalt atoms approach the tungsten surface closer than atoms of the other $3d$ transition elements discussed in this thesis: the Co monolayer was found to relax inwards by 22 % on W(001). As a consequence of the large inward relaxation, the TB-LMTO calculation for the relaxed systems containing cobalt always lead to a non-magnetic solution. However, such a large structural change as the 22 % surface relaxation of the Co layer on W(001) cannot be adequately handled within the TB-LMTO ASA method. The magnetic properties of the Co overlayers are very sensitive to the actual surface geometry and no definite prediction about these properties can be made until the surface geometry is precisely and reliably known. In contrast to the surface layers with cobalt, the magnetic properties of overlayers containing only Fe and Mn are influenced by the surface relaxation only little. The V and Cr atoms display a more pronounced reduction of their magnetic moments with the relaxation than Fe or Mn atoms do, but otherwise their behavior is also not fundamentally changed.

4.4 Magnetic anisotropy of the monolayers on W(001)

The sensitivity of the SP-STM to the local magnetic moments depends on the orientation of the magnetic moments with respect to the magnetization of the scanning probe. Owing to this fact, the SP-STM can help us determine the direction in which the magnetic moments of surface atoms are oriented. The orientation of the magnetic moments on the surface with respect to the surface plane is driven by the *magnetic anisotropy energy* (MAE). The MAE is also important from another point of view. According to the Mermin-Wagner theorem [75], ferromagnetism cannot occur in two-dimensional systems (including magnetic surfaces) that can be described by an isotropic Heisenberg model, except for the absolute zero temperature. This theorem conveys the importace of the surface magnetic anisotropy in the formation of ferromagnetic surfaces at finite temperatures. Knowing the value of the MAE is an essential prerequisite for an estimate of the Curie temperature of a ferromagnetic surface system.

I have calculated the MAE for the ferromagnetic monolayers of V, Cr and Mn on the W(001) surface. The magnetic anisotropy of the antiferromagnetic Fe/W(001) has been already determined by Kubetzka et al. [44]. They found that the preferred orientation of magnetic moments for Fe on W(001) is perpendicular to the surface plane. The magnetic anisotropy of the antiferromagnetic Co monolayer on W(001) would be difficult to evaluate reliably because of the large inward relaxation of the cobalt layer combined with a considerable dependence of its magnetic properties on this relaxation.

In order to find the MAE, calculations that account for the spin-orbit coupling have to be performed. The spin-orbit coupling and related effects are particularly sensitive to the shape of electron wave functions and to the energies of the single-electron states. Full-potential linearized augmented plane wave (FP-LAPW) calculations were performed so as to meet the requirement for a faithful representation of the electron density and single-electron wave functions. The WIEN2k [37] software package, which implements the FP-LAPW method, was employed to carry out these calculations. All three systems for which the MAE was calculated were represented by a symmetric repeated slab consisting of 11 atomic layers, 9 of which were tungsten layers and the other two represented the adsorbed $3d$ transition metal (V, Cr, or Mn), one atomic layer of the adsorbate being on each side of the slab. The distances between atomic layers in the slab were determined beforehand by an atomic force minimization without the spin-orbit coupling. The determination of the surface geometry was done by VASP (Vienna Ab-initio Simulation Package) using the projector augmented wave method [73, 74] with the GGA representation of the exchange-correlation potential.

The spin-orbit interaction was included in the FP-LAPW calculations by means of the second variational method. For each of the three chemically different systems, the total energy was calculated for two different orientations of the magnetization axis, one along the (001) crystallographic direction, i.e. perpendicular to the W(001) surface, and the other along the (100) direction, i.e. in the plane of the W(001) surface. The MAE per unit cell is then calculated as the difference of these two total energies. The unit cell contained two surface atoms (one for each side of the slab), so the MAE per surface atom is half of this difference. The GGA in the parameterization of Perdew, Burke, and Ernzerhof [38] was used as an approximation to the exchange-correlation potential. The set of basis functions consisted of augmented plane waves up to $K_{max} = 78.8\ \mathrm{nm}^{-1} = 4.17\ \mathrm{a.u.}^{-1}$, which corresponded to the maximal kinetic energy of 17.4 Ry. Spherical harmonics up to $l_{max} = 10$ were included in the expansion of the augmentation parts of the basis functions around the atomic positions. Spherical harmonics up to $l = 4$ were considered in the determination of the non-spherical part of the effective potential inside the atomic spheres and spherical harmonics up to the same maximal angular quantum number (l=4) were also included in the calculation of the spin-orbit interaction. Scalar-relativistic eigenfunctions corresponding to eigenenergies up to 48 eV (3.5 Ry) above the Fermi level were determined and this eigenfunctions served as a new basis in the second variational step. The surface Brillouin zone was sampled by 60×60 $\vec{k}$-points. This sampling amounted to 465 $\vec{k}$-points in the irreducible wedge of the Brillouin zone in the case of the perpendicular orientation of the magnetization axis and to 900

$\vec{k}$-points in the case of the in-plane orientation of the magnetization axis. In the latter case, the symmetry of the system was reduced with respect to the former case, hence the different irreducible wedges. The high numbers of the $\vec{k}$-points and the basis functions as compared to the former calculations without spin-orbit coupling were necessary to achieve reasonably converged results. The augmentation part of the plane wave basis functions inside the atomic spheres representing tungsten atoms was constructed according to the APW+lo scheme for the angular quantum numbers $l \leq 3$ and according to the LAPW scheme for higher l. The augmentation part inside the atomic spheres representing the adsorbed atoms of the $3d$ transition metals was set according to the APW+lo scheme for $l \leq 2$ and according to the LAPW scheme otherwise. The $3p$ electronic states of the $3d$ metals and the $5p$ and $4f$ electronic states of the tungsten atoms were treated as semi-core states, which meant that they were represented by a combination of the same basis functions as the valence states and that the set of the basis functions was enhanced by corresponding local orbitals so as to be able to represent these semi-core states properly. The radii of the atomic spheres were all set to 0.127 nm (2.4 a.u.), irrespective of the chemical nature of the particular atom. The radius of 0.127 nm is 93 % of the radius at which the atomic spheres of neighboring tungsten atoms arranged on the bcc lattice would touch each other.

The *ab-initio* calculations within the method implemented in WIEN2k do not account for a dipole-dipole interaction amongst the magnetic moments of individual atoms, so this interaction has to be included by a separate consideration. The part of the MAE that is contributed by the dipole-dipole interaction can be found with the help of Eq. (123). So as to find the numerical value of the anisotropy energy, one has to evaluate the sum on the right-hand side of that equation. The summation may be performed numerically provided that the sum is restricted to a very large but finite number of terms around the origin (i.e. around n_x=0, n_y=0). However, the sum converges very slowly with an increasing number of terms included in it. It is therfore preferable not to omit the terms corresponding to the infinite number of distant dipoles completely. Instead, the discrete terms beyond certain distance from the origin should be replaced with an integral, as if there was continuously distributed magnetization replacing the point dipoles:

$$\sum_{n_x,n_y} \frac{n_x^2}{\left(n_x^2+n_y^2\right)^{5/2}} \longrightarrow \int \frac{x^2}{\left(x^2+y^2\right)^{5/2}} dx\, dy$$

for large enough n_x ($n_x = x$; $|x| > a$) or large enough n_y ($n_y = y$; $|y| > b$). The division of the surface plane to the respective areas of summation and integration is sketched in Fig. 24. The integral over an area outside a rectangle that has a side of length a parallel with the x axis and a side of length b parallel with the y axis can be evaluated analytically; the result is

$$\int_A \frac{x^2}{\left(x^2+y^2\right)^{5/2}} dx\, dy = \frac{4\left(2b^2+a^2\right)}{3ab\sqrt{a^2+b^2}}; \quad A \equiv \{[x,y];\ (|x| > a) \vee (|y| > b)\} \qquad (136)$$

The terms from within the rectangle have to be summed one by one numerically and added to the value of the integral to obtain an approximation for the infinite

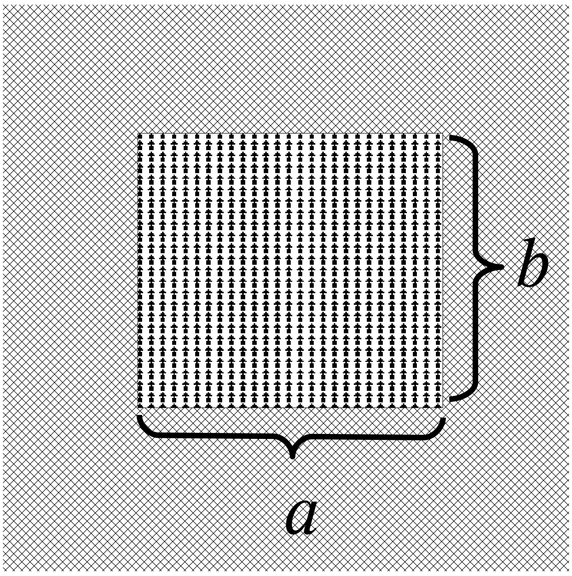

Figure 24: *The division of the infinite area over which the contributions from the magnetic dipoles have to be added together. A numeric summation of discrete terms is performed inside the rectangle with sides of lengths a and b. In contrast, an integration of a smooth function corresponding to a constant magnetization density is performed over the cross-hatched area outside the rectangle. The contributions from the two regions are then added to obtain the final result. The precision of the resulting approximation improves quite fast as $a \to \infty$, $b \to \infty$.*

sum. I have calculated the estimate of the infinite sum for several different values of a (with $b = a$) to check the convergence of the result. Finally, I have obtained

$$\frac{3}{2} \sum_{n_x, n_y} \frac{n_x^2}{\left(n_x^2 + n_y^2\right)^{5/2}} = 6.7752\ldots \tag{137}$$

for $a = b > 25$.

Substituting the numerical values from Eq. (122) and Eq. (137) together with $a_{\|} = a_{\mathrm{W}} = 0.3165$ nm into Eq. (123), one finally obtains

$$(E_{\|} - E_{\perp}) = -0.0115\,\mathrm{meV} \times (\mu/\mu_B)^2 \tag{138}$$

per adatom for that part of the magnetic anisotropy in the overlayer on W(001) that is contributed by the dipole-dipole interaction. The above formula takes into account only spin moments associated with atoms of the $3d$ transition element on top of the W(001) surface. The orbital-moment contribution to the total magnetic moments of atoms is neglected and so are the induced magnetic moments at the tungsten atoms.

The magnetic moments of the atoms in the three different ferromagnetic overlayers, vanadium, chromium, and manganese on W(001), are listed in Tab. 8 along with the MAE resulting from the magnetic dipole-dipole interaction and the MAE resulting from the spin-orbit coupling. The magnetic moments in the table were obtained

adatom	μ/μ_B	$(E_\parallel - E_\perp)_{dd}$	$(E_\parallel - E_\perp)_{SO}$
V	1.40	-0.022 meV	$-\mathbf{2.0}$ meV
Cr	2.48	-0.071 meV	$+\mathbf{2.7}$ meV
Mn	3.31	-0.126 meV	$+\mathbf{5.2}$ meV

Table 8: *Spin-related magnetic moments of adatoms, the contribution of the dipole-dipole interaction to the magnetic anisotropy energy per surface atom, and the contribution of the spin-orbit interaction to the magnetic anisotropy energy per surface atom for the ferromagnetic monolayers on W(001).*

atom	K_2 [meV]	$K_{4\perp}$ [meV]	$K_{4\parallel}$ [meV]
Mn	$+0.07$	$+0.00$	$+0.00$
W(I)	$+3.65$	$+0.00$	-0.05
W(I-1)	$+1.69$	-0.12	$+0.01$

Table 9: *Atom-specific contributions to the constants that describe the magnetocrystalline anisotropy of the Mn/W(001) system in accord with Eq. (139). Shown are the contribution from the overlayer Mn atoms, tungsten atoms in the top (interface) substrate layer W(I) and tungsten atoms in the next (the nearest sub-interface) substrate layer W(I-1) [76].*

as a difference between the spin-up and spin-down electron density integrated over the atomic sphere of one atom in the overlayer. Although the magnetic moments were calculated self-consistently with the spin-orbit interaction switched on, their numerical values do not significantly depend on the orientation of the spin quantization axis, so our model for the dipole-dipole coupling can be used. Evidently, the anisotropy energy originating from the dipole-dipole interaction is negligible by comparison with the anisotropy energy resulting from the spin-orbit interaction. The part of the MAE that originates from the dipole-dipole interaction thus needed to be estimated for the sole purpose of demonstrating that this part of the anisotropy energy is small enough to be neglected. The magnetic anisotropy energy originating from the spin-orbit interaction is approximately equal to the total MAE and the values in the last column of Tab. 8 are therefore printed in bold. From the values of the MAE shown in the last column of Tab. 8, we see that the magnetic moments of the vanadium atoms on W(001) tend to be aligned along the surface plane while the magnetic moments of chromium and manganese atoms tend to orient themselves perpendicular to the surface plane.

The notably large magnetocrystalline anisotropy of the Mn/W(001) overlayer, which has been obtained as one of the results of this thesis, has stimulated further investigation of this system [76]. So as to better understand the origin of the magnetocrystalline anisotropy, contributions of the spin-orbit coupling at individual atoms to the MAE were calculated. The use of the torque method [77, 78] have allowed us to make such a decomposition of the total MAE into the atom-specific components. The magnetocrystalline anisotropy can be, in general, characterized as a dependence of the total energy of the system on the direction of its magneti-

atom	$M_S^{\parallel}/\mu_B$	$M_S^{\perp}/\mu_B$	$M_L^{\parallel}/\mu_B$	$M_L^{\perp}/\mu_B$
Mn	3.174	3.176	0.073	0.087
W(I)	−0.342	−0.343	−0.011	−0.055
W(I-1)	0.073	0.072	−0.009	−0.013

Table 10: *Spin (M_S) and orbital (M_L) magnetic moments of Mn atoms in the overlayer, tungsten atoms in the top (interface) substrate layer W(I), and tungsten atoms in the next (the nearest sub-interface) substrate layer W(I-1). Values of the magnetic moments for both the parallel ($\|$) and perpendicular ($\perp$) orientation of these moments with respect to the surface plane are listed [76].*

zation. The direction-dependent part of the total energy per surface atom is, up to the fourth order, given by

$$\Delta E(\theta, \phi) = K_2 \sin^2(\theta) + K_{4\perp} \sin^4(\theta) + K_{4\|} \sin^4(\theta) \cos(4\phi), \tag{139}$$

where the polar angle θ is an angle between the magnetization (or, equivalently, the magnetic moments) and the normal to the surface plane. Tab. 9 presents the decomposition of the anisotropy constants that appear in Eq. (139) into contributions associated with individual atoms. As could be expected, the magnetocrystalline anisotropy is dominated by the uniaxial part that is represented by K_2, while the higher order terms of the anisotropy play only a minor role. Obviously, the largest contribution to the uniaxial anisotropy comes from the interface layer of the W substrate while the contribution from the Mn overlayer is rather small.

Spin and orbital magnetic moments of individual atoms in the Mn/W(001) surface system are shown in Tab. 10. Once again, we see that the spin magnetic moments do not depend very much on the direction of the magnetization axis, in contrast to the orbital moments, which are, however, substantially smaller. While the Mn atoms carry most of the magnetization associated with the Mn/W(001) system, there are also considerable induced magnetic moments at atoms of the tungsten interface layer. It is argued in [76] that the main contribution to the MAE of the $3d$ transition metals (like Mn) on the substrate of a $5d$ transition metal (like W) can be expressed as

$$E_{MA}^{5d} = -k_2^{5d} \chi^2 \sum_{ij} J_{3d-5d}^{i} J_{3d-5d}^{j} M_i^{3d} M_j^{3d}, \tag{140}$$

where k_2^{5d} is the normalized uniaxial anisotropy constant of the substrate atoms, χ is the local spin susceptibility of the substrate atoms, M_i^{3d} are the magnetic moments of the spontaneously magnetized overlayer atoms, and $\sum_i J_{3d-5d}^{i} M_i^{3d}$ expresses the exchange splitting that is induced in the interface atomic layer of the substrate by the magnetic overlayer. Therefore the large magnetocrystalline anisotropy energy of the Mn/W(001) surface is caused by the combined effects of a strong spin-orbit coupling at W atoms, large magnetic moments of the Mn overlayer atoms and a strong exchange coupling between the Mn atoms and the W atoms in the interface layer.

The Curie temperature T_C of the ferromagnetic Mn/W(001) system was estimated in [76] using the random phase approximation [79], which leads to the relation [80]

$$\frac{1}{k_B T_C} = \frac{6}{M}\frac{1}{N}\sum_{\vec{q}}^{\mathrm{BZ}} \frac{1}{E(\vec{q})}, \tag{141}$$

where the sum over the reciprocal vectors $\vec{q}$ samples the two-dimensional Brillouin zone and where

$$E(\vec{q}) = \frac{4}{M}\sum_{j\neq 0} J_{0j}[1 - \exp(i\vec{q}\cdot\vec{R}_{0j})] + \Delta. \tag{142}$$

In the above formulae, M is the magnetic moment per surface atom in Bohr magnetons, $\vec{R}_{0j}$ are positions of surface atoms with respect to one specific surface (Mn) atom that has been chosen as the origin, J_{ij} are the exchange parameters (exchange coupling constants) between surface atoms, and Δ is the total uniaxial MAE per surface atom (including the contribution from the dipole-dipole interaction). The sum over j on the right-hand side of Eq. (142) was limited to the nearest and second nearest neighbors and the values of $J_{01} = 22.78$ meV and $J_{02} = -7.11$ meV were substituted for the exchange parameters in Eq. (142). The exponenetial functions in Eq. (142) were expanded into polynomials up to the second order in $|\vec{q}|$. Based on the above data and approximations, the Curie temperature of the Mn/W(001) overlayer was estimated to be 655 K, a value well above the room temperature.

4.5 Summary of results for the $3d$ metals on W(001)

The theoretical study that deals with the two-dimensional binary alloys of magnetic $3d$ transition metals placed as monoatomic layers on the tungsten (001) surface has revealed the main tendencies that drive the orientation of local magnetic moments in these alloys. Apart from the already known magnetic interaction between atoms belonging to the same chemical element, namely the ferromagnetic interaction in vanadium, chromium, and manganese overlayers and the antiferromagnetic interaction in iron and cobalt overlayers, the following tendencies have been found to prevail in the magnetic interaction between atoms of different elements: the tendency to ferromagnetic ordering for any combination of vanadium, chromium, and manganese (VCr, VMn, CrMn) and also a weak tendency to ferromagnetic ordering between V and Fe, and the tendency to antiferromagnetic ordering not only between Fe and Co atoms, but also for FeCr, FeMn, CoCr, CoMn, and for CoV too. These sometimes contrary tendencies exhibited by the magnetic moments in the overlayers presumably lead to complex magnetic structures, which pose new challenges for the spin-polarized scanning tunneling microscopy. Moreover, while the magnetic moments of vanadium atoms tend to align in the plane of the surface, the magnetic moments of Cr, Mn, and Fe tend to be oriented perpendicular to the surface. Such differences in the character of the surface magnetocrystalline anisotropy further enhance the complexity of the magnetic properties expected for the vanadium-containing alloys on W(001), probably resulting into non-collinear magnetic structures (which has been also observed for a pure manganese overlayer on the same tungten surface anyway [58]). The magnetic moments of atoms from Cr to Co are rather robust in their magnitudes; these magnetic moments do not change much with changing chemical composition of the environment surrounding the atom.

The magnetic interactions in the surface alloys consisting of these elements can be effectively described by a classical Heisenberg model. The more itinerant magnetism of vanadium leads to a more complex behavior of its atomic moments. The magnetic moments of vanadium atoms are much more sensitive to their atomic neighborhood than the magnetic moments of the other elements (Cr, Mn, Fe, and Co) and the surface alloys that contain vanadium therefore defies the simplified description along the lines of the Ising or Heisenberg models.

The investigation of submonoatomic films of the $3d$ metals on the W(001) surface has shown a trend towards decreasing magnetic moments of individual atoms (especially of V, Cr, and Mn, but to a smaller extent also of Fe and Co) with decreasing thickness of the films, hence with decreasing average number of nearest atomic neighbors. For vanadium and chromium and (perhaps) also for manganese, the magnetic moment completely disappears if the coverage of the W(001) surface by these elements is low enough. Advances in the field of the scanning tunneling microscopy make it possible to probe magnetic properties of even single atoms on solid surfaces; this was first achieved indirectly using spin-averaged STS—see for example [81] or [82]—and lately also with the spin-polarized STM/STS [83]. Future experiments using the SP-STM will thus hopefully confirm the lack of spontaneous magnetization in incomplete vanadium or chromium layers sparsely covering the W(001) surface.

5 Summary

Two types of solid surface systems—first, the (001) surface of the fcc Invar alloy ($Fe_{0.64}Ni_{0.36}$) and, second, the bcc tungsten (001) surfaces covered with complete or incomplete monoatomic layers of various $3d$ transition metals (V, Cr, Mn, Fe, or Co) or with binary two-dimensional alloys of these metals—have been analyzed theoretically in terms of their geometrical, electronic, and magnetic structure, mainly with the aim of assisting the interpretation of experimental data like atomically resolved STM images and STS spectra.

1. It was found that the top atomic layer of the $Fe_{0.64}Ni_{0.36}$ alloy (001) surface is buckled with Fe pushed outwards and Ni inwards. The buckling height in the top layer, reaching up to 0.135 Å, depends on the type of atoms in sub-surface layers. The STM image of the (001) Invar surface reflects essentially the surface topography. The brighter spots (larger tunneling current) can be associated with Fe atoms, the darker spots with Ni atoms. The observed brighter and darker areas superimposed on the atomic contrast are related to regions of different local chemical composition in the sub-surface.

   The correctness of the chemical identity ascribed to the atoms in the images has been also corroborated by the finding that the $c(2 \times 2)-$FeNi checkerboard pattern of alternating Fe and Ni atoms, which has been identified as the prevailing structure in the experimental images, is indeed an especially stable structure in terms of its total energy.

   A surface resonance at about -0.3 eV bellow Fermi level on iron-rich alloy surfaces has been identified as the cause of the peak of the differential tunneling conductance that can be observed in the STS. The sensitivity of this peak to the chemical composition of the surface offers a possibility to distinguish between iron-enriched and iron-depleted surface areas.

2. The study of the magnetic ordering exhibited by the $3d$ bi-metallic alloy monolayers on the W(001) substrate has shown that the two constituent elements tend to orient their local magnetic moments antiparallel to each other in the FeMn, FeCr, CoMn, CoCr, and CoV alloys, while Fe and V have a weak tendency to align their moments parallel to each other. Due to incompatible tendencies of magnetic moment alignment, an uncompensated DLM phase becomes the state with minimal total energy for some of the surface alloys, indicating a complex behavior with possible non-collinear magnetic ground state of these alloys.

   Magnetic moments of Cr, Mn, and Fe atoms keep almost constant magnitudes, irrespective of the chemical composition of their neighborhood, while the magnetic moments of vanadium atoms are considerably sensitive to the local environment. Magnetic moments of Co atoms are either reduced or even completely suppressed by a large inward relaxation of the these atoms on the W(001) surface.

The interaction between magnetic moments of atoms of the $3d$ elements on the W(001) substrate has been characterized in terms of a prevailing ferromagnetic or antiferromagnetic tendency. The tendency to ferromagnetic (V, Cr, Mn) vs. antiferromagnetic (Fe, Co) order in these layers differs significantly from the situation on many other substrates, e.g. on W(110) [54, 55, 56, 57], Ag(001) [53], or Pd(001) [52]. The magnetic moments associated with the atoms of the $3d$ transition elements, especially V and Cr, also largely depend on the degree of coverage of the tungsten surface by these elements when they form an incomplete overlayer on the W(001) substrate.

3. The surface magnetocrystalline anisotropy that governs the orientation of the magnetic moments associated with the overlayer atoms on the W(001) substrate has been evaluated for the $3d$ metallic overlayers. In-plane (along-the-surface) alignment of the surface magnetic moments is favored by the surface anisotropy for V/W(001) and out-of-plane (normal-to-the-surface) alignment is favored for Cr/W(001) and Mn/W(001). A particularly large magnetocrystalline anisotropy energy (MAE)—over 5 eV per manganese atom—has been found for the Mn/W(001) monolayer.

My study of the Invar surface has explained the sources of contrast in STM images of this surface and the relation of the STS to the local surface composition, thus laying the basis for further research of the technologically important Fe-Ni alloys using the STM technique. Tungsten surfaces are often used as model substrates to study magnetic nanostructures grown on non-magnetic substrates (see e.g. [54, 55, 56, 57, 58]). The large MAE of the Mn films on this W(001) substrate shows that it is worthwhile to further explore the magnetic surface structures that combine the $3d$ and $5d$ transition metals: structures with such a large MAE may find practical applications, e.g., in information storage devices [76].

References

[1] G. Binnig, H. Rohrer, Ch. Gerber, and E. Weibel, Phys. Rev. Lett. **49**, 57–61 (1982).

[2] G. Binnig, H. Rohrer, Ch. Gerber, and E. Weibel, Surf. Sci. **131** L379–L384 (1983).

[3] G. Binnig, H. Rohrer, Ch. Gerber, and E. Weibel, Phys. Rev. Lett. **50** 120–123 (1983).

[4] M. Bode, Rep. Prog. Phys. **66**, 523–579 (2003).

[5] U. Kaiser, A. Schwarz, and R. Wiesendanger, Nature **446** 522–525 (2007).

[6] G. Binnig, H. Rohrer, Ch. Gerber, and E. Weibel, Appl. Phys. Lett. **40**, 78–80 (1982).

[7] G. Binnig and H. Rohrer, Rev. Mod. Phys. **59**, 615–625 (1987).

[8] W.A. Hofer, A.S. Foster, and A.L. Shluger, Rev. Mod. Phys. **75**, 1287-1331 (2003).

[9] J. Bardeen, Phys. Rev. Lett. **6**, 57–59 (1961).

[10] C.J. Chen, J. Vac. Sci. Technol. A **6**, 319–322 (1988).

[11] C.J. Chen, Mod. Phys. Lett. B **5**, 107–115 (1991).

[12] J. Tersoff and D.R. Hamann, Phys. Rev. Lett. **50**, 1998–2001 (1983).

[13] C.J. Chen, Phys. Rev. Lett. **65**, 448–451 (1990).

[14] C.J. Chen, Phys. Rev. B **42**, 8841–8857 (1990).

[15] P. Hohenberg and W. Kohn, Phys. Rev. **136**, B864–B871 (1964).

[16] R.M. Dreizler and E.K.U. Gross: *Density Functional Theory (An Approach to the Quantum Many-Body Problem)*, Springer-Verlag, Berlin/Heidelberg/New York, 1990, ISBN 3-540-51993-9.

[17] M. Levy, Proc. Natl. Acad. Sci. USA **76**, 6062–6065 (1979).

[18] W. Kohn and J. Sham, Phys. Rev. **140**, A1133–A1138 (1965).

[19] D.M. Ceperley and B.J. Adler, Phys. Rev. Lett. **45**, 566–569 (1980).

[20] O.K. Andersen, Phys. Rev. B **12**, 3060–3083 (1975).

[21] E. Sjöstedt, L. Nordström, and D.J. Singh, Solid State Communications **114**, 15–20 (2000).

[22] S. Cottenier, *Density Functional Theory and the Family of (L)APW-methods: a step-by-step introduction* (Instituut voor Kern- en Stralingsfysica, K.U. Leuven, Belgium), 2002, ISBN 90-807215-1-4 (to be found at `http://www.wien2k.at/reg_user/textbooks`).

[23] D.J. Singh, *Planewaves, pseudopotentials and the LAPW method*, Kluwer Academic Publishers, Boston/Dordrecht/London, 1994, ISBN 0-7923-9421-7.

[24] I. Turek, V. Drchal, J. Kudrnovský, M. Šob, P. Weinberger, *Electronic Structure of Disordered Alloys, Surfaces and Interfaces*, Kluwer Academic Publishers, Boston/London/Dordrecht, 1997, ISBN 0792397983, 9780792397984.

[25] P. Soven, Phys. Rev. **156**, 809–813 (1967).

[26] P. Novák, *Notes about spin-orbit* at `http://www.wien2k.at/reg_user/textbooks`

[27] R.J. Weiss, Proc. Phys. Soc. London **82**, 281–288 (1963).

[28] K. Lagarec, D.G. Rancourt, S.K. Bose, B. Sanyal, and R.A. Dunlap, J. Magn. Magn. Mater. **236**, 107–130 (2001).

[29] V. Crisan, P. Entel, H. Ebert, H. Akai, D.D. Johnson, and J.B. Staunton, Phys. Rev. B **66**, 014416 (2002).

[30] V.M. Hallmark, S. Chiang, J.F. Rabolt, J.D. Swalen, and R.J. Wilson, Phys. Rev. Lett. **59**, 2879–2882 (1987).

[31] M. Schmid, H. Stadler, and P. Varga, Phys. Rev. Lett. **70**, 1441–1444 (1993).

[32] P.T. Wouda, B.E. Nieuwenhuys, M. Schmid, and P. Varga, Surf. Sci. **359**, 17–22 (1996).

[33] Y. Gauthier, P. Dolle, R. Baudoing-Savois, W. Hebenstreit, E. Platzgummer, M. Schmid, and P. Varga, Surf. Sci. **396**, 137–155 (1998).

[34] M. Ondráček, F. Máca, J. Kudrnovský, J. Redinger, A. Biedermann, C. Fritscher, M. Schmid, and P. Varga, Phys. Rev. B **74**, 235437 (2006).

[35] E.A. Owen, E.L. Yates, and A.H. Sully, Proc. Phys. Soc. **49**, 315–322 (1937).

[36] A.P. Miodownik, J. Magn. Magn. Mater. **10**, 126–135 (1979).

[37] P. Blaha, K. Schwarz, G.K.H. Madsen, D. Kvasnicka, and J. Luitz, **WIEN2k***, An Augmented Plane Wave + Local Orbitals Program for Calculating Crystal Properties* (Karlheinz Schwarz, Techn. Universität Wien, Austria), 2001, ISBN 3-9501031-1-2.

[38] J. P. Perdew, K. Burke, and M. Ernzerhof, Phys. Rev. Lett. **77**, 3865–3868 (1996).

[39] M. Ondráček, F. Máca, J. Kudrnovský, and J. Redinger, Czech. J. Phys. **56**, 69–74 (2006).

[40] J.A. Stroscio, D.T. Pierce, A. Davies, R.J. Celotta, and M. Weinert, Phys. Rev. Lett. **75**, 2960–2963 (1995).

[41] S. H. Vosko, L. Wilk, and M. Nusair, Can. J. Phys. **58**, 1200–1211 (1980).

[42] S.L. Altmann and A.P. Cracknell, Rev. Mod. Phys. **37**, 19–32 (1965).

[43] N. Papanikolau, B. Nonas, S. Heinze, R. Zeller, and P. H. Dederichs, Phys. Rev. B **62**, 11118–11125 (2000).

[44] A. Kubetzka, P. Ferriani, M. Bode, S. Heinze, G. Bihlmayer, K. von Bergmann, O. Pietzsch, S. Blügel, and R. Wiesendanger, Phys. Rev. Lett. **94**, 087204 (2005).

[45] R. Wu and A.J. Freeman, Phys. Rev. B **45**, 7532–7535 (1992).

[46] P. Ferriani, S. Heinze, G. Bihlmayer, and S. Blügel, Phys. Rev. B **72**, 024452 (2005).

[47] E. Fawcett, Rev. Mod. Phys. **60**, 209–283 (1988).

[48] T. Yamada, N. Kunitomi, Y. Nakai, D.E. Cox, and G. Shirane, J. Phys. Soc. Jpn. **28**, 615–627 (1970).

[49] A.C. Lawson, A.C. Larson, M.C. Aronson, S. Johnson, Z. Fisk, P.C. Canfield, J.D. Thompson, and R.B. von Dreele, J. Appl. Phys. **76**, 7049–7051 (1994).

[50] C. Rau, C. Liu, A. Schmalzbauer, and G. Xing, Phys. Rev. Lett. **57**, 2311–2313 (1986).

[51] I.G. Batyrev, J.-H. Cho, and L. Kleinman, Phys. Rev. B **63**, 172420 (2001).

[52] S. Blügel, M. Weinert, and P.H. Dederichs, Phys. Rev. Lett. **60**, 1077–1080 (1988).

[53] S. Blügel and P.H. Dederichs, Europhys. Lett. **9**, 597–602 (1989).

[54] M. Przybylski and U. Gradmann, Phys. Rev. Lett. **59**, 1152–1155 (1987).

[55] S. Heinze, M. Bode, A. Kubetzka, O. Pietzsch, X. Nie, S. Blügel, and R. Wiesendanger, Science **288**, 1805–1808 (2000).

[56] B. Santos, J.M. Puerta, J.I. Cerda, R. Stumpf, K. von Bergmann, R. Wiesendanger, M. Bode, K.F. McCarty, and J. de la Figuera, New. J. Phys. **10**, 013005 (2008).

[57] M. Bode, M. Heide, K. von Bergmann, P. Ferriani, S. Heinze, G. Bihlmayer, A. Kubetzka, O. Pietzsch, S. Blügel, and R. Wiesendanger, Nature **447**, 190–193 (2007).

[58] P. Ferriani, K. von Bergmann, E.Y. Vedmedenko, S. Heinze, M. Bode, M. Heide, G. Bihlmayer, S. Blügel, and R. Wiesendanger, Phys. Rev. Lett. **101**, 027201 (2008).

[59] M. Ondráček, J. Kudrnovský, and F. Máca, in *WDS'06 Proceedings of Contributed Papers, Part III – Physics*, eds. J. Šafránková and J. Pavlů, pp. 132–137, Matfyzpress, Prague, 2006, ISBN 80-86732-86-X.

[60] M. Ondráček, J. Kudrnovský, and F. Máca, Surf. Sci. **601**, 4261–4264 (2007).

[61] M. Ondráček, J. Kudrnovský, I. Turek, and F. Máca, J. Phys.: Conf. Series **61**, 894–898 (2007).

[62] D. Spišák and J. Hafner, Phys. Rev. B **70**, 195426 (2004).

[63] Y. Waseda, K. Hirata, and M. Ohtani, High Temp. High Pressures **7**, 221–226 (1975).

[64] A.J. Pindor, J. Staunton, G.M. Stocks, and H. Winter, J. Phys. F: Met. Phys. **13**, 979–989 (1983).

[65] I. Turek, J. Kudrnovský, V. Drchal, and P. Weinberger, Phys. Rev. B **49**, 3352–3362 (1994).

[66] D.I. Bardos, J. Appl. Phys. **40**, 1371–1372 (1969).

[67] I. Turek, J. Kudrnovský, and S. Blügel, Acta Phys. Slovaca **48**, 723–726 (1998).

[68] T.E. Felter, R.A. Barker, and P.J. Estrup, Phys. Rev. Lett. **38**, 1139–1141 (1977).

[69] A.J. Freeman and R. Wu, J. Magn. Magn. Mater. **100**, 497–514 (1991).

[70] M.K. Debe and D.A. King, Phys. Rev. Lett. **39**, 708–711 (1977).

[71] E.C. Stoner, Proc. R. Soc. Lond. A **154**, 656–678 (1936).

[72] J.F. Janak, Phys. Rev. B **16**,255–262 (1977).

[73] P.E. Blöchl, Phys. Rev. B **50**, 17953–17979 (1994).

[74] P.E. Blöchl, C.J. Först, and J. Schimpl, Bull. Mater. Sci. **26**, 33–41 (2003).

[75] N.D. Mermin and H. Wagner, Phys. Rev. Lett. **17**, 1133–1136 (1966).

[76] A.B. Shick, F. Máca, M. Ondráček, O.N. Mryasov, and T. Jungwirth, Phys. Rev. B **78**, 054413 (2008).

[77] J.B. Staunton, Ψ_k-network Highlight 82 (August 2007).

[78] X. Wang, R. Wu, D.-S. Wang, and A.J. Freeman, Phys. Rev. B **54**, 61–64 (1996).

[79] S.V. Tyablikov, *Methods of Quantum Theory of Magnetism*, Plenum Press, New York, 1967.

[80] M. Pajda, J. Kudrnovský, I. Turek, V. Drchal, and P. Bruno, Phys. Rev. Lett. **85**, 5424–5427 (2000).

[81] V. Madhavan, W. Chen, T. Jamneala, and M.F. Crommie, Science **280**, 567–569 (1998).

[82] C.F. Hirjibehedin, C.-Y. Lin, A.F. Otte, M. Ternes, C.P. Lutz, B.A. Jones, and A.J. Heinrich, Science **317**, 1199–1203 (2007).

[83] F. Meier, L. Zhou, J. Wiebe, and R. Wiesendanger, Science **320**, 82–86 (2008).